PLASMA CHARACTERISATION OF AN ELECTRON CYCLOTRON RESONANCE ION SOURCE BY MEANS OF X-RAY SPECTROSCOPY

MUNEER SAKILDIEN

A thesis submitted in partial fulfillment of the requirements for the degree of Magister Scientiae in the Department of Physics, University of the Western Cape

Supervisor: Dr. R. Thomae
Co-Supervisor: Prof. R. Lindsay

April 2012

PLASMA CHARACTERISATION OF AN ELECTRON CYCLOTRON RESONANCE ION SOURCE BY MEANS OF X-RAY SPECTROSCOPY

Muneer Sakildien

KEYWORDS

Plasma

Electron cyclotron resonance

Ion source

Bremsstrahlung

High-purity germanium detector

PIXIE4

ROOT

Spectral temperature

Electron density

Multiply-charged ions

ABSTRACT

PLASMA CHARACTERISATION OF AN ELECTRON CYCLOTRON RESONANCE ION SOURCE BY MEANS OF X-RAY SPECTROSCOPY

M. Sakildien

M.Sc. thesis, Department of Physics, University of the Western Cape.

The ultimate aim of any multiply-charged ion source, like the Electron Cyclotron Resonance Ion Source, ECRIS, is the production of multiply-charged ions, in sufficiently large quantities. These multiply-charged ions, in the case of the ECRIS, are created by a step-by-step ionisation process, whereby neutral atoms are ionised by energetic electrons. The goal of this thesis was to gain an understanding of the relative importance of various ECRIS parameters on the production of these energetic electrons. This was done by measuring the bremsstrahlung continuum emitted by the mirror confined plasma of an ECR ion source.

The focus of our study was to investigate the influence of neutral pressure, incident microwave power and magnetic field configuration on spectral temperature and electron density of the warm electron population of the ECRIS plasma. The thesis begins by familiarising the reader with various aspects of plasma physics as it relates to the measurements.

The measurements were done with a high-purity germanium detector and processed with the DGF Pixie-4 module. Analyses of the measured spectra were done with subroutines written in Root. From the measured result, it was concluded that by increasing the incident microwave power from 50 W to 300 W, the spectral temperature increases by 14.01% for helium plasma and 7.88% for argon plasma. Evidence of saturation of spectral temperature and electron density with increasing microwave power was also noticed, as reported by other groups investigating plasma bremsstrahlung. The increase of spectral temperature with neutral pressure was found to be considerable, increasing by 20.23% as the neutral pressure in the plasma chamber of the ECRIS was decreased. This increase in spectral temperature was accompanied by a 40.33% decrease in electron density, which led us to conclude that the increase in spectral temperature was most likely due to an increase in the mean free path of the electrons.

The influence of the magnetic field configuration on both spectral temperature and electron density was also investigated. During this investigation, one of the solenoid coil currents was increased, whilst keeping the other constant. This amounts to moving the plasma volume around axially in the plasma chamber of the ECRIS. This was found to significantly enhance the spectral temperature and this effect was attributed to more efficient heating of the electrons near the resonance zone. The electron density on the other hand was found to remain relatively constant, if one excludes the electron density as a result of one particularly setting of the solenoid coils. The decrease of electron density as a result of this particular setting of the solenoid coils enhanced the electron losses through the magnetic bottle. This is evidenced by the increase in photon counts as measured by our detector. The influence of neutral pressure, incident microwave power and magnetic field configuration on the extracted ion beam intensities was also investigated. This investigation led us to conclude that the mean charge state extracted increases with spectral temperature. This result was in agreement with those measured by other groups.

April 2012

DECLARATION

I declare that *Plasma characterisation of an Electron Cyclotron Resonance Ion Source by means of X-ray spectroscopy* is my own work, that it has not been submitted before for any degree or examination in any university, and that all the sources I have used or quoted have been indicated and acknowledged as complete references.

Muneer Sakildien

April 2012

Signed:…….

ACKNOWLEDGEMENTS

My sincere appreciation goes to Dr. P. Papka for tirelessly assisting me with the experimental set-up and data analysis software and for his many ideas on improving the experimental set-up.

I thank my supervisor, Dr. R. Thomae, for suggesting this topic and for his continued interest in this work.

I would also like to thank my co-supervisor, Prof R. Lindsay, for allowing me the opportunity to pursue a graduate degree.

I would also like to thank Mr. S. Murray for his many hours spend in assisting me with the software to analyse the measured spectra.

A word of appreciation also needs to be expressed to Mr. R. Pylman for his assistance during the actual measurements.

I would also like to thank the radionuclide department for allowing me the use of their detector and electronics and for supplying me with liquid nitrogen throughout the course of this study.

I would also like to thank the nuclear physics department for affording me the opportunity to use the DGF Pixie-4 to acquire my data.

Finally I would like to thank my family for their support and patience throughout the course of this study.

Plasma characterisation of an electron cyclotron resonance ion source by means of X-ray spectroscopy

M.Sakildien

September 5, 2012

Contents

Chapter 1

Motivation and outline

1.1 Introduction

In 1947, the head of the Radioactivity Division of the Council for Scientific and Industrial Research, CSIR, upon returning from a sabbatical abroad, proposed the construction of a cyclotron, South Africa's first resonance accelerator [1]. The acceptance of this proposal in 1950 signalled the entrance of South Africa into the cyclotron community.

The Pretoria cyclotron, as it came to be known, was initially used for training and research in nuclear physics. During the course of its lifetime, it was also used for the production of short-lived medical radioisotopes, as well as long-lived radioisotopes for industrial purposes. This conventional solid-pole cyclotron was a fixed frequency, fixed-energy machine [2]. It could therefore only accelerate particles with a charge-to-mass ratio of $\frac{1}{2}$ to relatively low energies [2]. Alpha particles, deuterons and protons, as H_2^+-ions, could be accelerated to 32 MeV, 16 MeV and 8 MeV, respectively [2].

During the nineteen sixties, the cyclotron was modified to accelerate particles with different charge-to-mass ratios to variable energies, protons from 5.8 MeV to 15.3 MeV, deuterons from 11.5 MeV to 17.3 MeV, ^{3}He-ions from 18 MeV to 37 MeV and α-particles from 23 MeV to 34.6 MeV [2]. Around this time, it became apparent to the scientific community, that if they were to continue pursuing internationally competitive research, they would have to invest in a new more powerful accelerator, which could also be used for the production of radioisotopes. At the same time, radiotherapists were interested in an accelerator for proton and neutron therapy. In 1973, a feasibility study was commissioned, which concluded in 1975 with a proposal to con-

struct a new 200 MeV Separated Sector Cyclotron, SSC. This proposal was subsequently approved and the task of administrating the construction of such a multidisciplinary research centre was allocated to the CSIR in 1977 [1].

The beam specification stipulated for the purpose of the feasibility study was diverse. The main beam requirements for the different user groups were specified as follows [3]:

- for nuclear physics, general physics and nuclear chemistry the requirements were, proton beams in the energy range 20 MeV to 200 MeV with beam intensities less then 10 μA, deuterium to helium energies typically 50 MeV per nucleon with intensities in the range 1 pμA to 10 pnA, helium to argon energies typically between 15 MeV to 50 MeV per nucleon with intensities similar to those for deuterium and helium.
- for neutron therapy, deuterons and protons in the energy range 16 MeV to 100 MeV, with typical beam intensities ranging between 10 μA to 100 μA.
- for proton therapy, proton radiography and radiobiology, protons with an energy less than or equal to 200 MeV, with typical beam intensities of 1 μA.
- for radioisotope production, deuterons and protons, with beam energy less than 80 MeV and intensities greater than 100 μA.

The recommendation from the task group charged with the feasibility study was that a SSC would be the best choice as a main accelerator. To cater for the diverse user requirements, it was recommended to use two pre-accelerators: one for light ions and a second for heavy ions.

High extraction efficiencies, strong vertical focusing, the possibility to install flat-topping resonators and high quality beams were seen as primary reasons for choosing an SSC [3]. A solid-pole cyclotron as pre-accelerator was chosen primarily because of its ability to produce high-intensity beams which could be extracted with little effort [3].

Since most of the user requirements could be fulfilled with beams pre-accelerated in the light ion injector, a decision was made to start its construction first. This injector was a solid-pole cyclotron, SPC1, with a maximum

bending magnet power for 8 MeV protons, i.e. a cyclotron with a K-value of 8, equipped with an internal Penning Ionisation Gauge, PIG, source.

The initial recommendation from the task group was to construct a second solid pole cyclotron, with a K-value of 40 and an internal PIG source for acceleration of heavy ions. High charge states could then be obtained by charge stripping between this injector and the SSC. During the construction phase of the SPC1, a breakthrough in ion sources led to the scrapping of the idea of aforementioned K 40 cyclotron in favour of a K 10 solid-pole cyclotron, SPC2, with a new type of ion source, the Electron Cyclotron Resonance Ion Source, ECRIS. The SPC2 could therefore be practically identical to SPC1, except that the beam has to be injected axially, since an ECRIS is too large to be installed inside a cyclotron.

During his post gradual work at Grenoble, Richard Geller became frustrated with hot-cathode ion sources as these needed to be serviced frequently [4]. He therefore investigated a means of producing highly charged particles without cathodes. This led to the discovery of the ECRIS. The first operational ECR ion source in South Africa was of the minimafios type. The minimafios used at iThemba LABS was the second generation of these sources and was designed and build in Grenoble, France. The first beam was extracted from this source on the 13^{th} of June 1990 and on 30^{th} of June that same year, the first beam was extracted from SPC2 [5]. The first highly charged beam, 268 MeV $^{12}C^{4+}$, was extracted from the SSC on the 10^{th} September 1994 [5].

Since the installation of the minimafios source, many improvements have been made to ECR ion sources. These improvements resulted in ions with higher charge states and greater beam intensity. In order for iThemba LABS to continue to produce scientific work of international standard, it became imperative to invest in a new, more powerful ECRIS as soon as funds could be obtained. To this end, funds were made available to pursue the abovementioned goal. A new ECRIS, the Grenoble Test Source, GTS2, has now been build and installed in the ECR vault at iThemba LABS.

Additionally, iThemba LABS have also installed and operated, for a while now, a 14.5 GHz Caprice type ECRIS, also known as the ECRIS4, donated by the Helmholtz Zentrum Berlin, formerly known as the Hahn-Meitner Institute, HMI. The Minimafios ECRIS has now been decommissioned.

1.2 Motivation for the study

The initial beam requirements of the iThemba LABS facility, as set forth in the technical report of the accelerator task group were as follows, for nuclear physics, general physics and nuclear chemistry [3]:

- protons beams in the energy range 20 MeV to 200 MeV with beam intensities less than 10 μA
- deuterium to helium energies typically 50 MeV per nucleon with intensities in the range 10 pnA to 1 pμA
- helium to argon energies typically between 15 MeV to 50 MeV per nucleon with intensities similar to those for deuterium and helium

To reach these 'high-energy' requirements, the ion sources must produce higher charge states, as the particle energy delivered by a cyclotron is given by [4]:

$$W = K\left(\frac{q}{M}\right)^2 \tag{1.1}$$

where

- q is the charge of the ion
- M is the mass of the ion
- K is an efficiency factor

Given the pivotal role played by the electrons in an ECRIS in the production of highly-charged ions, it is important to gain as much information as possible about the electron populations present in such an ion source. To accomplish this task, it was set out to measure the bremsstrahlung radiation emitted by the plasma of an ECRIS. From the information gathered one can then suggest ways to optimise the ECRIS for the production of highly-charged ions.

Bremsstrahlung radiation measurements have never been performed on any of the existing ECR ion sources at iThemba LABS. These types of measurements are the only diagnostic that can be used to gain information about the high-energy electrons inside an ECRIS plasma [6]. This high-energy electron population plays an instrumental role in the formation of multiply-charged ions inside the source. If by some means, one were able to gather information

about these high-energy electrons, this would theoretically allow one to gain a handle on the production of multiply-charged ions inside the source. This was ultimately the goal of this study.

1.3 Outline of the thesis

The thesis is structured as follows:

- Chapter 2 briefly describes the iThemba LABS accelerators and the facility in general.
- Chapter 3 highlights the basic aspects of plasma physics, starting with the particle dynamics in a plasma and progressing to the fluid description of a plasma.
- Chapter 4 describes the inner workings of the ECRIS, dealing with topics like the confinement field and the interaction of the external microwaves with the plasma.
- The experimental work performed on the ECRIS4 are dealt with in chapter 5. This chapter summarises bremsstrahlung measurements performed by other group and covers the bremsstrahlung measurements performed on the ECRIS plasma, as well as discussion of the results.
- Finally, chapter 6 summarises the study and draws conclusions.

Chapter 2

Layout of the facility

2.1 Introduction

The layout of the cyclotrons and their beamlines are shown in figure 2.1. A high-intensity proton beam is pre-accelerated to an energy of 3.14 MeV in the light-ion injector cyclotron, SPC1, and transported to the SSC through a transfer beamline with provision for re-bunching of the beam, beam pulse length definition, beam emittance definition and energy selection.

The beam is horizontally injected into the SSC and accelerated to an energy of 66 MeV. From the SSC the 66 MeV beam is directed, with bending magnets and focused transversely with quadrupole magnets, to a horizontal and a vertical beam target station for the production of radioisotopes and a vault for neutron therapy treatments, at beam intensities of 100 μA, 250 μA and 30 μA, respectively. Less intense beams of protons, also pre-accelerated in SPC1, but to an energy of 8 MeV, are accelerated to 200 MeV in the SSC and directed to the vault for proton therapy treatments.

Beams of polarised hydrogen and heavy ions are pre-accelerated in the second injector cyclotron, SPC2, injected into the SSC and from there directed to the facilities for Nuclear Physics research. These facilities consist of a 1.5 m scattering chamber, a K 600 magnetic spectrometer, a γ-ray spectrometer and a beamline for the production of neutron beams. Due to the varied user community, the facility is operated according to a tight twenty four hour, seven day a week schedule, with planned maintenance periods.

SPC1 was built with an internal ion source, specifically for the production of light ions. SPC2 was built several years after SPC1 and the SSC was

put into operation and is fed axially from one of two external ion sources. Currently a third external ion source is being commissioned. The one type of external source is called an ECR ion source and produces highly-charged particles using energetic electrons. The other external source is of the atomic beam type and produces polarised protons and deuterons using inhomogeneous magnetic fields [7]. The third source is also of the ECRIS type. Beams of charged particles are then fed into SPC2 from either source using an inflector.

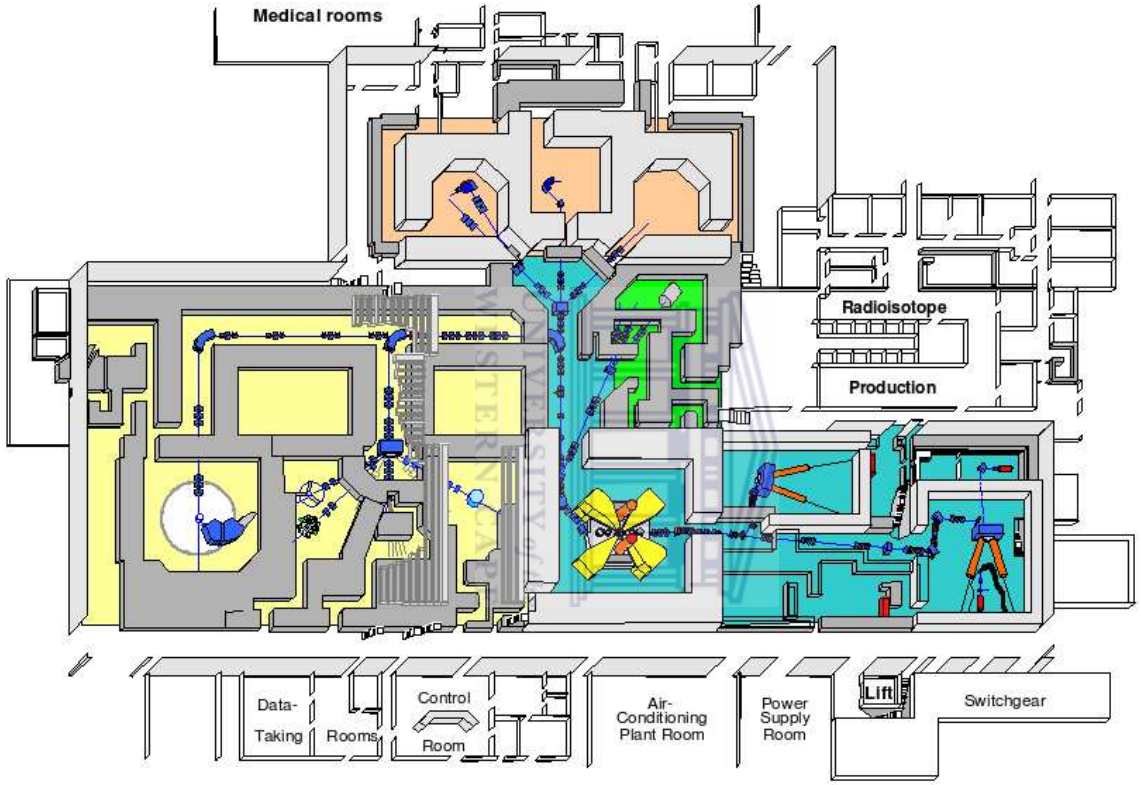

Figure 2.1: The present layout of the iThemba LABS facility showing the different vaults.

2.2 Main Parameters of the Cyclotrons and Ion Sources

2.2.1 The separated-sector cyclotron, SSC

The SSC is a variable energy machine, which was designed to produce protons of maximum beam energy 200 MeV although on one occasion the proton beam energy was increased to 227 MeV [5]. The layout of the major components in the SSC is shown in figure 2.2.

The magnet system of the SSC comprises four identical C-shape sector magnets [8]. Each of these four sector magnets has a sector angle of 34°. This compromise angle was chosen mainly to avoid serious resonances in the betatron oscillations during acceleration resulting in beam loss [3]. Each of the sector magnets has three sets of coils, giving it a maximum flux density of 1.265 T in the 66 mm pole gap [3]. The main field is provided by a single coil layer around the pole tips which provides a flux density of 1.15 T [8]. Additional coils are wound around the yoke to correct for difference in steel properties between sector magnets [9]. To preserve isochronism over the radial distance, the flux density must increase by 20% if protons are to be accelerated to 200 MeV [8]. To accomplish this, a set of 29 trim coils is used.

The four sector magnet system confines the particle trajectory to a spiral of increasing radius. The charged particle beam thus repeatedly traverses an acceleration gap, across which an accelerating voltage is applied . This accelerating voltage is provided by the RF system, which consists of two $\left(\frac{\lambda}{2}\right)$-resonators with a delta shaped accelerating electrode [10]. The resonators are each capacitively coupled to a 150 kW power amplifier. To minimise the reflected power in the RF circuit, the input impedance of the resonator needs to match the output impedance of the power amplifier. This matching is done with variable capacitors. To tune the resonator to different frequencies, the capacitance needs to be adjusted coarsely. These adjustments are made with the short-circuit plates. The resonator can be tuned over the resonance frequency range 6 to 26 MHz [10].

Pre-accelerated beams from SPC1 or SPC2 are transported via a transfer beamline and guided through the virtually field-free central region onto the first well-centred orbit [3]. The central region refers to the region in the

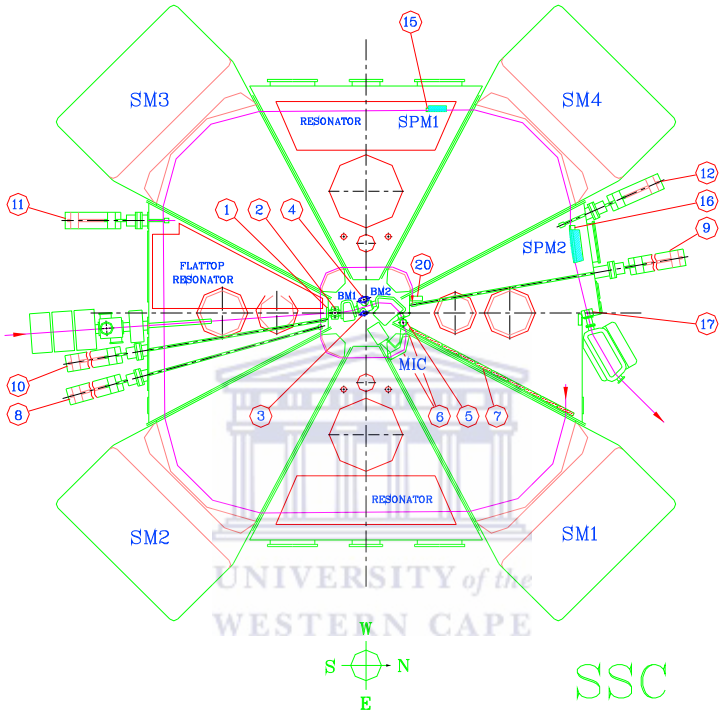

Figure 2.2: The layout of the major components in the SSC: 1, injection collimator; 2, harp; 3, beam profile scanner; 4, capacitive phase probe; 5, harp; 6, magnetic injection channel collimators and liners; 7, axial graphite collimators, 8 & 9, multi-head probes; 10, beam stop; 11, extraction harp 1; 12, extraction harp 2; 13, extraction scanner; 14, electrostatic extraction channel collimators; 15, septum magnet 1-collimators and liners; 16, septum magnet 2-collimators and liners; 17, extraction collimators; 18, electrostatic inflection channel collimators; 19, radial slit; 20, beam centering harp.

SSC where the sector magnets all come together as shown in figure 2.2. The process of injection into the SSC from the low energy side is accomplished using two bending magnets to compensate for the stray field from the sector magnets and a magnetic inflection channel, MIC. This magnetic channel is situated in the pole tip of the first sector magnet, SM1, and supplies additional bending power to bend the beam sufficiently [3]. The process of extraction is achieved using two C-shape iron cores with surrounding conductors [3]. These septum magnets, as they are called, deflect the high-energy particles from their orbits thereby increasing the orbit separation. This makes single-orbit extraction possible.

2.2.2 The light-ion solid-pole injector cyclotron, SPC1

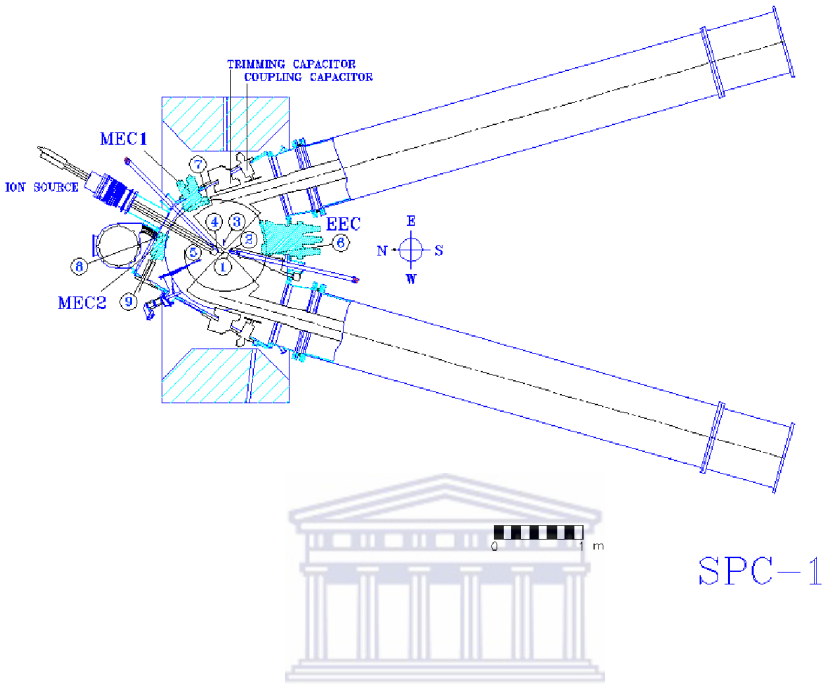

Figure 2.3: The layout of the major components in SPC1: 1, ΣΔR probe no.1; 2, RADAX slits; 3, 2nd radial slit; 4, ΣΔR probe no.2; 5, 2nd axial slit; 6, EEC collimators; 7, 1st magnetic channel collimators and liner; 8, 2nd magnetic channel collimators and liner; 9, passive magnetic channel collimators.

The layout of SPC1 is shown in figure 2.3. SPC1, like the SSC, is also a variable-energy machine and was designed to accelerate protons to a maximum beam energy of 8 MeV. It is equipped with an internal Penning Ionisation Gauge, PIG, ion source capable of accelerating particles ranging from protons to heavy ion beams with a mass-to-charge ratio, $\left(\frac{q}{m}\right)$, of 0.25 [11], where q is the charge state and m is the ion mass in atomic mass units. SPC1 is however mostly used for the production of radioisotopes and for neutron therapy using 3.14 MeV protons and for proton therapy using 8 MeV protons. The RF frequency of SPC1 ranges from 8.6 MHz to 26 MHz and the 2nd and 6th harmonic modes are used for acceleration [11]. Extraction from SPC1 is accomplished using an Electrostatic Extraction Channel, EEC, and two Magnetic Extraction Channels, MEC1 and MEC2.

The internal PIG source of SPC1 utilises electron oscillations in the presence of a strong magnetic field to increase the probability for charged particle

production [12]. To produce the electrons a heated filament, through which an electrical current passes, heats a pill-shaped pellet, the cathode [5]. The emitted electrons undergo collisions with the gas atoms producing charged particles. This process of charged particle production results in deterioration of, amongst others, the cathode and heating element, which leads to frequent servicing of the source. This is one of the major drawbacks of such an ion source.

2.2.3 The second solid-pole injector cyclotron, SPC2

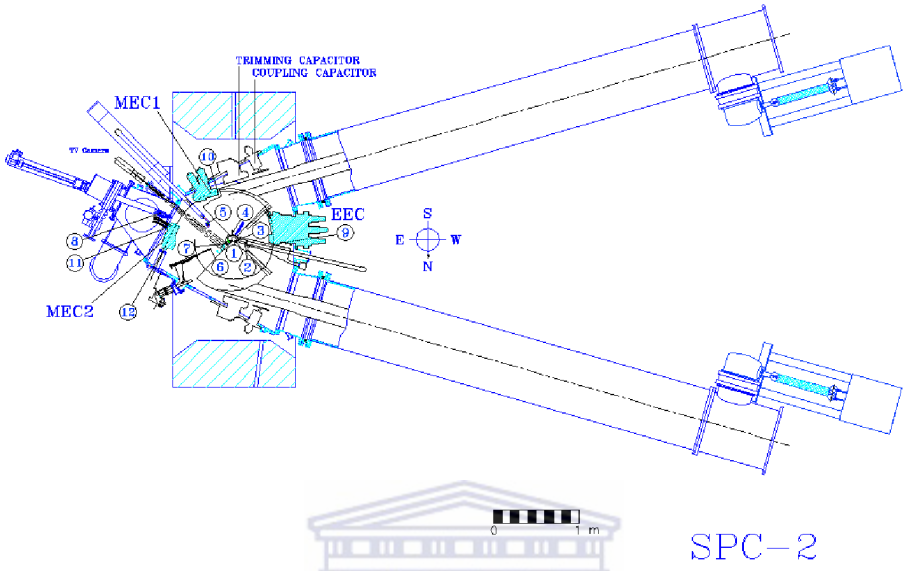

Figure 2.4: The layout of the major components in SPC2: 1, inflector collimators; 2, ΣΔR probe no.1; 3, RADAX slits; 4, 2nd radial slit; 5, ΣΔR probe no.2; 6, 2nd axial slit; 7, visual display plate; 8, harp; 9, EEC collimators; 10, 1st magnetic channel collimators and liner; 11, 2nd magnetic channel collimators and liner; 12, passive magnetic channel collimators.

Figure 2.4 shows the layout of SPC2, which is in many respects similar to SPC1. It is also a four-sector, solid-pole cyclotron with two 90° dees and an extraction radius of 0.476 m. A major difference however is that beams, transported via a transfer beamline, from either the polarised ion source or the ECR ion source, must be axially injected into SPC2 with a spiral inflector. To cover the range of energies and ion species, three interchangeable spiral inflectors are used.

2.2.4 The ion sources and injection beam lines of SPC2

Figure 2.5 shows the layout the two ECR ion sources, HMI ECRIS4 and GTS2, and connecting transfer beamlines in the ECR vault.

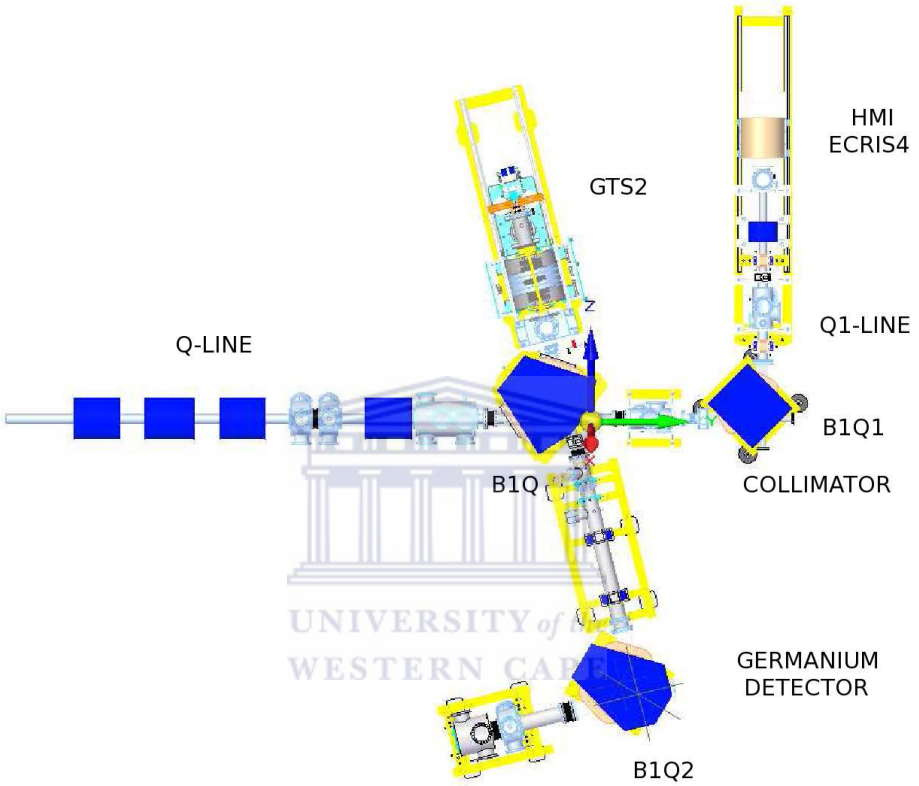

Figure 2.5: Layout of the ECR vault housing the two ECR ion sources, GTS2 and ECRIS4.

Figure 2.6 shows the layout of the two vaults housing the three ion sources and connecting transfer beamlines. The transfer beamline from the polarised ion source remains unchanged. However the ECR ion source shown in figure 2.6 and the part of the transfer beamline leading to bending magnet 1Q, B1Q, including B1Q has now been removed. This source has been replaced by the two ion sources shown in figure 2.5 and a new B1Q on a different position. It should be mentioned that the ECRIS4 is rotated through 180° relative to the old ECR ion source shown in figure 2.6.

Both injectors, SPC1 and SPC2, are situated at ground level. The horizontal median plane of each of these injectors are level with that of the SSC at 1.5 m above ground level [13]. From ground level, the SSC vault extends downwards, 4 metres, to the basement level. The three ion sources are located at basement level below SPC2. All three ion sources are mounted horizontally, with their horizontal median plane 1 m above basement floor level [13]. To transport the charged particle beam from this level to the injector, the beam is rotated vertically through 90° and transported via the axial, AX, transfer beamline into SPC2. The AX-beamline therefore goes through the concrete roof of the vault.

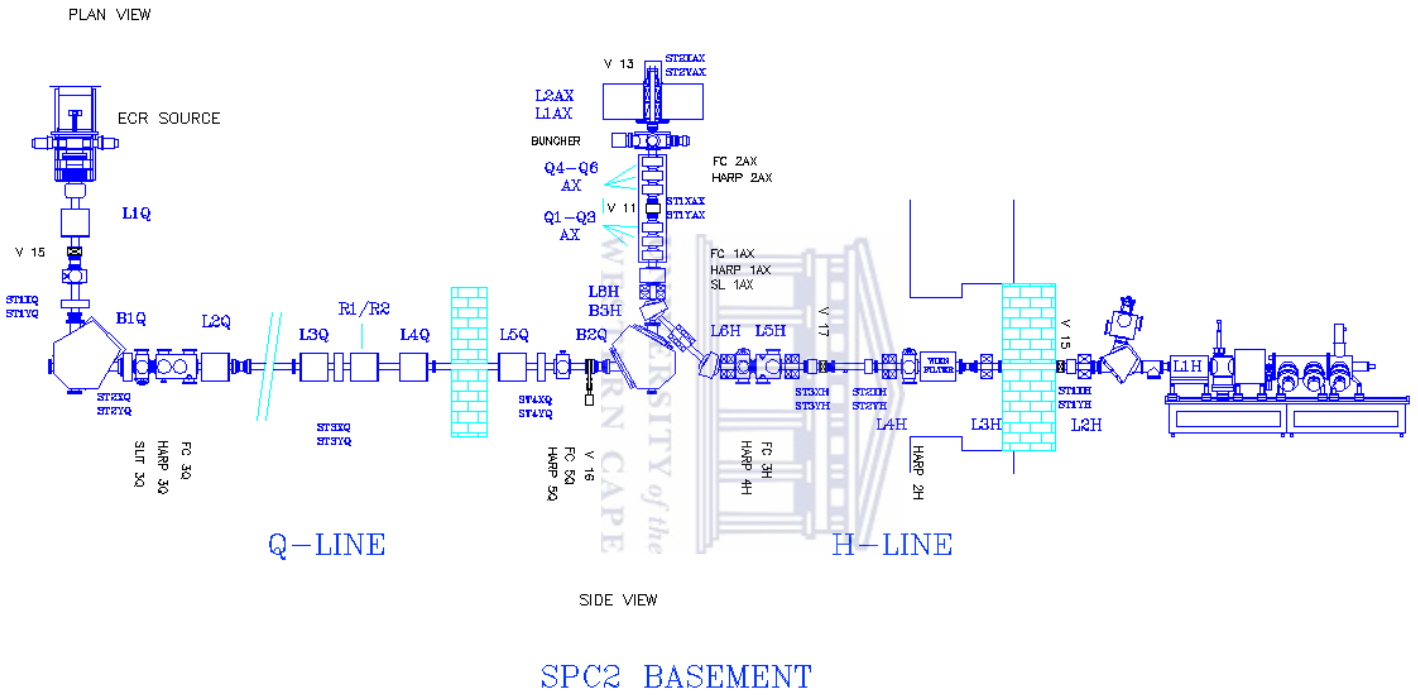

Figure 2.6: The layout of the two vaults housing the three ion sources and its connecting transfer beamlines.

The transfer beamline from the ECRIS4

The extracted charged particle beam from the ECRIS4 is focused with a solenoid magnet to the entrance of a pair of slits, thus achieving matching to the transfer beamline. If the charged particle beam is not properly matched to the transfer beamline, it might be lost against the walls of the vacuum chamber within B1Q1 shown in figure 2.5.

The particle beam then passes through a double-focusing 90° bending magnet. This bending magnet focuses the beam to a second pair of slits in the transfer beamline. Using the the solenoid magnet, the bending magnet and the first and second pair of slits in the transfer beamline, charge-state selection is accomplished [14]. The beam is then focused using an einzel lens before it enters the Q-line [15].

The ECR ion sources are located in a vault adjacent to the SPC2 cyclotron vault in the basement area. To transfer the beam of charge particles from this vault to the injector cyclotron at ground level, the beam must be bend through a 90° degree magnet and injected axially into the injector. This is accomplished using a so-called mirror symmetric system [14]. A mirror image of the beam is thus produced between two points along the transfer beamline. To accomplish this so-called achromaticity, six solenoids magnets, L2Q, L3Q, L4Q, L5Q, R1 and R2, are used.

The axial transfer beamline

To minimise beam losses, the emittance of the extracted beam must be matched to the injection requirements of the injector. This is accomplished using six quadrupole magnets, in the AX-line. These quadrupole magnets are arranged as two triplets. The two quadrupole triplets will focus the beam to a double waist at the entrance of the buncher in the AX-line [14]. Two additional solenoid magnets, L1AX and L2AX, focus the beam to a double waist at the entrance to the inflector [14].

The transfer beamline of the polarised ion source

The beam extracted from the polarised ion source is directed towards the downward projected axis of SPC2. Both charged particle beams from the ECR ion sources and the polarised ion source reach a focal point along the same point in the AX-line [14]. From extraction, the polarised beam is focused to a waist by the first solenoid magnet, L1H, in the transfer beamline.

An aperture at this point in the vacuum chamber will remove some of the unfocused particles [13]. A second set of solenoid magnets, L2H and L3H, form a beam waist at the position of the 'Wien Filter'.

The extracted beam from the ion source is polarised along the beam axis, either forwards or backwards [13]. Along the transfer beamline the polarised ions are rotated through 90° with the aid of two 45° bending magnets. This rotation of the beam causes the axis of polarisation to precess. The Wien Filter is the device used to correct for any precession of the polarised beam through the two 45° bending magnets [14].

The Wien Filter is followed by a second set of solenoid lenses, L4H and L5H, and the achromatic system of the polarised ion source beamline [13]. This is followed by the beam optics in the axial beamline as described earlier.

Chapter 3

Basic aspects of ECR plasma physics

The goal of this chapter is not to give an exhaustive explanation of the physics of electron cyclotron resonance ion source, ECRIS, plasmas. It is merely an attempt to highlight the basic aspects of ECR plasma physics. Additionally, it's meant to familiarise the reader with concepts and parameters that will be used later, to explain the results of the experimental work.

As a starting point, a definition is presented of what is meant by the word plasma. Subsequent to this, the complicated trajectory followed by a single particle, in a 'magnetic confinement field' is examined. This single particle examination is important, as the only plausible explanation for electron heating can be given for single particles only [4].

To determine a large number of plasma phenomena observed in experimental work, fluid description of plasmas is used, hence this topic is briefly discussed in the latter part of this chapter. The chapter is then concluded with an examination of the physics involved during the emission of photons in a plasma. Discussions about electron heating and the magnetic confinement field are deferred to Chapter 4.

3.1 Plasma parameters

3.1.1 Definition of a plasma

In the universe, four states of matter exist, of which the plasma state is the most abundant form of matter, yet encounters with this state of matter

is very much limited. In order for an 'ionised gas' to be classed as a plasma, it needs to satisfy three criteria.

A plasma may be defined as '*a quasineutral gas of charged and neutral particles, which exhibits collective behaviour*' [16]. Quasi-neutrality demands that:

$$n_e \cong \sum_{1}^{s} Z_s n_{is} \tag{3.1}$$

where

- Z_s is the charge state of the ionic species s
- n_{is} is the number of ions of ionic species s per cubic centimetre or ion density of ionic species s
- n_e is the number of electrons per cubic centimetre or electron density.

By quasi-neutrality, it is implied that when a potential is introduced into a plasma, the individual charged particles undergo motion inside the plasma, resulting in large electric fields being generated. The end result of such motion by the gas of charged particles is to shield-off the foreign potential. This phenomena is known as Debye shielding and results in a cloud of electrons surrounding the positive potential and a cloud of positive ions surrounding the negative potential. The thickness of this cloud of charged particles is called the Debye length, λ_D, and is a measure of the shielding distance of the plasma. It is assumed that there exists enough particles in each charge cloud to effect Debye shielding, meaning

$$N_D = \frac{4}{3} n \pi \lambda_D^3 \gg 1 \tag{3.2}$$

where

- N_D is the number of particles in the 'Debye sphere'
- n is the particle density.

This is the first condition an ionised gas must satisfy in order for it to be classed as a plasma.

Let L be the characteristic length of a plasma chamber housing a plasma. If the dimension L is much larger than the Debye length and a foreign potential is introduced into the plasma, the shielding distance will be much smaller than the dimension of the plasma. This will leave the major part of the plasma free of large electric potentials. The plasma is thus said to be quasineutral.

$$\lambda_D \ll L. \tag{3.3}$$

This constitutes the second criteria for qualification as a plasma.

The plasma, as mentioned previously, is a gas of charged and neutral particles. Charged particles tend to exert Coulomb forces on one another. Inside the plasma, the moving charged particles give rise to electric and magnetic fields. By collective behaviour it is implied that all possible forces are taken into account during the motion of charged particles inside the plasma. This leads to the third condition, which requires:

$$\omega_p \tau > 1 \tag{3.4}$$

where

- ω_p is the frequency of the plasma oscillations
- τ is the mean time between collisions.

Given that the ECRIS4 at iThemba LABS is operated with a 14.5 GHz microwave generator, the magnitude of some of the parameters discussed above can be estimated. If it is assumed that the electron density is in the region of 10^{10}cm^{-3} and 14.5 GHz microwaves are launched at the plasma chamber, the resonant magnetic field strength will be 0.518 T. For a plasma with an electron temperature of 20 keV and an electron density of 10^{10}cm^{-3}, the electron Debye length is 1.047 cm, much less than the length of the water-cooled plasma chamber of the ECRIS4. Additionally the number of electrons in the 'Debye sphere', given the electron density and Debye length above, will be 4.808×10^{10}. Assuming a mean time between collisions of 10^{-3} s and further assuming that the plasma frequency is equal to the electron plasma frequency, $\omega_p \cong \omega_{pe}$, we find that $\omega_p \tau = 5640$ rad > 1. This justifies our claims that the ionised gas of the ECRIS4 can be rightfully defined as a plasma.

3.2 Motion of single charged particles

The derivations in the following sections follows the book of Chen [16].

3.2.1 Motion of single charged particle in uniform E and B fields

It is well known that when a moving charged particle is exposed to a magnetic field, it experience a force which confines the trajectory to circular motion. If one point the two thumbs of your hands in the direction of the prevailing magnetic field, the fingers of the left hand curl in the direction of rotation of a positively charged particle, whilst the fingers of the right hand curl in the direction of rotation of the negatively charged particle.

Lets assume that a uniform magnetic field is directed along the z-axis ($\mathbf{B} = \mathrm{B}\hat{\mathbf{z}}$) and $\mathbf{E} = 0$, in a Cartesian coordinate system. The equation of motion for this situation can be expressed as follows:

$$m\frac{d\mathbf{v}}{dt} = q\left(\mathbf{v} \times \mathbf{B}\right) \tag{3.5}$$

where

- m is the mass of the particle
- q is the charge of the particle
- $\mathbf{v}$ is the velocity of the particle.

Separation of the x- and y-components of (3.5) leads to:

$$\ddot{v}_x = \frac{qB}{m}\dot{v}_y = -\left(\frac{qB}{m}\right)^2 v_x \tag{3.6}$$

$$\ddot{v}_y = -\frac{qB}{m}\dot{v}_x = -\left(\frac{qB}{m}\right)^2 v_y \tag{3.7}$$

$$\omega_c = \frac{|q|B}{m} \tag{3.8}$$

where ω_c is the frequency at which the charged particles orbit the field lines. This frequency is known as the cyclotron frequency of the orbiting charged particle.

One possible solution to (3.6) and (3.7) is:

$$v_{x,y} = v_{\perp} \exp\left(\pm i\omega_c t + \delta_{x,y}\right) \tag{3.9}$$

where the $\pm$ denotes the sign of the charged particles and $v_{\perp}$ denotes the speed of the charged particles in the plane perpendicular to $\mathbf{B}$. The phase angle δ may be chosen such that:

$$v_x = v_{\perp} e^{i\omega_c t} = \dot{x} \tag{3.10}$$

$$\frac{dv_x}{dt} = v_{\perp} i\omega_c e^{i\omega_c t} = \dot{v}_x. \tag{3.11}$$

Substituting (3.11) into (3.7) and solving for v_y results in:

$$v_y = \pm i v_{\perp} e^{i\omega_c t} = \dot{y}. \tag{3.12}$$

Integrating (3.10) and (3.12) one obtains

$$x - x_0 = -i\frac{v_{\perp}}{\omega_c}\left[e^{i\omega_c t} - 1\right] \tag{3.13}$$

$$y - y_0 = \pm\frac{v_{\perp}}{\omega_c}\left[e^{i\omega_c t} - 1\right] \tag{3.14}$$

where x_0 and y_0 are the x and y-coordinates at time t=0. The single particle motion can thus be described by circular motion around a guiding centre $(x_{\rm gc}, y_{\rm gc})$, which is fixed.

$$x_{\rm gc} = x_0 + i\frac{v_{\perp}}{\omega_c} \tag{3.15}$$

$$y_{\rm gc} = y_0 \mp i\frac{v_{\perp}}{\omega_c} \tag{3.16}$$

$$x - x_{\rm gc} = -i\frac{v_{\perp}}{\omega_c}\left[e^{i\omega_c t}\right] \tag{3.17}$$

$$y - y_{\rm gc} = \pm\frac{v_{\perp}}{\omega_c}\left[e^{i\omega_c t}\right]. \tag{3.18}$$

Using (3.19) one can separate the complex and the real parts of (3.17) and (3.18)

$$e^{i\omega_c t} = \cos\omega_c t + i\sin\omega_c t \tag{3.19}$$

The expressions for the real parts of (3.17) and (3.18) are given by the expressions below

$$x - x_{\rm gc} = r_L \sin(\omega_c t) \tag{3.20}$$

$$y - y_{\rm gc} = \pm r_L \cos(\omega_c t) \tag{3.21}$$

$$r_L = \frac{v_\perp}{\omega_c} \tag{3.22}$$

where r_L is the so-called Larmor radius or the gyro-radius of the charged particles. In the case of the ECRIS4, the mean gyro-radius of electrons at the ECR surface would be 1.07 mm for an average electron energy of 25 keV. This same result for a proton of average energy of 5 eV would be 0.69 mm.

Equations (3.20) and (3.21) describe circular motion around a guiding centre $(x_{\rm gc}, y_{\rm gc})$. The direction of circulation is always such that the magnetic field generated by the charged particle is opposite to the externally imposed magnetic field. The individual plasma particles therefore reduce the ambient magnetic field by superposition of this diamagnetic effect.

Lets now impose an electric field, confined to the $x - z$ plane, on the previous situation. The equation of motion is now described by:

$$m\frac{d\mathbf{v}}{dt} = q\left(\mathbf{E} + \mathbf{v} \times \mathbf{B}\right). \tag{3.23}$$

The transverse components of (3.23) are:

$$\frac{dv_x}{dt} = \frac{q}{m}E_x \pm \omega_c v_y \tag{3.24}$$

$$\frac{dv_y}{dt} = 0 \mp \omega_c v_x \tag{3.25}$$

$$\frac{dv_z}{dt} = \frac{q}{m}E_z. \tag{3.26}$$

In the case above case $\mathbf{E}$ is assumed to be confined to the $x-z$ plane, which implies that $E_y = 0$ and as in the previous case, $\mathbf{B} = \mathrm{B}\hat{\mathbf{z}}$, which implies that $B_x = B_y = 0$. Differentiating (3.24) and (3.25) and using the fact that $\mathbf{E}$ is uniform, one obtains:

$$\ddot{v}_x = -\omega_c^2 v_x \tag{3.27}$$

$$\ddot{v}_y = \mp\omega_c\left(\frac{q}{m}E_x \pm \omega_c v_y\right) = -\omega_c\left(v_y + \frac{E_x}{B}\right). \tag{3.28}$$

If one now write

$$\frac{d^2}{dt^2}\left(v_y + \frac{E_x}{B}\right) = -\omega_c^2\left(v_y + \frac{E_x}{B}\right)$$

then (3.28) reduces to (3.7) if one replaced v_y by $\left(v_y + \frac{E_x}{B}\right)$ in the latter equation. Equations (3.10) and (3.12) are therefore replaced by:

$$v_x = v_\perp e^{i\omega_c t} = \dot{x} \tag{3.29}$$

$$v_y = \pm i v_\perp e^{i\omega_c t} - \frac{E_x}{B} = \dot{y}. \tag{3.30}$$

Integrating (3.29) and (3.30) once and taking the real part of both equations result in

$$x - x_{\text{gc}} = r_L \sin(\omega_c t) \tag{3.31}$$

$$y - y_{\text{gc}} = \pm r_L \cos(\omega_c t) + \frac{E_x}{B} t. \tag{3.32}$$

The motion of such a charged particle is also circular as in the case of a uniform **B** field only, however superimposed on this motion is a drift of the guiding centre as a result of the **E** field. This drift comes about because the charged particle, during its circular trajectory, is accelerated in the **E** field for only half of its trajectory. For the remaining half of the trajectory, the charged particle is decelerated. During acceleration, it gains energy and its circular trajectory increases in radius, whilst it decreases in radius for the remaining trajectory as it loses kinetic energy. This drift is sometimes referred to as the $\mathbf{E} \times \mathbf{B}$ drift.

3.2.2 Motion of a single charged particle in any uniform field

Using (3.23), one can determine the drift of the guiding centre under the influence of any general force. To do this the centrifugal force, $m\frac{d\mathbf{v}}{dt}$, is ignored as it is well known that this force only produces the circular motion. Equation (3.23) then becomes:

$$q\left(\mathbf{E} + \mathbf{v} \times \mathbf{B}\right) = 0. \tag{3.33}$$

Taking the cross product of the above equation with **B** results in

$$\left[\mathbf{E} \times \mathbf{B}\right] = \left[\mathbf{v}\mathrm{B}^2 - \mathbf{B}\left(\mathbf{v} \cdot \mathbf{B}\right)\right].$$

The transverse components of this equation are

$$\mathbf{v}_{\perp \text{gc}} = \frac{\mathbf{E} \times \mathbf{B}}{\mathrm{B}^2}. \tag{3.34}$$

By substituting any general force $\mathbf{F}$ for the $q\mathbf{E}$ force in (3.33) one can determine the guiding centre drift caused by this general force

$$v_{\mathrm{f}} = \frac{1}{q}\left[\frac{\mathbf{F}\times\mathbf{B}}{\mathrm{B}^2}\right]. \tag{3.35}$$

3.2.3 Motion of a single charged particle in a non-uniform B field

Grad-B (∇B) Drift

Lets now examine the charged particle drift brought about by an inhomogeneous magnetic field. The specific case considered here is where the magnetic flux lines are straight, with a perpendicular gradient in the magnetic field strength, ∇B perpendicular to $\mathbf{B}$. For simplicity, it is assumed that the only $\mathbf{B}$ field component present, is in the z-direction, $\mathbf{B} = \mathrm{B}\hat{\mathbf{z}}$, and ∇B is in the y-direction.

Using Taylor's theorem, the variation of the magnetic field strength in the y-direction, $B_z(y)$, can be expressed by a sequence of approximations of the function, $\dfrac{dB_z}{dy}$, around a given point, by polynomials, the Taylor polynomials of that function, whose coefficients depend only on the derivatives of the function at that point. Taylor's theorem therefore gives an approximation, for x near a point a, of the form

$$f(x) \approx f(a) + f'(a)(x-a) + \frac{f''(a)}{2!}(x-a)^2 + ... + \frac{f^n(a)}{n!}(x-a)^n. \tag{3.36}$$

Using Taylor's theorem, B_z can be approximated at any y position using $\dfrac{\partial B_z}{\partial y}$ at $x_0 = 0$ and $y_0 = 0$ as long as the y position where we want to determine B_z is near the point $x_0 = 0, y_0 = 0$. Given this restriction, Taylor's theorem may be use to determine the magnetic field as follows:

$$B_z = B_0 + y\left(\frac{\partial B_z}{\partial y}\right) + ... \tag{3.37}$$

Examining the physical picture of the charged particle trajectory during such a '$\nabla\mathbf{B}$ drift', it can be shown that the radius of curvature of the gyro-orbit is smaller on the larger magnetic field side of the orbit and larger on the smaller magnetic field side of the orbit. Having arbitrarily chosen the magnetic field to lie in the z-direction and the gradient in magnetic field

strength to lie in the y-direction, it can be visualised that the drift will be in the x-direction. Referring to (3.35), it then becomes obvious that the 'general force' which causes this $\nabla\mathbf{B}$ drift must lie in the y-direction.

To determine this general force, F_y, the particle motion is time-averaged over many gyro-periods to give the gyro-averaged particle motion, also known as the guiding centre drift. The charged particle orbit in a homogeneous magnetic field, is given by (3.6) and (3.7). To determine the charged particle orbit in a magnetic field gradient, the same equations are used but the uniform magnetic field is substituted with the approximation given by Taylor's theorem, ignoring non-linear terms.

$$F_y = -qv_x B_z(y) = -qv_x \left[B_{gc} + (y - y_{\mathrm{gc}}) \frac{dB}{dy} \right] \tag{3.38}$$

where $B_z(y)$ have been approximated by

$$B_z(y) = B_{gc} + (y - y_{\mathrm{gc}}) \frac{dB}{dy}. \tag{3.39}$$

For this approximation to be valid, $r_{\mathrm{L}} \left(\dfrac{dB}{dy} \right) \ll B$. Thus the gyro-radius must be much smaller than the typical scale-length of the variation of the magnetic field. Substituting (3.10) and (3.18) into (3.38) results in

$$F_y = -q \left(v_\perp e^{i\omega_c t} \right) \left[B_{gc} \pm \frac{v_\perp}{\omega_c} \left(e^{i\omega_c t} \right) \frac{dB}{dy} \right].$$

Taking the real part of the result above gives

$$F_y = -qv_\perp \left(\cos \omega_c t \right) \left[B_{gc} \pm r_{\mathrm{L}} \left(\cos \omega_c t \right) \frac{dB}{dy} \right]. \tag{3.40}$$

The average of the first term in (3.40) over a full gyration is zero and the average of $\cos^2 \omega_c t$ is $\dfrac{1}{2}$ so that

$$\overline{F}_y = \mp qv_\perp r_{\mathrm{L}} \frac{1}{2} \left(\frac{dB}{dy} \right). \tag{3.41}$$

The guiding centre drift velocity as a result of a magnetic gradient is therefore given by

$$v_{\mathrm{gc}} = \frac{1}{q} \frac{\mathbf{F} \times \mathbf{B}}{B^2} = \frac{1}{q} \frac{\overline{F_y}}{|B|} \hat{x} = \mp \frac{v_\perp r_{\mathrm{L}}}{B} \frac{1}{2} \frac{dB}{dy} \hat{x}. \tag{3.42}$$

Since the choice of the y axis was arbitrary, this can be generalised to

$$v_{\nabla B} = \pm\frac{1}{2} v_{\perp} r_{\mathrm{L}} \frac{\mathbf{B} \times \nabla B}{B^2}. \tag{3.43}$$

This so-called grad-B drift is in opposite directions for electrons and positively charged ions, resulting in a current transverse to $\mathbf{B}$.

Curvature Drift

The second case of a non-uniform magnetic field to be considered is the case where the magnetic flux lines are locally curved, with a constant radius of curvature, R_c, and with the magnetic field strength, $|B|$, being locally constant. To solve the guiding centre drift that accompanies this magnetic field configuration, the problem is redefined in cylindrical coordinates (r, θ, z). The curvature of the magnetic flux lines is chosen to be in the azimuthal direction $\hat{\theta}$ and the variation of the magnetic field strength, if any, is chosen to be in the radial direction $\hat{\mathbf{r}}$.

As a result of their thermal motion, the plasma particles move along the magnetic flux lines in addition to spiralling along the flux lines. To solve for this motion, the frame of reference is transformed, from the inertial frame of reference, to the rotating frame of reference, that is moving with the particle along the magnetic flux lines. In this frame of reference, all the equations of motion are still valid except for the addition of a centrifugal 'pseudo force' in the radial direction. Redefining $v_{\parallel}^2$ as the average square velocity component parallel to $\mathbf{B}$, the average centrifugal force is given by

$$\mathbf{F}_{\mathrm{cf}} = \frac{m v_{\parallel}^2}{R_c} \hat{\mathbf{r}} = m v_{\parallel}^2 \frac{\mathbf{R}_c}{R_c^2}. \tag{3.44}$$

To determine the guiding centre drift caused by this force, (3.44) is substituted into (3.35) to yield the so-called curvature drift, v_{curv}, of the guiding centre.

$$v_{\mathrm{curv}} = \frac{1}{q} \frac{\mathbf{F}_{\mathrm{cf}} \times \mathbf{B}}{B^2} = \frac{m v_{\parallel}^2}{q B^2} \frac{\mathbf{R}_c \times \mathbf{B}}{R_c^2} \tag{3.45}$$

To determine the total drift of the more general case where the magnetic flux lines are curved with a constant local radius of curvature and accompanied by a decrease of $|B|$ with radius, one must determine the grad-B drift which accompanies this scenario. This can be shown to be equal to [16]:

$$v_{\nabla B} = \mp\frac{1}{2} \frac{v_{\perp} r_L}{B^2} \mathbf{B} \times |B| \frac{\mathbf{R}_c}{R_c^2} = \pm\frac{1}{2} \frac{v_{\perp}^2}{\omega_c} \frac{\mathbf{R}_c \times \mathbf{B}}{R_c^2 B} = \frac{1}{2} \frac{m}{q} v_{\perp}^2 \frac{\mathbf{R}_c \times \mathbf{B}}{R_c^2 B^2}.$$

Combining the above expression with (3.45) yields the total drift in a curved vacuum magnetic field

$$v_{\text{curv}} + v_{\nabla B} = \frac{m}{q}\frac{\mathbf{R}_c \times \mathbf{B}}{R_c^2 B^2}\left(v_{\parallel}^2 + \frac{1}{2}v_{\perp}^2\right) \tag{3.46}$$

where vacuum magnetic fields refer to the absence of volume currents in the plasma [17].

3.2.4 Magnetic mirrors

Lets now consider the case in which a gradient of B exists along the direction of $\mathbf{B}$. If it is assumed that this static magnetic field, B, is primarily pointing in the z-direction and one recalls Maxwell's equation, $\nabla \cdot \mathbf{B} = 0$, then the field lines must converge at some distance along the z-axis. Additionally it is assumed that the static magnetic field is axisymmetric with $B_\theta = 0$ and $\dfrac{\partial}{\partial\theta} = 0$.

Since the field lines must converge and diverge, the static magnetic field must have a B_r component. It can be shown that this magnetic field component gives rise to a force, F_z, which traps the particle in the magnetic field. Obtaining the average of this 'trapping force' over one gyration yields the following result [16]:

$$\overline{F}_z = -\frac{1}{2}\frac{mv_{\perp}^2}{B}\frac{\partial B_z}{\partial z}. \tag{3.47}$$

This allows one to define a parameter which is related to the rotational energy of the trapped, gyrating particle. This parameter is the magnetic moment, μ, of the gyrating particle,

$$\mu = \frac{1}{2}\frac{mv_{\perp}^2}{B} = \frac{E_{\perp}}{B} \tag{3.48}$$

where $E_\perp$ is the perpendicular component of the kinetic energy of the gyrating particle. As the particle gyrates around the magnetic field lines, it moves into regions of stronger and weaker B. During this process, its Larmor radius changes, but μ remains invariant. Assuming the particle's energy is conserved, it can be shown that the magnetic moment is time independent [16].

$$\frac{\partial\mu}{\partial t} = 0.$$

As the particle moves from a region of lower magnetic field, B_1, into a region of higher magnetic field, B_2, $E_\perp$ increases correspondingly to preserve the invariance of μ.

$$\frac{E_{\perp 1}}{B_1} = \frac{E_{\perp 2}}{B_2} = \mu$$

where

- $E_{\perp 1}$ is the component of the kinetic energy of the gyrating particle in the region where $B = B_1$
- $E_{\perp 2}$ is the component of the kinetic energy of the gyrating particle in the region where $B = B_2$

As the particle's total energy must be conserved, the parallel component of the kinetic energy of the gyrating particle must decrease as the particle moves from B_1 to B_2. Consequently the particle's velocity component parallel to the magnetic field line decreases as the magnetic field increases. The increasing magnetic field therefore acts as a mirror and reflects the charged particle. Two magnetic mirrors are used to form a magnetic bottle, used to confine charged particles.

Trapping of the charged particles is however not perfect and some of the charged particles will escape the magnetic bottle. Lets define the value of the magnetic field at the midplane of the magnetic bottle to be B_0. Lets further define the perpendicular component of the velocity of the gyrating particle as $v_\perp$ and the parallel component of the velocity of the gyrating particle as $v_{||}$. A particle with $v_\perp = v_{\perp 0}$ and $v_{||} = v_{||0}$ at the midplane of the magnetic bottle, will have $v_\perp = v_\perp^{'}$ and $v_{||} = 0$ at the reflection point, $B = B^{'}$, along the magnetic bottle.

In order for a particle to be reflected, the ratio $\frac{v_\perp}{v_{||}}$ must exceed some defined value. This ratio is commonly referred to as the pitch-angle, α. If the pitch-angle of the gyrating particle is smaller than some critical pitch-angle (α_0), then the particle is not reflected by the magnetic mirror. Using the invariance of μ

$$\frac{1}{2}\frac{mv_{\perp 0}^2}{B_0} = \frac{1}{2}\frac{mv_\perp^{'2}}{B^{'}} \tag{3.49}$$

and recalling the conservation of energy

$$v_\perp^{'2} = v_{\perp 0}^2 + v_{||0}^2 \equiv v^2. \tag{3.50}$$

Defining $v_\perp = v \sin\alpha$, where $v = |\mathbf{v}|$ and $\mathbf{v}$ is the velocity of the gyrating particle. Combining equations (3.49) and (3.50), one obtains

$$\frac{B_0}{B'} = \frac{v_{\perp 0}^2}{v_\perp'^2} = \frac{v_{\perp 0}^2}{v^2} = \sin^2\alpha \qquad \Rightarrow \qquad \alpha = \sin^{-1}\left[\frac{B_0}{B'}\right]^{\frac{1}{2}}.$$

If α does not exceed some critical value, α_0, then the particle will not be reflected by the magnetic mirror. Replacing B' by B_m, one can determine the critical pitch-angle, as well as the maximum magnetic field for particle reflection. This is given by:

$$\sin^2\alpha_0 = \frac{B_0}{B_m} \equiv \frac{1}{R_m} \tag{3.51}$$

where R_m is a parameter used to determine the mirror strength of a magnetic bottle called the mirror ratio.

3.3 Fluid description of the plasma

The derivations in the following sections follow the book of Goldston and Rutherford [17] as well as the book of Chen [16].

The typical plasma density in any specific plasma might be of the order 10^{12} ion-electron pairs per cm^{-3} [16]. Under the influence of **externally prescribed E** and **B** fields, each plasma particle follows a complicated trajectory as illustrated earlier. As a result of its motion, the individual charged particle alters the externally prescribed **E** and **B** fields. To make predictions of the plasma behaviour, one would have to solve the individual charged particle trajectory such that it generates the prescribed **E** and **B** field. This needs to be done with the explicit knowledge that the one variable, the charged particle's trajectory, alters the other, the prescribed **E** and **B** fields, and vice verse. In addition to all of this, all the parameters are time dependant.

Fortunately, solving simultaneously this large number of equations, seldom needs to be done, as a majority of plasma phenomena observed in real experiments, could be described by fluid mechanics.

3.3.1 The convective derivative

The equation of motion for a single charged particle exposed to an **E** and a **B** field is given by (3.23).

$$m\frac{d\mathbf{v}}{dt} = q\left(\mathbf{E} + \mathbf{v} \times \mathbf{B}\right).$$

In the absence of thermal motion and collisions, all the charged particles in a fluid element move together, and the average velocity of the charged particles in the fluid element is given by $\mathbf{u}$. The fluid equation of motion is obtained by multiplying the particle density with the familiar Lorentz force. This extends the Lorentz force to all the particles in the fluid element, assuming that the average velocity of the fluid element is the same as the particle velocity in (3.23).

$$mn\frac{d\mathbf{u}}{dt} = qn\left(\mathbf{E} + \mathbf{u} \times \mathbf{B}\right) \tag{3.52}$$

In (3.52), $\dfrac{d\mathbf{u}}{dt}$ is in the frame of reference moving with the particles. It is desired to have an equation of motion for a fluid element that is fixed in space. To accomplish this task, the so-called convective derivative is used, as defined in the book of Chen [16]

$$\frac{d\mathbf{G}(x,t)}{dt} = \frac{\partial \mathbf{G}}{\partial t} + \frac{\partial \mathbf{G}}{\partial x}\frac{dx}{dt} = \frac{\partial \mathbf{G}}{\partial t} + u_x\frac{\partial \mathbf{G}}{\partial x}. \tag{3.53}$$

Let the variable of interest in this case be designated by $\mathbf{G}$(x,t), where $\mathbf{G}$ is any property of the fluid in a one-dimensional x space. The time rate of change of this variable of interest, $\dfrac{d\mathbf{G}(x,t)}{dt}$, in the frame of reference moving with the particle, can be described by a term representing the change of $\mathbf{G}$ at a stationary point in space and a term describing the change of $\mathbf{G}$ as it moves with the fluid into a region of different $\mathbf{G}$. In three dimensions, (3.53) generalises to

$$\frac{d\mathbf{G}}{dt} = \frac{\partial \mathbf{G}}{\partial t} + \left(\mathbf{u} \cdot \nabla\right)\mathbf{G}. \tag{3.54}$$

If $\mathbf{G}$ is defined to be the fluid velocity $\mathbf{u}$, in the case of our fluid description of the plasma, (3.52) becomes

$$mn\left[\frac{\partial \mathbf{u}}{\partial t} + \left(\mathbf{u} \cdot \nabla\right)\mathbf{u}\right] = qn\left(\mathbf{E} + \mathbf{u} \times \mathbf{B}\right). \tag{3.55}$$

3.3.2 Continuity equation

Lets consider a differential element of volume in the shape of a cube. Lets now assume that this differential element of volume is bounded by six sides, parallel to their respective coordinate surfaces ($\pm \mathrm{d}x_2\mathrm{d}x_3, \pm \mathrm{d}x_1\mathrm{d}x_3$ and $\pm \mathrm{d}x_1\mathrm{d}x_2$). The number of particles, flowing out of the volume element, across the surface $\mathrm{d}x_2\mathrm{d}x_3$, per second, will therefore be $n\left\langle v_1\right\rangle \mathrm{d}x_2\mathrm{d}x_3$, where $\left\langle v_1\right\rangle$ is the average velocity of species of particles in the x_1-direction. Following a similar line of reasoning, one can determine an expression for the flow across

the other surfaces. Additionally it is assumed that no particles are gained or lost from the volume element, except as a result of flow of species of particles across the boundary surfaces. The rate of change of the number of particles in the cubic volume element is therefore:

$$\frac{\partial n}{\partial t}\mathrm{d}x_1\mathrm{d}x_2\mathrm{d}x_3 = -\left[n\left\langle v_1\right\rangle \mathrm{d}x_2\mathrm{d}x_3\right]_{x_1+dx_1} + \left[n\left\langle v_1\right\rangle \mathrm{d}x_2\mathrm{d}x_3\right]_{x_1} ...$$

If one now divide the expression above by $\mathrm{d}x_1\mathrm{d}x_2\mathrm{d}x_3$ and allow the cube to shrink to an infinitesimal size, the continuity equation is obtained:

$$\frac{\partial n}{\partial t} = -\sum \frac{\partial}{\partial x_i}\left(n\left\langle v_i\right\rangle\right).$$

Changing to vector notation and writing $\mathbf{u}$ for the average velocity, $\langle\mathbf{v}\rangle$, the continuity equation may be written as:

$$\frac{\partial n}{\partial t} + \nabla\cdot(n\mathbf{u}) = 0. \tag{3.56}$$

3.3.3 The pressure tensor

Extending the Lorentz force to all particles of a given species, per unit volume, results in:

$$\mathbf{F} = nq\left(\mathbf{E} + \mathbf{u}\times\mathbf{B}\right)$$

where $\mathbf{u}$ is the average velocity. The change in momentum density, $\dfrac{\partial\left(nm\mathbf{u}\right)}{\partial t}$, due to this force density, $\mathbf{F}$, is:

$$\frac{\partial\left(nm\mathbf{u}\right)}{\partial t} = \mathbf{F} = nq\left(\mathbf{E} + \mathbf{u}\times\mathbf{B}\right). \tag{3.57}$$

Lets now consider the change in momentum density, due to a particle flux in the x_1 direction as a result of x_2-directed momentum. It can be shown that the total flux of x_2-directed momentum in the x_1 direction is given by

$$\int mv_2v_1fd^3v$$

and by using the definition of f, this result can be written as $mn\left\langle v_1v_2\right\rangle$, where f is the distribution function of the chosen particle species [17]. The rate of change of x_2-directed momentum density, averaged over all of the particles, can now be expressed in terms of the divergence of fluxes of momentum across the various surfaces [17].

$$\frac{\partial\left(nmu_2\right)}{\partial t} = -\frac{\partial\left(nm\left\langle v_1v_2\right\rangle\right)}{\partial x_1} - \frac{\partial\left(nm\left\langle v_1v_2\right\rangle\right)}{\partial x_2} - \frac{\partial\left(nm\left\langle v_1v_2\right\rangle\right)}{\partial x_3}. \tag{3.58}$$

Momentum flux is closely related to a generalised definition of pressure, in the case where pressure is viewed as a tensor quantity, the so-called 'pressure tensor' [17], denoted by $\mathbf{P}$. A tensor could be described as physical quantities that makes a correspondence between one set of vectors to another set of vectors.

In the result derived in (3.55), the thermal motion of the individual plasma particles was explicitly omitted. If the thermal motion of the particles is taken into consideration, a pressure force arises, which has to be added to the right side of (3.55). This force arises due to the random motion of the plasma particles as they move in and out the fluid element under consideration.

Since no special properties of x_1 and x_2 was used in deriving (3.58), it can be replaced with the arbitrary suffixes i and j. The flux in the i direction of j-directed momentum is therefore just $P_{ij} + mnu_iu_j$. Using (3.58) and the relation between the pressure tensor and the momentum flux, the rate of change of j-directed momentum brought about by the particle fluxes across the various surfaces can now be determined [17]

$$\frac{\partial (mnu_j)}{\partial t} = -\sum_i \frac{\partial P_{ij}}{\partial x_i} - m\sum_i \frac{\partial}{\partial x_i}(nu_iu_j). \tag{3.59}$$

Reverting to vector notation and combining the two contributions, (3.58) and (3.57), to $\frac{\partial (nm\mathbf{u})}{\partial t}$ one obtains the 'momentum balance equation' [17]:

$$\frac{\partial (nm\mathbf{u})}{\partial t} = nq(\mathbf{E} + \mathbf{u}\times\mathbf{B}) - \nabla\cdot\mathbf{P} - \nabla\cdot(mn\mathbf{uu}). \tag{3.60}$$

One can expand the last term on the right hand side of (3.60) and rewrite the momentum balance equation, in its most standard form [17]:

$$mn\left[\frac{\partial \mathbf{u}}{\partial t} + (\mathbf{u}\cdot\nabla)\mathbf{u}\right] = qn(\mathbf{E} + \mathbf{u}\times\mathbf{B}) - \nabla\cdot\mathbf{P} - mS\mathbf{u}. \tag{3.61}$$

Often the term involving S, which represents the volume source and the volume sink terms, is neglected resulting in [17].

$$mn\left[\frac{\partial \mathbf{u}}{\partial t} + (\mathbf{u}\cdot\nabla)\mathbf{u}\right] = qn(\mathbf{E} + \mathbf{u}\times\mathbf{B}) - \nabla\cdot\mathbf{P}. \tag{3.62}$$

3.3.4 Collisions between the different species in a plasma

Any neutral plasma must at least have two different species, ions and electrons, present in the plasma volume. During collisions between these two plasma constituents, momentum is transferred.

Lets define a 'collision frequency', $\nu_{\alpha\beta}$, as the rate at which momentum is transferred, by collisions, from species α to species β. If it is further assumed that the rate at which momentum is transferred, is proportional to the difference between the mean velocities of the two species, then this rate of momentum transfer per unit volume is given by [17]:

$$R_{\alpha\beta} = -m_\alpha n_\alpha \nu_{\alpha\beta} \left(\mathbf{u}_\alpha - \mathbf{u}_\beta\right). \tag{3.63}$$

If this effect is included in the momentum balance equation, (3.62) becomes [17]

$$mn\left[\frac{\partial \mathbf{u}}{\partial t} + \left(\mathbf{u}\cdot\nabla\right)\mathbf{u}\right] = qn\left(\mathbf{E} + \mathbf{u}\times\mathbf{B}\right) - \nabla\cdot\mathbf{P} + \sum_\beta R_{\alpha\beta}. \tag{3.64}$$

where the summation is over all the species β with which particles of the species α can collide.

3.3.5 Single-fluid model of a fully ionised plasma

In the 'single-fluid' model of a fully ionised plasma, the plasma is modelled as a single hydrodynamic fluid, acted upon by electric and magnetic forces. This is called the magnetohydrodynamic, MHD, model. In this model, the plasma is treated as a single fluid with mass density

$$\rho = n_i M + n_e m_e \approx n\left(M + m_e\right) \approx nM$$

charge density

$$\sigma = \left(n_i - n_e\right) q$$

mass velocity

$$\mathbf{u} = \frac{\left(n_i M \mathbf{u}_i + n_e m_e \mathbf{u}_e\right)}{\rho} \approx \frac{\left(M\mathbf{u}_i + m_e \mathbf{u}_e\right)}{M + m_e} \approx \mathbf{u}_i + \left(\frac{m_e}{M}\right)\mathbf{u}_e$$

and current density

$$\mathbf{j} = q\left(n_i \mathbf{u}_i - n_e \mathbf{u}_e\right) \approx nq\left(\mathbf{u}_i - \mathbf{u}_e\right)$$

where

- $\mathbf{u}_i$ is the average ion velocity
- $\mathbf{u}_e$ is the average electron velocity
- M is the ion mass
- m_e is the electron mass.

In addition to this, if one multiply the individual electron and ion continuity equations with their respective particle masses and add the result together, the 'mass continuity equation' is obtained

$$\frac{\partial \rho}{\partial t} + \nabla \cdot (\rho \mathbf{u}) = 0. \tag{3.65}$$

Similarly, if the individual ion and electron continuity equations are subtracted from each other, the result yields the 'charge continuity equation'

$$\frac{\partial \sigma}{\partial t} + \nabla \cdot \mathbf{j} = 0. \tag{3.66}$$

Following this pattern if the individual ion and electron momentum balance equations are added it produces the combined 'single-fluid equation of motion'

$$\rho \frac{\mathrm{d}\mathbf{u}}{\mathrm{d}t} = \rho \left(\frac{\partial \mathbf{u}}{\partial t} + \mathbf{u} \cdot \nabla \mathbf{u} \right) = \sigma \mathbf{E} + \mathbf{j} \times \mathbf{B} - \nabla p. \tag{3.67}$$

One can obtain a second single-fluid equation, the single-fluid electron equation of motion, from the two individual fluid equations

$$\mathbf{E} + \mathbf{u} \times \mathbf{B} = \eta \mathbf{j} + \frac{\mathbf{j} \times \mathbf{B} - \nabla p_e}{nq} \tag{3.68}$$

where η is the plasma resistivity. To describe how the plasma pressure, p, changes with time, the *adiabatic law* is often assumed

$$\frac{\mathrm{d}}{\mathrm{dt}} \left(\frac{p}{\rho^\gamma} \right) = 0. \tag{3.69}$$

The system of equations for modelling the single-fluid plasma is completed with the four Maxwell's equations:

$$\nabla \times \mathbf{B} = \mu_0 \mathbf{j} + \frac{1}{c^2} \frac{\partial \mathbf{E}}{\partial t} \tag{3.70}$$

$$\nabla \times \mathbf{E} + \frac{\partial \mathbf{B}}{\partial t} = 0 \tag{3.71}$$

$$\nabla \cdot \mathbf{B} = 0 \tag{3.72}$$

$$\nabla \cdot (\epsilon_0 \mathbf{E}) = \sigma \tag{3.73}$$

where

- c is the speed of light
- ϵ_0 is the permittivity of free space
- μ_0 is the permeability of free space.

Modelling the plasma as a single, electrically conducting fluid, equations (3.65)-(3.73) provide a complete set of tools for determining the plasma equilibrium, self-consistently. This implies that the mere presence of the plasma itself, alters the externally imposed magnetic field configuration.

3.4 Origin of the radiation from an accelerated charge

The derivations in the following sections, follow the book of Jackson [18].

3.4.1 The radiation fields

To determine the radiation from an accelerated charge, one use as a starting point, Maxwell's equations, (3.70) - (3.73). To reduce Maxwell's equations to a smaller number of second-order equations, potentials are introduced. Defining $\mathbf{B}$ in terms of a vector potential:

$$\mathbf{B} = \nabla \times \mathbf{A}$$

(3.71) can then be written as:

$$\nabla \times \left(\mathbf{E} + \frac{\partial \mathbf{A}}{\partial t} \right) = 0. \tag{3.74}$$

From the vector identity

$$\nabla \times (\nabla \phi) = 0$$

one can deduce that the expression in (3.74), with the curl equal to zero, can be expressed as a gradient, ∇, of a scalar function, namely a scalar potential ϕ.

$$\mathbf{E} = -\frac{\partial \mathbf{A}}{\partial t} - \nabla \phi \tag{3.75}$$

Rewriting Maxwell's two inhomogeneous equations, (3.70) and (3.73), in terms of the potentials results in:

$$\nabla^2 \phi + \frac{\partial}{\partial t} (\nabla \cdot \mathbf{A}) = -\sigma \tag{3.76}$$

$$\nabla^2\mathbf{A} - \frac{\partial^2\mathbf{A}}{\partial t^2} - \nabla\left(\nabla\cdot\mathbf{A} + \frac{\partial\phi}{\partial t}\right) = \mu_0\mathbf{j}. \tag{3.77}$$

Maxwell's equations have now been reduced to a set of two coupled equations. To uncouple the equations, one choose a set of potentials $(\mathbf{A}, \phi)$ that satisfy the Lorentz condition below:

$$\nabla\cdot\mathbf{A} + \frac{\partial\phi}{\partial t} = 0. \tag{3.78}$$

After uncoupling the equations, one is left with two inhomogeneous wave equations, one for ϕ and one for $\mathbf{A}$.

$$\nabla^2\phi - \frac{\partial^2\phi}{\partial t^2} = -\sigma \tag{3.79}$$

$$\nabla^2\mathbf{A} - \frac{\partial^2\mathbf{A}}{\partial t^2} = -\mu_0\mathbf{j}. \tag{3.80}$$

The wave equations, (3.79) and (3.80) all have the same basic structure,

$$\nabla^2\psi - \frac{\partial^2\psi}{\partial t^2} = -f\left(\mathbf{x}, t\right) \tag{3.81}$$

where $f\left(\mathbf{x}, t\right)$ is a known source distribution. To solve equations of this type, Green's function for the wave operator is used. A Green's function is a type of function used to solve inhomogeneous differential equations, subject to specific initial conditions or boundary conditions.

Solving the potentials satisfying the inhomogeneous wave equations (3.79) and (3.80) using the Green's function yields:

$$\phi = \frac{1}{4\pi\epsilon_0}\int\frac{[\sigma]}{|\mathbf{x}-\mathbf{x}'|}d^3x' \tag{3.82}$$

$$\mathbf{A} = \frac{\mu_0}{4\pi}\int\frac{[\mathbf{j}]}{|\mathbf{x}-\mathbf{x}'|}d^3x'. \tag{3.83}$$

For a point charge of magnitude q, position $\mathbf{r}$(t) and velocity $\mathbf{v}$(t)

$$\sigma = q\delta(\mathbf{x}-\mathbf{r}(t)) \tag{3.84}$$

$$j = q\mathbf{v}\delta(\mathbf{x}-\mathbf{r}(t)). \tag{3.85}$$

Substituting (3.84) and (3.85) into (3.82) and (3.83) respectively, results in

$$\phi = \frac{q}{4\pi\epsilon_0}\left[\frac{1}{\kappa\mathbf{R}}\right] \tag{3.86}$$

$$\mathbf{A} = \frac{\mu_0 q}{4\pi}\left[\frac{\mathbf{v}}{\kappa \mathbf{R}}\right] \tag{3.87}$$

where $\mathbf{R} \equiv \mathbf{x} - \mathbf{r}$ is the vector from the charge to the field point and $\kappa = 1 - \dfrac{\mathbf{R}\cdot\mathbf{v}}{Rc}$. The potentials of the point charge are called the Liénard-Wiechert potentials.

The electric field may then be calculated from (3.75) to give [19]

$$E = \frac{q}{4\pi\epsilon_0}\left(\frac{1}{\kappa^3 R^2}\left(\hat{\mathbf{R}} - \frac{\mathbf{v}}{c}\right)\left(1 - \frac{v^2}{c^2}\right) + \frac{1}{c\kappa^3 R}\hat{\mathbf{R}} \times \left\{\left(\hat{\mathbf{R}} - \frac{\mathbf{v}}{c}\right) \times \frac{\dot{\mathbf{v}}}{c}\right\}\right) \tag{3.88}$$

where $\hat{\mathbf{R}} \equiv \dfrac{\mathbf{R}}{R}$. The magnetic field can be determined from:

$$\mathbf{B} = \frac{1}{c}\left[\hat{\mathbf{R}}\right] \times \mathbf{E}. \tag{3.89}$$

3.4.2 Angular distribution of radiation emitted by an accelerated charge

By closer inspection of (3.88), it becomes clear that the expression is divided into two parts, one which is independent of the acceleration called the 'velocity field' and another which is linearly dependant on $\dot{\beta} = \dfrac{\dot{\mathbf{v}}}{c}$, called the 'acceleration field' [18]. The velocity fields are essentially static fields, whereas the acceleration fields are typical radiation fields.

The instantaneous energy flux is given by the Poynting's vector,

$$\mathbf{S} = \mathbf{E} \times \mathbf{B}. \tag{3.90}$$

From (3.88) the radial component of Poynting's vector is

$$[\mathbf{S}\cdot\mathbf{n}] = \frac{q^2}{16\pi^2\epsilon_0 c R^2}\left(\frac{1}{\kappa^6}\left|\hat{\mathbf{R}} \times \left\{\left(\hat{\mathbf{R}} - \frac{\mathbf{v}}{c}\right) \times \frac{\dot{\mathbf{v}}}{c}\right\}\right|^2\right). \tag{3.91}$$

This expression gives the energy per unit area, per unit time, detected at an observation point, at the time t, due to radiation emitted by the charge at time $t' = t - \dfrac{R(t')}{c}$. To calculate the energy radiated during a finite period of acceleration, say from t'=T_1 to t'=T_2, one would write

$$W = \int_{t=T_1+\left[\frac{R(T_1)}{c}\right]}^{t=T_2+\left[\frac{R(T_2)}{c}\right]} [\mathbf{S}\cdot\mathbf{n}]\, dt = \int_{t'=T_1}^{t'=T_2} (\mathbf{S}\cdot\mathbf{n})\frac{dt}{dt'}dt'. \tag{3.92}$$

The quantity $(\mathbf{S}\cdot\mathbf{n})\,\dfrac{dt}{dt'}$ is therefore the power radiated per unit area in terms of the charge's own time. One can therefore define the power radiated per unit solid angle to be

$$\frac{dP(t')}{d\Omega} = \kappa R^2 \mathbf{S}\cdot\mathbf{n}. \tag{3.93}$$

With (3.93) for the Poynting's vector, the angular distribution is

$$\frac{dP(t')}{d\Omega} = \frac{q^2}{16\pi^2\epsilon_0 c}\left(\frac{1}{\kappa^5}\left|\hat{\mathbf{R}}\times\left\{\left(\hat{\mathbf{R}}-\frac{\mathbf{v}}{c}\right)\times\frac{\dot{\mathbf{v}}}{c}\right\}\right|^2\right). \tag{3.94}$$

The simplest example of (3.94) is linear motion in which β and $\dot{\beta}$ are parallel. If θ is the angle of observation measured from the common direction of β and $\dot{\beta}$ then (3.94) reduces to

$$\frac{dP(t')}{d\Omega} = \frac{q^2\dot{v}^2}{16\pi^2c^3}\frac{\sin^2\theta}{(1-\beta\cos\theta)^5}. \tag{3.95}$$

As $\beta\to 1$, the angular distribution is tipped forward, more and more, and increases in magnitude, as indicated schematically in [18].

3.4.3 Bremsstrahlung

When a charged particle is incident on a plasma, it undergoes collisions with the plasma constituents. During this process, energy is exchanged between the incoming charged particle and the plasma constituents. As a result, both the incoming charged particle and the plasma constituents, undergo acceleration, which results in the emission of radiation as dictacted by (3.88).

The radiation emitted during these collisions are frequently called braking radiation or bremsstrahlung. In the measurements reported on in this work, the interest was predominantly on the electron-ion and electron-electron collisions in the plasma. However, due to the design of the collimator system, the detector used in our experimental setup was able to also measure bremsstrahlung as a result of unconfined electrons striking the extraction electrode of the ECRIS.

From (3.93) one can deduce that angular distribution of the emitted bremsstrahlung is confined to a narrow cone in the direction of motion of the charged particle. Since the ECRIS4 has no radial port, measurement of the bremsstrahlung was confined to the axial direction only.

Since the measurements performed during this investigation were merely used to gauge the relative increase in electron temperature, measurement of only axial bremsstrahlung was accepted to be adequate. This assumption is largely based on the following two arguments. Energy imparted to the electrons is seldom purely radial and mostly also have an axial component. This implies axial acceleration of the electrons. Secondly electrons undergo collisions inside the plasma. During such collisions energy is transferred to the colliding electrons. Based on these arguments it is accepted that axial bremsstrahlung measurements gives an estimate of the relative increase in electron temperature as the ECRIS parameters are varied.

Chapter 4

Electron cyclotron resonance ion source (ECRIS)

After having introduced the complex motion of a single charged particle in an ECRIS and the fluid dynamics equations used to analyse the ECRIS plasma, the interaction of the plasma electrons with the externally launched microwaves were examined. These externally launched microwaves, selectively heat the electron populations inside the ECRIS via the process of Electron Cyclotron Resonance Heating, ECRH. The components of the magnetic confinement fields, used to confine the charged particles to the plasma chamber are also derived.

4.1 ECRIS operations

4.1.1 Operating principle of an ECRIS

The ECRIS in its most basic form is composed of a metal box, placed between a radial confinement field and a longitudinal confinement field. The vector sum of these magnetic fields are chosen such that it produces a minimum magnetic field, $\mathbf{B}_{\min}$, in the centre of the metal box and a maximum magnetic field at the walls of the box. Injected into this box, through a waveguide, are microwaves at high frequencies, typically in the gigahertz range. Through a different port on the ECRIS, the target element to be ionised is introduced. Depending on the nature of the materials, different options for introducing the target elements into the source are used.

When these target atoms, target molecules or target ions encounters an electron of sufficient energy, an energy exchange can occur. During this

exchange process, the electron transfers some of its kinetic energy to the internal motion of the particle, resulting in either ionisation or excitation. Once ionised, the equation of motion for a charged particle in the presence of a magnetic field and an electric field is given by the Lorentz force as shown in the discussion on single particle motion in Chapter 3.

The injected microwaves on the other hand are transformed by some means into so-called circularly polarised waves. These electromagnetic, EM, waves also gyrate around the magnetic field lines. When the conditions are such that the frequency of the EM waves is the same as the gyrofrequency of the circulating electrons, an efficient energy transfer occurs from the EM waves to the circulating electrons. This manner of energy transfer is called Electron Cyclotron Resonance Heating [4].

An 'ECR surface' is thus created where an electron crossing this surface will experience an increase in the velocity component perpendicular to the magnetic field lines [4]. In doing so, the electron acquires a high velocity, which exceeds the ionisation potential of many highly-charged ions. Such an electron thus possesses the ability to produce high-charge state ions via step-by-step electron-ion collisions. The end result of a number of these electron-ion collisions yields a 'plasma' containing a mixture of neutral atoms, electrons and ions.

4.1.2 Production of multiply charged ions

An atom is composed of a central, positively-charged nucleus, surrounded by a cloud of orbiting electrons. These electrons are positioned in consecutive shells housing different number of electrons. Each shell is further subdivided into subshells. An electron belonging to any of the outer shells is weakly bound to the positive nucleus of the atom and as such can be transformed into a free electron with minimal effort. As one progresses to the more inner shells, the electrons are more tightly bound to the nucleus and require more energy to be removed. The amount of energy needed to remove a bound electron is called the ionisation potential.

In a plasma, various types of collisions occur, however not all collisions lead to ionisation. The most important collisions, as far as multiply-charged ion production in an ECRIS is concerned, are the so-called binary inelastic collisions. Binary collisions deal with the interactions of one particle with another. The specific binary inelastic collision to be considered, is the encounter

of an electron with a target particle. To comment on the relative importance of these specific collisions on ionisation in the ECRIS, it is worthwhile to define some critical collision parameters.

As mentioned previously a number of collision types is possible in a plasma. The probability of any of these collisions occurring is given by the so-called collision cross-section, σ, for that specific collision. Due to the presence of the magnetic confinement structure in an ECRIS, cross-sections cannot be immediately applied [4]. More useful concepts related to the cross-section is the mean free path and the collision frequency, as the latter can immediately be compared to other plasma frequencies.

The average length of path an incoming particle travels before undergoing a specific collision, is called the mean free path, λ

$$\lambda = \frac{1}{n\sigma}. \tag{4.1}$$

The amount of time taken for a particle of speed v, to travel one mean free path is

$$\tau = \frac{v}{\lambda} \tag{4.2}$$

- where v is the speed of the travelling particle relative to the target particle.

The reciprocal of this time is called the collision frequency, ν, and represents the number of collisions per unit of time

$$\nu = \frac{1}{\tau}. \tag{4.3}$$

During an inelastic electron collision, an electron of sufficient energy interacts with the target particle and transfers a significant amount of energy to the internal motion of the target particle. During such an interaction, various ionisation mechanisms are possible. Lets consider the interaction between a target particle and a flux of electrons. If, by some means, one were able to keep the target particle exposed to the electron flux for a long time, the collision frequency between the target particle and the incoming electron flux will increase. The target particle will subsequently suffer a series of ionising collisions, each time dislodging a peripheral electron. This situation would ultimately result in the production of multiply-charged ions. This process takes place as follows:

$$e^- + A \longrightarrow e^- + A^+ + e^-$$

Early experiments proved the effectiveness of producing multiply-charged ions using successive collisions and as a result, this has become the accepted method of multiply-charged ion production [4].

However once ionised, various recombination reactions seek to reduce the charge state of the ions. The most dominant recombination reaction in ECRIS is the recombination of multiply-charged ions with neutral atoms [4]. During this process, a collision occurs between a multiply-charged ion and a neutral atom. The recombination of a multiply charged ion with a neutral atom takes places as follows:

$$A^{z+} + B^0 \longrightarrow (AB)^{z+} \longrightarrow A^{(z-1)+} + B^{1+}$$

A neutral atom collides with an ion, owing to the electrostatic force between them. As a result of this collision, a molecular ion is created, which splits into two particles as illustrated above. The charge state of the multiply-charged ion is reduced during this charge exchange process. From this discussion one can conclude that the population of high-charge states in an ECRIS is closely linked to the density of the neutral atoms.

4.1.3 Cross sections for ionisation and charge exchange

As it is generally accepted that single ionisation of an ion or atom is the dominant route for the production of multiply-charged ions, only the cross section for this particular reaction is considered. Using the Lotz formula [20], the cross section for single ionisation is given by:

$$\sigma_i = \frac{4.5 \times 10^{-14}}{T_e} \sum_{k=1}^{m} \frac{n_k}{I_k} \log \frac{T_e}{I_k} \quad \left[\mathrm{cm}^2\right] = \frac{4.5 \times 10^{10}}{T_e} \sum_{k=1}^{m} \frac{n_k}{I_k} \log \frac{T_e}{I_k} \quad \text{[b]} \quad (4.4)$$

where

- T_e is the electron energy
- m is the number of occupied subshells in the ion
- I_k is the ionisation potential of the k$^{\text{th}}$ electron in the subshell
- n_k is the number of electrons in the subshell.

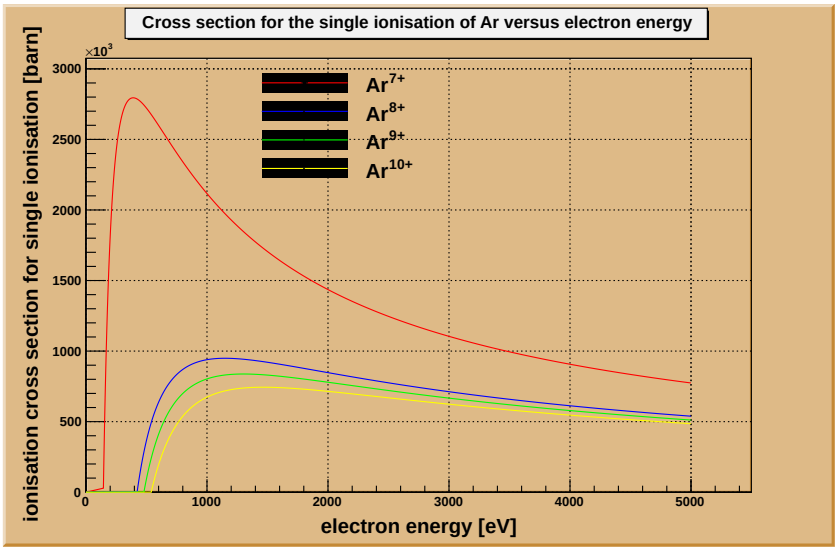

Figure 4.1: Calculated cross sections for single ionisation of Ar^{7+}, Ar^{8+}, Ar^{9+} and Ar^{10+} as a function of electron energy.

Figure 4.1 shows the single ionisation cross section for Ar^{7+} to Ar^{10+} calculated from the Lotz formula, equation (4.4). From this figure and from the Lotz formula it can be concluded that the electron energy for the maximum single ionisation cross section increases with charge states. The production of multiply charged ions therefore heavily relies on the ability to create energetic electrons inside the ECRIS.

Additionally the figure shows the dramatic decline of the cross section with increasing charge state. For Argon, the maximum cross section drops from 2.8×10^{-17} cm^2 for Ar^{7+} to 7×10^{-18} cm^2 for Ar^{10+}. For Xenon the maximum cross section in making the transition from Xe^{34+} to Xe^{35+} is 3.2×10^{-20} cm^2 at an electron energy of 4.4 keV. It should also be mentioned that the energy at maximum cross section increases with increasing charge state. During the production of high charge states the charge exchange cross section can at times be significant larger the ionisation cross section.

Charge exchange cross sections in the typical ECR energy region appear to be independent of electron energy [21]. For estimates of these charge exchange processes, references [22], [23] can be consulted.

4.2 The magnetic confinement system used in an ECRIS

The term 'magnetic field', **H**, refers to the magneto-motive force in a magnetic circuit and has units Am^{-1}. In a medium or in free space, this generates a magnetic flux of units Weber, Wb. The flux per unit cross section is referred to as the flux density or the induction. This entity has units of T (Tesla) and symbol **B**. Commonly, experts refer to the 'flux density' and the 'magnetic field' interchangeably. This practice may be justified as these two quantities have identical distributions in areas of constant magnetic permeability μ

$$\mathbf{H}=\frac{\mathbf{B}}{\mu}. \tag{4.5}$$

When distributions are the quantity of interest the term field will be used for both quantities.

In order for one to derive expressions for the different magnetic field components of the confinement system of an ECRIS, one starts with Maxwell's equations for magneto-statics:

$$\nabla \times \mathbf{H} = \mathbf{j} \tag{4.6}$$

$$\nabla \cdot \mathbf{B} = 0 \tag{4.7}$$

where **j** is the vector current density. Let's then make the assumption that electric currents are not present in the immediate region of the problem meaning

$$\mathbf{j} = 0.$$

This implies that the curl of the magnetic field is equal to zero, $\nabla \times \mathbf{H} = 0$. If the curl of a vector function is equal to zero, then the vector function can be expressed as the gradient of a scalar function

$$\mathbf{B} = -\nabla\phi. \tag{4.8}$$

In this case, the vector function is the induction, **B**, and the scalar function is the magnetic scalar potential, ϕ. Equation (4.8) can be expressed as follows in the cylindrical coordinate system:

$$B_r = -\frac{\partial\phi}{\partial r} \tag{4.9}$$

$$B_\theta = -\frac{1}{r}\frac{\partial\phi}{\partial\theta} \tag{4.10}$$

$$B_z = -\frac{\partial \phi}{\partial z} \tag{4.11}$$

where B_r, B_θ and B_z are the radial, azimuthal and axial components, of the field respectively.

$$\mathbf{B} = -\hat{\mathbf{r}}\frac{\partial \phi}{\partial r} - \hat{\theta}\frac{1}{r}\frac{\partial \phi}{\partial \theta} - \hat{\mathbf{z}}\frac{\partial \phi}{\partial z} \tag{4.12}$$

where $\hat{\mathbf{r}}$, $\hat{\theta}$ and $\hat{\mathbf{z}}$ are unit vectors in the cylindrical coordinate system. Substituting (4.8) into (4.7) yields the familiar Laplace's equation

$$\nabla \cdot \mathbf{B} = \nabla \cdot \nabla \phi = \nabla^2 \phi = 0. \tag{4.13}$$

Laplace's equation in cylindrical coordinates (r, θ, z) is:

$$\frac{\partial^2 \phi}{\partial r^2} + \frac{1}{r}\frac{\partial \phi}{\partial r} + \frac{1}{r^2}\frac{\partial^2 \phi}{\partial \theta^2} + \frac{\partial^2 \phi}{\partial z^2} = 0. \tag{4.14}$$

This equation will be used later to derive the magnetic field components of the hexapole of the ECRIS.

4.2.1 The axial field

Most laboratory plasmas are confined using a magnetic bottle. This magnetic structure is simply composed of two solenoid magnets separated by a fixed or variable distance. Since a solenoid magnet acts predominantly as an axial magnetic field, B_z, it cannot effectively confine particles in the radial direction.

Before deriving the magnetic field of a solenoid, the vector potential must first be reintroduced. Following a similar line of arguing, as was done in the case of the ϕ, one can conclude that if the divergence of a vector function is equal to zero, then it should be possible to express that vector function as the curl of some other vector function. Implementing this line of thinking results in:

$$\mathbf{B} = \nabla \times \mathbf{A} \tag{4.15}$$

where $\mathbf{A}$ is the vector potential. If one further defines:

$$\nabla \cdot \mathbf{A} = 0 \tag{4.16}$$

then by taking the curl of (4.15) one obtains:

$$\nabla \times \nabla \times \mathbf{A} = \nabla \times \mathbf{B} = \mu \mathbf{j} \tag{4.17}$$

where its now assumed that currents are present. By applying a vector identity, (4.17) becomes:

$$\nabla\left(\nabla\cdot\mathbf{A}\right)-\nabla^2\mathbf{A}=\mu\mathbf{j}. \tag{4.18}$$

Substituting (4.16) into (4.18) yields the result

$$\nabla^2\mathbf{A}=-\mu\mathbf{j}. \tag{4.19}$$

Lets now determine the vector potential $\mathbf{A}$ due to a current flow $\mathbf{j}$ in a solenoid of radius r_0. The solenoid consists of a single turn of thin wire or a single planar coil, of radius a and permeability μ, carrying a steady current J. In such a case, the only component of the vector potential is the azimuthal component, which implies:

$$\nabla^2 A_\theta=-\mu j_\theta \tag{4.20}$$

where $j_\theta=\dfrac{J}{\pi a^2}$ is the azimuthal current flowing in the solenoid. It can be shown that one possible solution for (4.20) is [24]

$$A_\theta=\cos\left[k\left(z-z_0\right)-\alpha_k\right]\left[A\left(k\right)I_1(kr)+B(k)K_1(kr)\right] \tag{4.21}$$

where k is the wave number and $I_1(kr)$ and $K_1(kr)$ are Bessel functions. r and z are the cylindrical coordinates of the field point and z_0 is the axial position of the coil . In the case of an ECRIS only the field inside the solenoid is of interest, $r<r_0$, hence one can exclude $K_1(kr)$ from the interior region of the solenoid [24], resulting in:

$$A_\theta=\int_0^\infty A\left(k\right)I_1(kr)\cos\left[k\left(z-z_0\right)\right]dk. \tag{4.22}$$

It can be shown that [24]

$$A(k)=\frac{\mu r_0 J}{\pi}K_1(kr_0) \tag{4.23}$$

leading to the potential

$$A_\theta=\frac{\mu r_0 J}{\pi}\int_0^\infty K_1(kr_0)I_1(kr)\cos\left[k\left(z-z_0\right)\right]dk. \tag{4.24}$$

Using the result obtained in (4.24), the magnetic field in cylindrical coordinates is given by [25]:

$$B_r\left(r,z,r_0,z_0\right)=-\frac{\partial}{\partial z}A_\theta\left(r,z,r_0,z_0\right) \tag{4.25}$$

$$B_z\left(r,z,r_0,z_0\right)=\frac{1}{r}A_\theta\left(r,z,r_0,z_0\right)+\frac{\partial}{\partial r}A_\theta\left(r,z,r_0,z_0\right). \tag{4.26}$$

Lets now express the Bessel function as a series, as follows [25]:

$$I_1=\left(\frac{1}{2}kr\right)\sum_{m=0}^{\infty}\left(\frac{1}{4}r^2\right)^m\frac{k^{2m}}{m!\Gamma\left(m+2\right)}\qquad\text{where}\qquad\Gamma(n)=(n-1)!. \tag{4.27}$$

By substituting (4.27) into (4.24) one obtains:

$$A_\theta=\frac{\mu r_0 J}{\pi}\int_0^\infty K_1(kr_0)\cos\left[k\left(z-z_0\right)\right]dk\left(\frac{1}{2}kr\right)\left[1+\frac{1}{4}\frac{r^2k^2}{\Gamma(3)}+\ldots\right]. \tag{4.28}$$

Inspecting (4.28), it is observed that the lowest order expression contains a term $k\cos\left[k\left(z-z_0\right)\right]$ and the next higher order expression has a term $k^3\cos\left[k\left(z-z_0\right)\right]$ and as the series continues to infinity, so also does this pattern. One can also note that:

$$k\cos\left[k\left(z-z_0\right)\right]=\frac{\partial}{\partial z}\sin\left[k\left(z-z_0\right)\right] \tag{4.29}$$

$$k^3\cos\left[k\left(z-z_0\right)\right]=-\frac{\partial^3}{\partial z^3}\sin\left[k\left(z-z_0\right)\right] \tag{4.30}$$

Substituting the algebraic manipulations above into (4.28) yields the result

$$A_\theta=\frac{\mu r_0 J}{\pi}\int_0^\infty K_1(kr_0)\frac{1}{2}rdk\frac{\partial}{\partial z}\sum_{m=0}^{\infty}\frac{(-1)^m\left(\frac{1}{4}r^2\right)^m}{m!\Gamma\left(m+2\right)}\frac{\partial^{2m}}{\partial z^{2m}}\sin\left[k\left(z-z_0\right)\right]. \tag{4.31}$$

Evaluating the integral over k result in [26]

$$\int_0^\infty K_1(kr_0)\sin\left[k\left(z-z_0\right)\right]dk=\frac{\pi}{4}\frac{2\left(z-z_0\right)}{r_0\sqrt{r_0^2+\left(z-z_0\right)^2}}. \tag{4.32}$$

If one now defines

$$A_0(z,r_0,z_0)=\frac{\partial}{\partial z}\frac{(z-z_0)}{\sqrt{r_0^2+\left(z-z_0\right)^2}} \tag{4.33}$$

and substitute the result obtained in (4.32) and the definition in (4.33) into (4.31), then one finds the result:

$$A_\theta\left(r,z,r_0,z_0\right)=\frac{\mu J}{2}\frac{r}{2}\sum_{m=0}^{\infty}\frac{(-)^m\left(\frac{1}{4}r^2\right)^m}{m!\Gamma\left(m+2\right)}\frac{\partial^{2m}}{\partial z^{2m}}A_0(z,r_0,z_0). \tag{4.34}$$

From the result obtained in (4.34) one can derive expressions for the vector potential, A_θ, and the two cylindrical magnetic field components, B_r and B_z, for the solenoid in the region $r < r_0$. Lets model the solenoid as a thick cylindrical current sheet with the following dimensions:

- inner radius : R_1
- outer radius : R_2
- axial length : $2L$.

Lets then integrate (4.33) over r_0 and z_0 to yield the result [27]

$$A_0(z, L, R_1, R_2) = -\left[(z - z_0)\ln\left(r_0 + \sqrt{r_0^2 + (z - z_0)^2}\right)\right]. \tag{4.35}$$

The vector potential may then be expressed as a power series expansion in r as follows:

$$A_\theta(r, z) = \frac{\mu r_0 J}{4L(R_2 - R_1)}\left[\frac{1}{2}rC_1 - \frac{1}{16}r^3C_3 + \frac{1}{384}r^5C_5 - \frac{1}{18432}r^7C_7 + \ldots\right]|_{-L}^{L}|_{R_1}^{R_2} \tag{4.36}$$

where the coefficients are defined as follows:

$$C_{i+1} = \frac{\partial^i}{\partial z^i}A_0(z, L, R_2, R_1). \tag{4.37}$$

The radial and axial magnetic field components are then given by:

$$B_r(r, z) = -\frac{\mu r_0 J}{4L(R_2 - R_1)}\left[\frac{1}{2}rC_2 - \frac{1}{16}r^3C_4 + \frac{1}{384}r^5C_6 - \frac{1}{18432}r^7C_8 + \ldots\right]|_{-L}^{L}|_{R_1}^{R_2} \tag{4.38}$$

$$B_z(r, z) = \frac{\mu r_0 J}{4L(R_2 - R_1)}\left[C_1 - \frac{1}{4}r^2C_3 + \frac{1}{64}r^4C_5 - \frac{1}{2304}r^6C_7 + \ldots\right]|_{-L}^{L}|_{R_1}^{R_2}. \tag{4.39}$$

Typically, in an ECRIS, the solenoidal fields are produced with electromagnets powered with DC supplies. In the older generation ECRIS, two such solenoidal coils were used, termed the injection and extraction coils. The newer generation ECRIS employs a third such coil placed between the injection and extraction coil. This coil, sometimes referred to as the centre coil, is used to adjust the so-called minimum magnetic field, $\mathbf{B}_{\min}$. To enhance particle extraction from the ion source, the magnetic field at injection is usually higher than the magnetic field at extraction.

To increase the magnetic field at the injection region of the ion source, an 'iron plug' is sometimes employed. This decreases the stray magnetic field and consequently increases the magnetic field inside the ECRIS. In the case of the ECRIS4, this field strength is typically 1.5 T.

4.2.2 The radial field

Solenoidal fields, such as the ones derived in the previous section, are very effective for axial confinement of multiply-charged particles. However, to confine such particles radially as well, one needs a field whose strength increases with radius. For this purpose, in an ECRIS, various multipolar fields have been investigated. As a result of these investigations, the majority of ECR ion sources operational today use a hexapolar field for radial confinement of the multiply-charged particles.

Lets now derive an expression for the magnetic field components of a hexapolar field. The symmetry conditions for a $2m$-pole magnet with $m = 1, 2, 3, \ldots$ are as follows:

$$\phi(r, \theta, z) = -\phi(r, -\theta, z) \tag{4.40}$$

$$\phi(r, \theta, z) = -\phi\left(r, \frac{\pi}{m} + \theta, z\right). \tag{4.41}$$

In an attempt to find a solution to Laplace's equation, the magnetic scalar potential is expressed as a Fourier series

$$\phi(r, \theta, z) = \sum_{n=1}^{\infty} a_n(r, z) \sin(n\theta - \theta_n). \tag{4.42}$$

By substituting the symmetry condition (4.41) into (4.42) and using the trigonometric identities, it can be shown that any specific multipole magnet with $2m$ poles is restricted to the following values of n [28]:

$$n = m, 3m, 5m, \ldots$$

Applying the restriction above, the magnetic scalar potential for a symmetric $2m$-pole magnet is expressed as follows:

$$\phi(r, \theta, z) = \sum_{n=m,3m,\ldots}^{\infty} a_n(r, z) \sin(n\theta - \theta_n). \tag{4.43}$$

Substituting (4.43) into (4.14) yields the result

$$\sum_{n=m,3m,\ldots}^{\infty}\left[\frac{\partial^2 a_n}{\partial r^2}+\frac{1}{r}\frac{\partial a_n}{\partial r}+\frac{\partial^2 a_n}{\partial z^2}-\frac{n^2}{r^2}a_n\right]\sin\left(n\theta-\theta_n\right)=0. \tag{4.44}$$

Since (4.44) needs to be valid for all values of θ, the following expression is true:

$$\frac{\partial^2 a_n}{\partial r^2}+\frac{1}{r}\frac{\partial a_n}{\partial r}+\frac{\partial^2 a_n}{\partial z^2}-\frac{n^2}{r^2}a_n=0. \tag{4.45}$$

Additionally $a_n(r,z)$ can be be expressed as a power series expansion in r [28]

$$a_n(r,z)=\sum_{l=1}^{\infty}C_{n,l}(z)r^l. \tag{4.46}$$

By substituting (4.46) into (4.45) and simplifying, it can be shown that [28]:

$$C_{n,l}=\frac{-1}{\left(l^2-n^2\right)}\frac{d^2}{dz^2}C_{n,l-2}. \tag{4.47}$$

Further on, it can be shown that

$$a_n(r,z)=\sum_{i=0}^{\infty}\frac{(-)^i\,n!r^{n+2i}}{4^i\,(n+i)!i!}\frac{d^{2i}K_n}{dz^{2i}} \tag{4.48}$$

where $C_{n,n}(z)=K_n(z)$. By substituting (4.48) into (4.43) one obtain the magnetic scalar potential for a multipole magnet with $2m$ poles, for which the symmetry conditions are valid.

$$\phi(r,\theta,z)=\sum_{n=m,3m,\ldots}^{\infty}r^n\sin(n\theta-\theta_n)\sum_{i=0}^{\infty}\frac{(-)^i\,n!r^{2i}}{4^i\,(n+i)!i!}\frac{d^{2i}K_n}{dz^{2i}} \tag{4.49}$$

For a magnet, for which the symmetry conditions are not valid, the magnetic scalar potential can be expressed in terms of the $2m$-pole magnetic scalar potential.

$$\phi(r,\theta,z)=\sum_{m=1,2}^{\infty}\phi_m(r,\theta,z)$$

$$\phi(r,\theta,z)=\sum_{m=1}^{\infty}\sum_{n=1}^{\infty}\nu_{m,n}r^n\sin(n\theta-\theta_n)\sum_{i=0}^{\infty}\frac{(-)^i\,n!r^{2i}}{4^i\,(n+i)!i!}\frac{d^{2i}K_{m,n}}{dz^{2i}} \tag{4.50}$$

where

$$\nu_{m,n}=\begin{cases}1 & \text{for}\quad n=m,3m,5m,\ldots\\ 0 & \text{for all other values of}\quad n.\end{cases}$$

The subscripts n and m in the term $K_{m,n}$ indicate the specific multipole, $n = 1$ for the dipole, $n = 2$ for the quadrupole, $n = 3$ for the hexapole, etc, and the specific boundary conditions for Laplace's equation, respectively.

$$\Phi(r, \theta, z) = \Phi\left(r, \frac{\pi}{m} + \theta, z\right)$$

By substituting (4.50) into (4.9), (4.10) and (4.11) one obtains the radial, azimuthal and axial magnetic field components, respectively.

$$B_r = -\sum_{m=1}^{\infty}\sum_{n=1}^{\infty} \nu_{m,n} n r^{n-1} \sin(n\theta - \theta_{m,n}) \sum_{i=0}^{\infty} \frac{(-)^i (n-1)!(n+2i) r^{2i}}{4^i (n+i)! i!} \frac{d^{2i} K_{m,n}(z)}{dz^{2i}} \tag{4.51}$$

$$B_\theta = -\sum_{m=1}^{\infty}\sum_{n=1}^{\infty} \nu_{m,n} n r^{n-1} \cos(n\theta - \theta_{m,n}) \sum_{i=0}^{\infty} \frac{(-)^i n! r^{2i}}{4^i (n+i)! i!} \frac{d^{2i} K_{m,n}(z)}{dz^{2i}} \tag{4.52}$$

$$B_z = -\sum_{m=1}^{\infty}\sum_{n=1}^{\infty} \nu_{m,n} r^{n-1} \sin(n\theta - \theta_{m,n}) \sum_{i=0}^{\infty} \frac{(-)^i n! r^{2i}}{4^i (n+i)! i!} \frac{d^{2i} K_{m,n}(z)}{dz^{2i}} \tag{4.53}$$

This hexapolar field introduces the magnetic mirror effect in the radial direction, as defined by the cylindrical coordinate system. With such a hexapolar field, the total magnetic field strength at given radius is constant and increases as a function of r^2.

The hexapolar field consists of six poles and is formed by permanent magnets, usually made from NdFeB. The hexapole is cylindrical in shape and made up in the so-called Halbach structure [29]. To enhance the magnetic field a so-called closed structure is used. This implies that the entire volume between the poles of the hexapole is filled with a magnetic material. A typical field strength for the hexapole is 1 T, at the wall of the plasma chamber.

4.3 The interaction of electromagnetic waves with a plasma

In general, the fluid plasma equations (3.65 - 3.73) derived earlier, do not necessarily represent a set of linear differential equations. If one considers any specific quantity in these equations, say the density, and it is assumed that this quantity oscillates sinusoidally at a given frequency, ω, one can linearise the fluid plasma equations by assuming that the oscillations are

small neglecting second- and higher order terms. Thus, any sinusoidally oscillating quantity, in the linear regime, can be represented in exponential notation. Using this notation, the density, n, can be written as follows:

$$n = \bar{n}e^{[i(\mathbf{k}\cdot\mathbf{r}-\omega t+\delta)]} \tag{4.54}$$

where

- $\bar{n}$ is a constant defining the amplitude of the wave
- $\mathbf{k}$ is the vector wave-number or the propagation constant
- δ is the phase of the quantity
- t is the time
- $\mathbf{r}$ is the position vector.

Additionally one needs to define the terms perpendicular, parallel, longitudinal, transverse, electrostatic and electromagnetic, as these terms will be frequently used in the discussions that follow. The terms parallel and perpendicular will be used to describe the direction of $\mathbf{k}$, relative to the static magnetic field, $\mathbf{B}_0$. Similarly the terms longitudinal and transverse will be used to describe the direction of $\mathbf{k}$, relative to the oscillating electric field, $\mathbf{E}_1$. Lastly if an oscillating magnetic field, $\mathbf{B}_1$, is absent, then the wave is electrostatic, otherwise it is electromagnetic, EM [17].

4.3.1 Plasma oscillations

When a cloud of electrons is displaced, in an unmagnetised plasma, from its initial position, there will be a nature tendency to restore this electron cloud to its unperturbed position. This restoring force comes about because of the electric field generated between the electron cloud and its 'unshielded ions' in the macroscopically neutral plasma. As a result of the restoring force, the cloud of electrons gains kinetic energy in the process. When the electron cloud, under the actions of the restoring force, arrives at its unperturbed position, it overshoots this position, as a result of its kinetic energy and the electron's inertia. Owing to the initial displacement, the electron cloud will therefore oscillate around its unperturbed position. This process is called Langmuir oscillations and the frequency at which the electron cloud oscillates is called the electron plasma frequency, ω_{pe}.

The electron plasma frequency is a very important timescale in ECRIS plasmas. From the discussion above, one can conclude that the electron plasma frequency is directly related to how fast the plasma electrons respond to a foreign potential introduced into the plasma. This leads to the conclusion that the quasi-neutrality referred to in Chapter 3 is only valid for timescales greater then the plasma period. In the case of the ECRIS4, quasi-neutrality would only apply for timescales greater then a few nanoseconds.

To derive an expression for the electron plasma frequency, it is assumed that the plasma is unmagnetised, $\mathbf{B} = 0$, and that a finite scalar electron pressure exists. The electron equation of motion and the electron continuity equation are then given by:

$$mn_e \left[\frac{\partial \mathbf{u}_e}{\partial t} + (\mathbf{u}_e \cdot \nabla)\, \mathbf{u}_e \right] = -qn_e \mathbf{E} - \nabla p_e \tag{4.55}$$

$$\frac{\partial n_e}{\partial t} + \nabla \cdot (n_e \mathbf{u}_e) = 0. \tag{4.56}$$

Generally, Poisson's equation is not used to solve for the $\mathbf{E}$ field in a plasma. This is a consequence of the so-called 'plasma approximation' [16]. In a plasma, as a result of movement of the ions, the electrons will also move in response to the ion movement. The $\mathbf{E}$ field must therefore adjust itself to preserve neutrality. Poisson's equation can therefore only be used to determine the charge density, σ, as this quantity adjusts itself to satisfy Poisson's equation. This result is however true only for low-frequency motions [16]. As the oscillations considered here are high-frequency oscillations, Poisson's equation can be applied to find $\mathbf{E}$.

$$\epsilon_0 \nabla \cdot \mathbf{E} = q\,(n_i - n_e) \tag{4.57}$$

To linearise the equations, the dependant variables are separated into two parts: an 'equilibrium part', denoted by a subscript 0 and a 'perturbation part', denoted by a subscript 1 [16]. The equilibrium part represents the state of the plasma prior to the perturbation being applied. Lets assume that the plasma was uniform and neutral before the electron cloud was displaced. As only electrons are considered, the subscript 'e' is dropped.

$$\nabla n_0 = \mathbf{u}_0 = \mathbf{E}_0 = 0$$

$$\frac{\partial n_0}{\partial t} = \frac{\partial \mathbf{u}_0}{\partial t} = \frac{\partial \mathbf{E}_0}{\partial t}$$

Linearising (4.55)

$$m\left[\frac{\partial \mathbf{u}_1}{\partial t} + (\mathbf{u}_1 \cdot \nabla)\,\mathbf{u}_1\right] = -q\mathbf{E}_1 - \nabla p_e$$

it is observed that the term $(\mathbf{u}_1 \cdot \nabla)\,\mathbf{u}_1$ has a second-order amplitude quantity and as such, one can neglect this term. Similarly by linearising (4.56)

$$\frac{\partial n_1}{\partial t} + \nabla \cdot (n_0\mathbf{u}_1 + n_1\mathbf{u}_1) = 0$$

the term $n_1\mathbf{u}_1$ also has a second-order amplitude quantity and as such, this term can also be neglected.

$$\frac{\partial n_1}{\partial t} + n_0\nabla \cdot \mathbf{u}_1 + \mathbf{u}_1 \cdot \nabla n_0 = 0$$

Given that $\nabla n_0 = 0$, the term $\mathbf{u}_1 \cdot \nabla n_0$ can also be neglected. In Poisson's equation, (4.57), it is noted that $n_{i0} = n_{e0}$ and that $n_{i1} = 0$ by the assumption that the ions are essentially stationary. Poisson's equation therefore becomes

$$\epsilon_0 \nabla \cdot \mathbf{E}_1 = -qn_1.$$

In this analysis the oscillating quantities are assumed to behave sinusoidally. Additionally the assumption is made that the electrons move in the direction of propagation of the plane wave and the electric field points in this direction as well. It is further assumed that the wave is propagating in the x direction.

$$\mathbf{u}_1 = u_1 e^{i(kx-\omega t)}\hat{x}$$
$$n_1 = n_1 e^{i(kx-\omega t)}$$
$$\mathbf{E} = Ee^{i(kx-\omega t)}\hat{x}$$

The pressure perturbation, p_1, needs to be related to n_1. It can be shown that [17]:

$$p_1 = \gamma k_{\mathrm{B}} T n_1 \qquad \text{where} \qquad \gamma = 3$$

where

- k_{B} is the Boltzmann constant
- $\gamma = \dfrac{(2+N)}{N}$ is a quantity that relates the increase in temperature of a plasma to the amount of compression applied to the plasma and N is the number of degrees of freedom which was chosen to be 1

- T is the temperature of the plasma.

From this point onwards the Boltzmann constant will be dropped as it serves merely to convert temperature from degrees Kelvin to units of energy. The equation above will then read as follows, $p_1 = \gamma T n_1$ with T expressed in units of energy.

Linearising the equation of motion of the electron fluid, one finds

$$\begin{aligned} mn_e\frac{\partial \mathbf{u}_1}{\partial t} &= -qn_e\mathbf{E}_1 - \nabla p_e \\ -i\omega mn_0u_1 &= -qn_0E_1 - ikp_1 \\ i\omega mn_0u_1 &= qn_0E_1 + 3ikTn_1. \end{aligned} \tag{4.58}$$

Similarly one can linearise the electron continuity equation:

$$-i\omega n_1 + ikn_0u_1 = 0 \tag{4.59}$$

and Poisson's equation

$$ik\epsilon_0E_1 = -qn_1. \tag{4.60}$$

Solving (4.59) for n_0u_1

$$n_0u_1 = \frac{\omega}{k}n_1 \tag{4.61}$$

and (4.60) for E_1

$$E_1 = \frac{-qn_1}{ik\epsilon_0} \tag{4.62}$$

and substituting (4.61) and (4.62) into (4.58), one obtains

$$\frac{i\omega^2mn_1}{k} = -\frac{q^2n_0n_1}{ik\epsilon_0} + 3ikTn_1.$$

Multiplying throughout the above equation by $-\dfrac{ik}{mn_1}$ yields the so-called 'Bohm-Gross dispersion relation'

$$\omega^2 = \frac{n_0q^2}{\epsilon_0m} + \frac{3k^2T}{m} = \omega_{pe}^2 + 3k^2v_{t,e}^2 \tag{4.63}$$

where

- $\omega_{pe} = \sqrt{\dfrac{n_eq^2}{\epsilon_0m}}$ is the electron plasma frequency
- $v_{t,e} = \sqrt{\left(\dfrac{T}{m}\right)}$ is the electron thermal velocity.

The thermal motion of the electrons can cause the plasma to propagate. The plasma oscillations can then be called a plasma wave. Given our assumption that $E_1||k$, it can in general be shown that such longitudinal waves must be electrostatic, meaning there's no pertubed magnetic field. As such, plasma waves or Langmuir waves are always electrostatic.

4.3.2 High-frequency electromagnetic waves propagating perpendicular to the magnetic field lines

Having introduced the notion of plasma oscillations, the interaction of high-frequency EM waves propagating perpendicular to an externally applied static magnetic field B_0 are now considered. This implies that the direction of the vector wave-number is perpendicular to the static magnetic field, $\mathbf{k} \perp \mathbf{B}$. By high-frequency it is implied that the frequency of oscillation is so high that the ions essentially remain unperturbed owing to their large inertia.

Working from the assumption that $\mathbf{k} \perp \mathbf{B}$, a further subdivision of this specific wave type can be made, namely 'ordinary waves' and 'extraordinary waves'. Ordinary waves or O-waves, arise where the high-frequency wave propagation is perpendicular to the magnetic field, $\mathbf{k} \perp \mathbf{B}$, and the high-frequency wave's electric field component, $\mathbf{E}$, is parallel to the magnetic field, $\mathbf{E} \parallel \mathbf{B}$.

Lets now determine the dispersion relation for O-waves. To do this, one starts off with Maxwell's equations, (3.70) and (3.71).

$$\nabla \times \mathbf{E}_1 = -\frac{\partial \mathbf{B}_1}{\partial t}$$

$$\nabla \times \mathbf{B}_1 = \mu_0 \mathbf{j} + \frac{1}{c^2}\frac{\partial \mathbf{E}_1}{\partial t}$$

Taking the time derivative of (3.70) results in:

$$\nabla \times \frac{\partial \mathbf{B}_1}{\partial t} = \mu_0 \frac{\partial \mathbf{j}}{\partial t} + \frac{1}{c^2}\frac{\partial^2 \mathbf{E}_1}{\partial t^2}.$$

Taking the curl of (3.71) and using the vector identities results in:

$$\nabla \times (\nabla \times \mathbf{E}_1) = \nabla (\nabla \cdot \mathbf{E}_1) - \nabla^2 \mathbf{E}_1 = -\nabla \times \frac{\partial \mathbf{B}_1}{\partial t}. \tag{4.64}$$

Substituting the time derivative of (3.70) into (4.64) and using our initial assumption of sinusoidal planes waves results in:

$$k^2\mathbf{E}_1 - \mathbf{k}\left(\mathbf{k}\cdot\mathbf{E}_1\right) = \frac{\omega^2}{c^2}\left[\mathbf{E}_1 + \frac{i\mathbf{j}_1}{\epsilon_0\omega}\right]. \tag{4.65}$$

From (4.65) one can derive an expression for the dispersion relation for high-frequency electromagnetic waves with $\mathbf{E}_1||\mathbf{B}_0$. This is given by:

$$\omega^2 = c^2k^2 + \omega_p^2. \tag{4.66}$$

Extraordinary waves or X-waves arise where the high-frequency wave propagation is again perpendicular to the magnetic field, $\mathbf{k} \perp \mathbf{B}$. However in contrast to O-waves, X-waves have a longitudinal component, $\mathbf{k} \perp \mathbf{E}_1$, and a transverse component, $\mathbf{k}||\mathbf{E}_1$, depending on the frequency of the propagating wave. If one now choose $\mathbf{B}_0$ to be z-directed and $\mathbf{k}$ to be x-directed, then $\mathbf{E}_1$ must have components in the x and y directions.

In the derivation that follows, the so-called 'cold plasma' approximation is used. This implies that the scalar electron pressure is neglected and it is assumed $T_e = T_i = 0$. Linearising the equation of motion of the electron fluid, one obtains:

$$-i\omega m u_{x1} = -e\left(E_{x1} + u_{y1}B_0\right) \tag{4.67}$$

$$-i\omega m u_{y1} = -e\left(E_{y1} + u_{x1}B_0\right). \tag{4.68}$$

These equations can be solved using Cramer's Rule for solving a system of linear equations with two unknowns, u_{x1}, u_{y1}.

$$\frac{e\mathbf{E}_{x1}}{m} = i\omega u_{x1} - \omega_c u_{y1} \tag{4.69}$$

$$\frac{e\mathbf{E}_{y1}}{m} = \omega_c u_{x1} + i\omega u_{y1} \tag{4.70}$$

The determinant is $\omega_c^2 - \omega^2$ and the solutions are:

$$u_{x1} = \frac{\left(\frac{e}{m}\right)\left(i\omega E_{xi} + \omega_c E_{y1}\right)}{\left(\omega_c^2 - \omega^2\right)} \tag{4.71}$$

$$u_{y1} = \frac{\left(\frac{e}{m}\right)\left(i\omega E_{yi} + \omega_c E_{x1}\right)}{\left(\omega_c^2 - \omega^2\right)} \tag{4.72}$$

The electron fluid equations, (4.71) and (4.72) obtained above, is then substituted into the wave equation given by (4.65). Since one is dealing with high-frequency waves, the ions are essentially stationary and the current density is generated by the electron flow only, therefore:

$$\mathbf{j}_1 = -n_0 e \mathbf{u}_1. \tag{4.73}$$

The vector $\mathbf{E}_1$ is then separated into its two components, E_{x1} and E_{y1}. The component in the z direction correspond to the O-waves considered earlier. From the x component of the right-hand side of (4.65) one obtains:

$$E_{x1} = \frac{i\left(\dfrac{n_0 e^2}{\epsilon_0 m}\right)\left(i\omega E_{x1} + \omega_c E_{y1}\right)}{\omega\left(\omega_c^2 - \omega^2\right)} \tag{4.74}$$

and from the y component, multiplying throughout by $\dfrac{c^2}{\omega^2}$, one obtains

$$\left(\frac{1 - c^2k^2}{\omega^2}\right) E_{y1} = \frac{i\left(\dfrac{n_0 e^2}{\epsilon_0 m}\right)\left(i\omega E_{y1} - \omega_c E_{x1}\right)}{\omega\left(\omega_c^2 - \omega^2\right)}. \tag{4.75}$$

Finally one multiplies throughout by $(\omega_c^2 - \omega^2)$ and rearrange the equations to obtain

$$\left(\omega_c^2 - \omega^2 + \omega_p^2\right) E_{x1} - i\left(\frac{\omega_p^2 \omega_c}{\omega}\right) E_{y1} = 0 \tag{4.76}$$

$$i\left(\frac{\omega_p^2 \omega_c}{\omega}\right) E_{x1} + \left[\left(1 - \frac{c^2k^2}{\omega^2}\right)\left(\omega_c^2 - \omega^2\right) + \omega_p^2\right] E_{y1} = 0. \tag{4.77}$$

As seen before, these are two simultaneous equations for E_{x1} and E_{y1}. By allowing the determinant of these equations to vanish, one obtains the dispersion relation for the extraordinary waves.

$$\left(\omega_c^2 - \omega^2 - \omega_p^2\right)\left[\left(1 - \frac{c^2k^2}{\omega^2}\right)\left(\omega_c^2 - \omega^2\right) + \omega_p^2\right] - \left(\frac{\omega_p^2 \omega_c}{\omega}\right)^2 = 0 \tag{4.78}$$

One can then define the so-called 'upper-hybrid' frequency as:

$$\omega_h^2 \equiv \omega_p^2 + \omega_c^2. \tag{4.79}$$

Writing the dispersion relation in terms of the upper hybrid frequency results in:

$$\left(1 - \frac{c^2k^2}{\omega^2}\right)\left(\omega_c^2 - \omega^2\right) + \omega_p^2 = \frac{\left(\dfrac{\omega_p^2 \omega_c}{\omega}\right)^2}{\left(\omega_h^2 - \omega^2\right)}. \tag{4.80}$$

By applying some algebraic manipulations, the result above can be simplified to:

$$\frac{c^2k^2}{\omega^2} = \frac{c^2}{v_p^2} = 1 - \frac{\omega_p^2\left(\omega^2 - \omega_p^2\right)}{\omega^2\left(\omega^2 - \omega_h^2\right)} \tag{4.81}$$

where

- $v_p \equiv \dfrac{\omega}{k} = c\left(1 + \dfrac{\omega_p^2}{c^2k^2}\right)^{\frac{1}{2}}$ is the phase velocity.

As a wave propagates through a region in which ω_c and ω_p change, it may encounter *cutoffs* and *resonances*. A wave is generally reflected at a cutoff and absorbed at a resonance.

The cutoffs of an extraordinary wave may be determined by allowing $k \to 0$ in (4.81). This yields the result

$$\omega\left(\omega^2 - \omega_c^2 - \omega_p^2\right) = \omega_p^2\left(\omega^2 - \omega_p^2\right). \tag{4.82}$$

To get an expression for ω, both sides of (4.82) is divided by $\omega\left(\omega^2 - \omega_p^2\right)$. Performing some algebraic manipulations and taking the square root then yields:

$$\omega^2 \pm \omega\omega_c - \omega_p^2 = 0. \tag{4.83}$$

From this result one can obtain four solutions for the cutoff frequency of an extraordinary wave

$$\omega = \frac{1}{2}\left[\pm\omega_c \pm \left(\omega_c^2 + 4\omega_p^2\right)^{\frac{1}{2}}\right]. \tag{4.84}$$

However, by definition, frequency is a positive quantity and as such, one can discard negative ω. This leads to two different cutoff frequencies, namely the right-hand cutoff frequency, ω_R, and the left-hand cutoff frequency, ω_L.

$$\omega_R = \frac{1}{2}\left[\omega_c + \left(\omega_c^2 + 4\omega_p^2\right)^{\frac{1}{2}}\right] \tag{4.85}$$

$$\omega_L = \frac{1}{2}\left[-\omega_c + \left(\omega_c^2 + 4\omega_p^2\right)^{\frac{1}{2}}\right] \tag{4.86}$$

4.3.3 High-frequency electromagnetic waves propagating parallel to the magnetic field lines

As in the case above, $\mathbf{B}_0$ is again assumed to be z-directed and as one is considering high-frequency wave propagation parallel to the magnetic field

lines, $\mathbf{k}$ must also be z-directed. $\mathbf{E}_1$ is allowed to have both transverse components, E_x and E_y. By defining $\mathbf{B}_0$ as being z-directed, the electron fluid velocities defined by (4.71) and (4.72) are still valid. Next one substitutes the expression for the current density, (4.73), into the wave equation, (4.65) and arrange the result of the x- and y- components of $\mathbf{E}_1$ in the appropriate form for solution using Cramer's Rule.

$$i\left(\frac{\omega_p^2\omega_c}{\omega}\right)E_{x1}+\left[\left(1-\frac{c^2k^2}{\omega^2}\right)\left(\omega_c^2-\omega^2\right)+\omega_p^2\right]E_{y1}=0$$

$$\left[\left(1-\frac{c^2k^2}{\omega^2}\right)\left(\omega_c^2-\omega^2\right)+\omega_p^2\right]E_{x1}-i\left(\frac{\omega_p^2\omega_c}{\omega}\right)E_{y1}=0$$

As was done in the case of the extraordinary waves, the determinant of coefficients is set equal to zero

$$\left(\frac{\omega_p^2\omega_c}{\omega}\right)^2-\left[\left(1-\frac{c^2k^2}{\omega^2}\right)\left(\omega_c^2-\omega^2\right)+\omega_p^2\right]^2=0$$

This quadratic equation has two solutions given by:

$$\left(\frac{\omega_p^2\omega_c}{\omega}\right)=\pm\left[\left(1-\frac{c^2k^2}{\omega^2}\right)\left(\omega_c^2-\omega^2\right)+\omega_p^2\right] \tag{4.87}$$

Lets now define the index of refraction, $\tilde{n}\equiv\dfrac{c^2k^2}{\omega^2}=\dfrac{c^2}{v_p^2}$. Having done that, one multiplies throughout (4.87) by ±1 and divide the result by $(\omega_c^2-\omega^2)$ to obtain:

$$\tilde{n}=1-\frac{\omega_p^2}{\omega\left(\omega+\omega_c\right)}\qquad\text{(L wave)} \tag{4.88}$$

$$\tilde{n}=1-\frac{\omega_p^2}{\omega\left(\omega-\omega_c\right)}\qquad\text{(R wave)} \tag{4.89}$$

Both these waves are so-called 'circularly polarised' waves, with the designations R and L meaning, right-hand circularly polarised and left-hand circularly polarised respectively. This implies that the R-wave is a wave rotating according to the right-hand rule. If the thumb of the right hand points in the direction of the magnetic field, then the curled fingers indicates the direction of rotation of the electric field vector. The left-hand rule applies to L-waves.

Lets now consider the cutoffs and resonances of the right-hand and left-hand circularly polarised waves. By allowing $k \rightarrow 0$ in (4.88) and (4.89) one obtains a quadratic equation for the cutoff frequencies. As before only cases where $\omega > 0$ are considered. One then obtains the same equations as was found for the cutoffs of the X-waves. The R-wave has the higher cutoff frequency, ω_R, and the L-waves has the lower cutoff frequency, ω_L. By setting k=0 for the R-waves, one obtains a resonance condition at $\omega = \omega_c$, where at resonance $\tilde{n} = \dfrac{ck}{\omega} \rightarrow 0$. In this resonance condition, the direction of rotation of the plane of polarisation is the same as the direction of gyration of the electrons. The wave therefore loses its energy in continuously accelerating the electrons.

Chapter 5

Experimental measurements on the Berlin 14.5 GHz ECRIS

5.1 Summary of previous bremsstrahlung investigations performed by other groups

During the interaction of a gas cloud with externally launched high-frequency electromagnetic waves, an ECR plasma is created. These ECR plasmas have been extensively investigated in the past as a possible alternative to the Tokamak fusion device [30]. A characteristic feature of these ECR plasmas are the existence of very energetic electrons. Electron energies of up to several MeV have been reported [31]. These energetic electrons can be studied by measuring the bremsstrahlung spectra emitted from the plasma.

Following these developments, bremsstrahlung measurements have been performed on ECR heated plasmas. These measurements has its roots in the 1960s with some of the first measurements being performed at Massachusetts Institute of Technology [32]. Since these first bremsstrahlung measurements, various investigations have been undertaken by a number of different institutes around the globe. The following discussion is by no means an exhaustive summary of all bremsstrahlung measurements performed over the years, but merely highlights the research performed by a number of these institutes.

At the Institute of Modern Physics in Lanzhou, China bremsstrahlung measurements have been performed to estimate the heat load to the cryostat on the Superconducting ECR ion source with Advanced design in Lanzhou, SECRAL. From these measurements possible solutions to reduce the heat load to the cryostat was proposed [33]. Measurements of bremsstrahlung were

also performed on the Lanzhou ECR ion source no. 2 Modified, LECR2M, operated at 14.5 GHz [34]. During these measurements a relative index of the average energy of the hot electron population was defined. This relative index or so-called spectral temperature was then investigated as a function of various ECRIS parameters. Similar axial bremsstrahlung measurements were also performed on the Lanzhou ECR ion source no. 3, LECR3 [35]. This source is fed with dual heating frequencies of 10 GHz and 14 GHz. During this investigation changes were made to the collimation system used during earlier measurements. This was performed largely to negate the effects of thick target bremsstrahlung and secondary scattered radiation on the measured bremsstrahlung spectra.

At the Department of Physics, University of Jyväskylä, JYFL, radial bremsstrahlung radiation were measured to study the effects of frequency tuning on the JYFL 14 GHz ECRIS [36]. This source is one of only a few ECR ion sources with a radial port to allow radial bremsstrahlung investigations. During this investigation the heating frequency of 14.085 GHz was varied within a band of 85 MHz. From these measurements it was concluded that minor changes in the heating frequency causes the electric field at the ECR zone to change drastically. This brought about fluctuations in the bremsstrahlung emission. In addition to this, a comprehensive set of bremsstrahlung measurements have also been performed on both the JYFL 6.4 GHz ECRIS and the JYFL 14 GHz ECRIS [37],[38]. This was done to gain a better understanding of the parameters affecting the time-evolution of electron energy. During one of these investigations, the bremsstrahlung data were analysed with 2 ms time intervals. This investigation yielded much information about the electron heating process inside an ECR ion source at unprecedented time resolution. Others investigations performed by this group was focused on probing the plasma breakdown process as well as studying phenomena that occurs at the beginning of the application of the microwave pulse and at the end of the application of the microwave pulse. Measurements by this group also linked the generation of high-energy electrons, typically energies exceeding 30 keV, with ion-beam production times.

Bremsstrahlung investigations were also performed by the Lawrence Berkeley National Laboratory, LBNL, ECR Ion Source Group in Berkley, California. During one such investigation performed by this group, bremsstrahlung measurements were combined with measurement of the diamagnetic current of the heated electrons [39]. During this investigation, performed on the LBNL 6.4 GHz ECR, the measured bremsstrahlung spectra were used to

determine the total X-ray power produced by the plasma. As was done by the Chinese, this investigation was performed to gain insight into the heat load brought about by the emitted X-rays. During another bremsstrahlung investigation performed by this group, the high energy component of the bremsstrahlung spectra generated by the 28 GHz Versatile ECR for Nuclear Science, VENUS, was studied [40],[41]. This investigation was performed to draw conclusions about the electron heating process and electron confinement in this source. Additionally the aim was to gain an understanding of the heat load absorbed by the cryostat of this source as this is also a superconducting ECR ion source. This group also examined the anisotropy in the X-ray power by simultaneously measuring the emitted bremsstrahlung radiation in the radial and axial directions. These measurements were done on both the 6.4 GHz LBNL ECRIS and the 14.3 GHz LBNL AECR-U [39].

At the National Superconducting Cyclotron Laboratory at Michigan State University, bremsstrahlung measurements were also performed using a fully superconducting 3rd generation ECR ion source [42]. This source called the Superconducting Source for Ions, SuSI, has six solenoid magnets. During one of the investigations performed by this group, the magnetic confinement field were tuned for so-called $\mathbf{B}_{\text{min}}$ and Flat$\mathbf{B}$ operation and the bremsstrahlung spectra measured for each mode of operation. In addition to this, the magnetic gradient at the injection side and extraction side of the resonance zone were independently varied and the bremsstrahlung spectra measured. From this investigation it was concluded that the $\mathbf{B}_{\text{min}}$ mode of operation is accompanied by very high radiation level.

Bremsstrahlung measurements were also performed by the Institut für Experimentalphysik AG II, Ruhr-Universität Bochum. This institute, along with the institute of Geller, is credited for first using electron cyclotron resonance heating to produce high charge state ions [4]. This group has largely been responsible for the design of a collimation system used to measure only bremsstrahlung generated by the plasma itself [6],[43]. During one such bremsstrahlung investigation, this group developed a scheme to extract the energy information from the measured bremsstrahlung spectra [44]. From this investigation they concluded that the energy distribution of the electrons obeyed a power law. They also concluded that the density of electrons with energies higher than 10 keV is very low. Over the years this group has refined its collimator design to measure only the so-called volume bremsstrahlung [43].

5.2 The Berlin 14.5 GHz ECRIS

The Berlin 14.5 GHz ECRIS, also called the ECRIS4, was originally build by GANIL for the Hahn-Meitner Institute, HMI [45], now called the Helmholtz-Zentrum Berlin. This source, shown in figure 5.1, was installed at iThemba LABS and linked up to the transfer beamline supplying charged particle beams to SPC2. The source has an 18 cm in length, water-cooled plasma chamber, with a diameter of 7 cm. To confine the charged particles radially, the plasma chamber is surrounded by permanent magnets made of FeNdB. These permanent magnets are arranged to produce a hexapolar field of strength 1 T at the walls of the plasma chamber. For axial particle confinement, the ECRIS4 has two solenoid coils. Along with the hexapolar field, these axial coils produce a field on the axis of the plasma chamber, that varies between 0.4 T and 1.1 T. The external electromagnetic power is supplied by a 14.5 GHz klystron that can deliver up to 2 kW of microwave power.

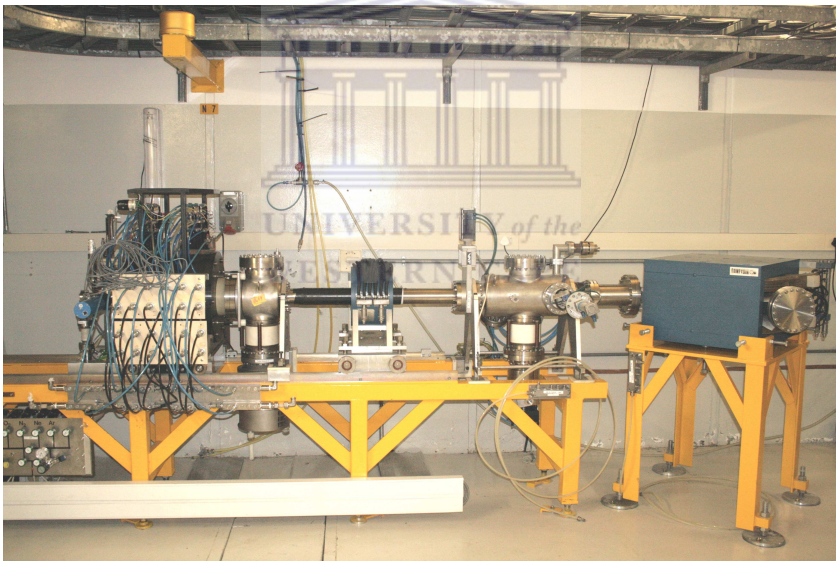

Figure 5.1: The Berlin 14.5 GHz ECRIS and the transfer beamline, consisting of a solenoid, a diagnostic chamber and 90 ° bending magnet.

In Berlin, the source and its beamline was operated at a high voltage of typically 15 kV [45]. At iThemba LABS, only the plasma chamber of the source is on a high-voltage, with the transfer beamline on ground potential. The extraction system of the ECRIS4 has a so-called quasi-Pierce geometry. The plasma electrode has an aperture of diameter 8 mm and its potential

ion	charge state	I [μA]
^{16}O	7+	18
^{40}Ar	14+	2.2
^{129}Xe	26+	5
^{181}Ta	29+	2

Table 5.1: Ion beam currents delivered by the ECRIS4 during the acceptance test of the source in Berlin.

is varied between 2 kV and 20 kV. The extraction electrode is on ground potential and has aperture of 13 mm and the distance between the two metal electrodes is 20 mm.

During the acceptance test of the ECRIS4 in September 1991 in Berlin, the source delivered the ion beam currents as shown in table 5.1 at an emittance less then 80 πmm mrad [45].

5.3 The Grenoble Test Source at iThemba LABS

The Grenoble Test Source at iThemba LABS, GTS2, is a replica of the GTS build by CEA for CERN. Like the ECRIS4, the GTS2, shown in figure 5.2 is also a room temperature ECRIS, meaning its axial magnetic field is generated by copper coils powered by large current supplies. These DC power supplies can deliver as much as 1300 A. Three sets of coils are utilised to produce the axial magnetic field, with the centre coil used for tuning the $\mathbf{B}_{\text{min}}$ field. The axial magnetic field can be varied between 0.5 T and 1.2 T.

The plasma chamber of the GTS2 has a double wall and is manufactured from aluminium [46]. It has an axial length of 30 cm and a diameter of 8 cm. The plasma chamber is surrounded by a permanent magnet hexapole, made of FeNdB, arranged in the Halbach structure and has a radial magnetic field strength of 1.3 T [46].

The resulting magnetic field that can be produced with the GTS2, allows the source to be operated at both 14 and 18 GHz. The source is therefore

Figure 5.2: The Grenoble Test Source at iThemba LABS.

coupled, via watercooled waveguides, to two microwave generators corresponding to the two above-mentioned frequencies. This allows the source to be operated in single or double frequency mode. Additionally, the source is also equipped with two ovens to produce metallic vapours.

The extraction from the GTS2 is performed by means of the so-called accel/decel extraction system. This entails an additional 'suppressor electrode' which shields the positive space charge of the extracted ion beam from the 'compensating electrons' [47]. These electrons are generated when the extracted ion beam ionises the residual gas particles present in the beamline following the extraction system.

The one discerning factor that sets the GTS2 apart from all the previous ECR ion sources at iThemba LABS is the fact that the GTS2 can be operated in either continuous wave, CW, or pulsed mode. This allows investigation of new ECRIS phenomena like the preglow and the afterglow effects [37],[38],[48].

5.4 The measurement setup

5.4.1 Collimation geometry and detection system used for the bremsstrahlung spectra

The high-energy bremsstrahlung emanating from an ECRIS has been measured in previous investigations by means of either Ge, NaI or CdTe detectors [49]. In our facility the former two detector types are available, hence only these detector were investigated for the bremsstrahlung measurements. Since germanium detectors have a much better energy resolution than a NaI detector [50], it was the logical choice for the measurements.

To detect the high-energy bremsstrahlung, it was decided to use the EG&G Ortec, GMX-10200. This high-purity germanium detector, HPGe, has a 55 mm diameter entrance window, through which the radiation enters the detector, and is 56.3 mm in length. The entrance face of the detector is covered with a 50 μm thick Beryllium window. By applying a 1500 V potential across the p-n junction, the detector becomes 'fully depleted'. As the bremsstrahlung enters the detector, it creates electron-hole pairs. A signal is therefore created which is directly proportional to the energy of the incoming bremsstrahlung.

The signal from the HPGe detector is usually very small, typically less than a millivolt, and needs to be preamplified before the signal can be further processed. The signal is fed from the detector to the preamplifiers. To eliminate poor signal-to-noise ratio, which is largely caused by stray electromagnetic fields and cable capacitance, the preamplifiers are placed close to the detector, to minimise the cable length. Two preamplifiers were used, one inside the cryostat of the detector equipped with a Field Effect Transistor, and one placed immediately outside the cryostat. From the output of the second preamplifier, the signal or pulse is fed into the digital electronics module, DGF Pixie-4 [51].

To simplify deconvolution of the bremsstrahlung spectra, if one were to determine the distribution function of the electron population, a collimation system was designed in such a way that the detector is not illuminated by any wall bremsstrahlung [52]. Given that the extraction aperture of the ECRIS4 has a 8 mm diameter, it was decided on a single collimator. The collimator is located 2.86 m after the extraction aperture of the source. The collimator is 4 cm long, with a 2 mm circular aperture in the centre and is made of

lead, with a thin copper inner lining. Since copper has no absorption edges in the energy range of interest, the thin copper lining lowers the probability of characteristic X-rays, produced by photoelectric absorption in the copper, from entering the detector. The only characteristic X-rays observed in the measurements were Tantilium from the source.

Given the size of the extraction aperture of the ECRIS4, our measurements mostly likely include wall bremsstrahlung. This wall bremsstrahlung would be generated by electrons bombarding the extraction electrode of the ECRIS and in the process generating thick-target bremsstrahlung. Since the collimation system does not limit the solid angle visible to the detector to an area smaller than the extraction aperture of the ECRIS, the measurements most likely includes wall bremsstrahlung. This was one of the reasons it was decided not to determine the Electron Energy Distribution Function, EEDF, of the electron population causing the bremsstrahlung. The electron temperature measured with the experimental setup was mainly used as a relative indication of the electron temperature.

The layout of the vault housing the two ECR ion sources, the connecting transfer beamlines and the detector setup, is shown in Figure 2.5. To select ions with the proper $\frac{m}{q}$ ratio, and to bend the charge particle beam into the transfer beamline, a 90 ° bending magnet is used. A perspex window was initially used to terminate the transfer beamline. This allowed the axial bremsstrahlung to penetrate through the perspex window and enter the HPGe detector. Initial measurements of the axial bremsstrahlung, with a silicon drift detector, indicated a possible attenuation of the low-energy bremsstrahlung in the perspex window. To address this problem, the perspex window was replaced with a 50 μm thick Kapton foil.

After removing the perspex window terminating the vacuum chamber of the 90 ° bending magnet, a valve was attached to the CF64 flange of the vacuum chamber. This was done to isolate the experimental setup from the source. A diagnostic chamber was then attached to the valve. This diagnostic chamber had six KF16 ports, of which only three were used. These were used to connect two pressure gauges and another to connect to a forepump. The other unused ports were closed with blank flanges. At the opposite end of the diagnostic chamber, reducers were placed to convert the CF64 flange to a KF16 flange. The Kapton window was vacuum-sealed with clamps to this flange. Using long 8 mm threaded bolts, the collimator system was secured to the CF64 flange of the diagnostic chamber.

5.4.2 Digital Gamma Finder (DGF) Pixie-4

The output from the preamplifier of the HPGe detector was fed via an RG-58 coaxial cable into one channel of the DGF Pixie-4 [51].

Digital spectrometers, like the DGF Pixie-4, is renowned for acquiring detailed pulse shapes, using high-speed analog to digital converters. The acquired pulse shape is then processed using field-programmable gate arrays and digital signal processors. Amongst others, this allows for very precise energy measurement and time stamping of the measured signal from the preamplifier of the HPGe detector.

Given that the GTS2 is to be operated in pulsed mode, it is intended to perform time-resolved measurements on this ECRIS, investigating time-resolved phenomena, like the preglow and the afterglow effects. To perform time measurements with analog multichannel analysers, multichannel scaling needs to be selected. This however limits one to performing measurements on time phenomena with at best twenty millisecond intervals. Given that electron heating occurs on much smaller timescales, it is desirable to measure with finer timescales, typically sub-millisecond timescales. This valuable option is made available to using the DGF Pixie-4. This was one of the deciding factor that drove us to opt for a digital measurement setup as oppose to the traditional analog measurement setup predominantly used by other investigators of plasma bremsstrahlung diagnostics.

After having acquired the data with the Pixie-4 [51], the data is analysed with subroutines written in Root [53].

5.5 The data analysis

5.5.1 Determining the electron energy distribution function

To ionise the injected atoms in an ECRIS, one relies on the interaction between an high-energy electron and a atom. However obtaining information about the energy of an electron in an ECRIS plasma is not a trivial matter. To accomplish this task, one relies on measuring the X-ray bremsstrahlung emanating from the ECRIS plasma. A number of such investigations have been performed in the past as described in the beginning of this chapter.

For our measurements, the initial goal was to only measure the volume bremsstrahlung, as this gives a definite evaluation of the EEDF [6].

Since the emitted bremsstrahlung spectra appeared to have an exponential dependence on the photon energy, it was assumed, that the high-energy electrons resulting in the bremsstrahlung being emitted, has a distribution function similar to a Maxwellian distribution function [6]. From the gradient of the spectra, one can then determine a so-called spectral temperature and use this parameter as a relative indicator of the electron temperature [41].

To obtain a more accurate EEDF one has to correct the measured volume bremsstrahlung spectra for two nonlinear effects, namely the energy dependence of the bremsstrahlung cross-section and the response function of the detector [6]. If one wants to obtain an EEDF from the wall bremsstrahlung or thick target bremsstrahlung [52], one has to correct for an additional nonlinear effect due to the additional scattering of electrons and radiation in the material of the wall of the plasma chamber [6]. The process of correcting for these nonlinear effects is called deconvolution of the bremsstrahlung spectra.

Before proceeding with any measurements, a background spectrum was taken to remove the counts at each energy channel corresponding to the average background count rate. From the background spectrum displayed in figure 5.3, the peaks for ^{22}Na, 511 keV and 1274 keV, and for ^{40}K, 1466 keV, are clearly visible. This spectrum was taken by exposing the HPGe detector to the ambient radiation in the ECR vault for a period of twelve hours.

To obtain the EEDF of the high-energy electrons, $f(E)$, one measures the emitted bremsstrahlung spectra, $I(K)$, from the magnetically confined plasma. This allows one to relate the electron energy E to a photon energy K. However, measurements of the bremsstrahlung spectra are usually performed with a X-ray detector which has a nonlinear response to a continuum of photon energies. The resultant bremsstrahlung spectra, measured with the X-ray detector and acquired with the data acquisition system, is therefore transformed into pulse height spectra, $P_m(K')$ where K' is the pulse height corresponding to the photon energy K.

By assuming that the collimation system implemented results in measurement of only the volume bremsstrahlung, $P(K')$ can be deconvoluted to yield $f(E)$ in a two step process, correcting for the two nonlinear effects

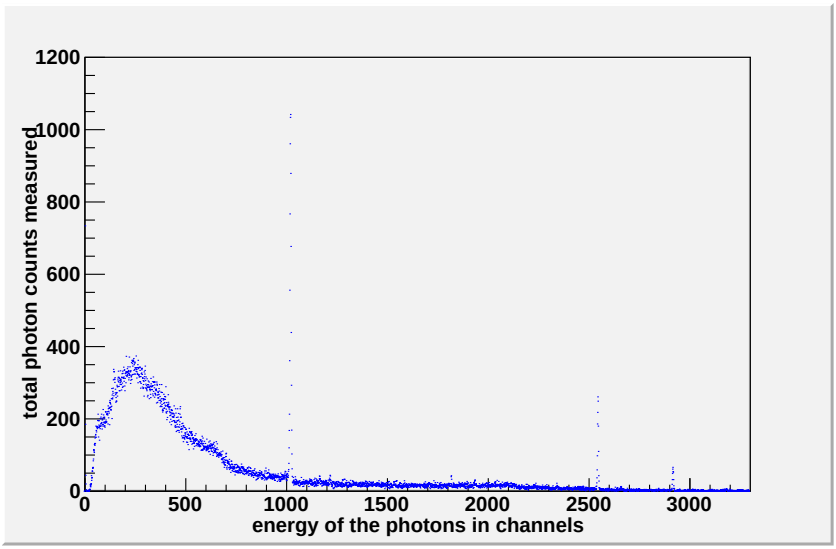

Figure 5.3: Background spectrum measured in the ECR vault with both sources not operational. The vertical axis shows the number of counts measured by the detector and the horizontal axis shows the energy of the detected peaks in channels. The binning of the histograms was chosen to be 500 eV.

mentioned earlier. To obtain an accurate $f(E)$, one first needs to normalise the measured spectra.

$$P(K') = P_m(K') \frac{4\pi\eta}{\Delta\Omega V t_m \Delta K \epsilon} \tag{5.1}$$

where

- $\eta = \dfrac{I}{I_0} = e^{-\mu t}$ is the attenuation the radiation suffered in the kapton vacuum window and in the air, before being detected by the X-ray detector
- $P_m(K')$ is the measured spectra
- $\Delta\Omega$ is the solid angle visible to the X-ray detector
- $V = 0.2$ L is the volume of the plasma
- t_m is the time interval during which the measurement was performed
- $\Delta K = 500$eV is the binning of the histogram
- ϵ is the absolute efficiency of the X-ray detector.

To proceed, the response function of the detector, $F(K', K)$, was determined. The nonlinear response of the detector results from the finite resolution of the detector and the counting of secondary Compton scattered radiation. Neutral radiation, like bremsstrahlung, first needs to be converted to a measurable radiation type before it can be detected. The prime interaction mechanisms for detection of neutral radiation is Compton scattering, photo-electric effect and pair production [50]. Each of these interaction mechanisms has an associated cross section. The measured spectrum reflects the different interactions occurring in the detector volume. Given that maximum bremsstrahlung energy from the ECRIS4 does not exceed 500 keV, pair production can in our case be ignored.

By measuring the response function, $F(K', K_0)$, obtained as a pulse height spectrum, of a number of monoenergetic sources of energy K_0 'equally distributed' over the energy range of interest, one obtains the response function of the continuum of photon energies, $F(K', K)$

$$F(K', K) = \int_0^\infty \delta(K - K_0) F(K', K_0). \tag{5.2}$$

This leads to:

$$P(K') = \int_0^\infty I(K) F(K', K) dK. \tag{5.3}$$

The second step in deconvoluting the measured pulse height spectra is by correcting for the nonlinear bremsstrahlung production. As the electrons present in the magnetically confined plasma have a range of energies, the production of bremsstrahlung will be nonlinear as it is a function of the electron energy. It can be shown that [6]:

$$I(K) = \int_{E=K}^{E_{\max}} G(K, E) f(E) dE \tag{5.4}$$

$$G(K, E) = Kp^2 \sigma(K, E) \tag{5.5}$$

where

- p is the electronic momentum
- $\sigma(K, E)$ is the cross-section for producing radiation of energy K by electrons of energy E.

Defining $H(K', E) = \int_{E=K'}^{E_{\max}} G(K, E) F(K', K)$ and combining equations (5.3) and (5.4) yield:

$$P(K') = \int_{E_{\min}}^{E_{\max}} H(K', E) f(E) dE \tag{5.6}$$

where $E_{\min}$ is the minimum electron energy in $f(E)$.

Using the deconvolution method developed by Bernhardi [44], an approximate solution for $f(E)$ is given by:

$$f(E) \approx -\frac{1}{H(K, E = K)} \frac{dP}{dK}. \tag{5.7}$$

5.5.2 Determining the electron temperature

Working from the earlier assumption that $f(E)$ is a Maxwellian distribution function, one can determine the electron temperature of this electron distribution. This is done by plotting the measured bremsstrahlung intensities on a logarithmic scale and taking the gradient of a line fitted through the spectrum [19]

$$T = -\frac{d \ln J(h\nu)}{d(h\nu)}. \tag{5.8}$$

If all quantities are kept in SI units and the energy is given in keV, the result of the equation above yields the temperature of the electron component in keV. In keeping with the convention chosen in chapter 4, the Boltzmann constant is absorbed into the temperature, hence the temperature is expressed in energy units. This method of determining the electron temperature can also be applied to a bi-Maxwellian distribution [52].

5.5.3 Determining the electron density

In an ECRIS, the extracted ion currents come about as a result of axial losses through the magnetic confinement system. This can be expressed as follows [54]:

$$I_q \approx \frac{n_q q e V}{\tau_q}. \tag{5.9}$$

Additionally, one can also define the ion temperature as follows [55]:

$$T_i = \left(\frac{dT_i}{dt}\right) \left[\frac{\sum_{i=1}^{z} q_i n_i}{\sum_{i=1}^{z} \left(q_i \frac{n_i}{\tau_i}\right)}\right] \tag{5.10}$$

with

$$\frac{dT_i}{dt} = \frac{4\sqrt{2\pi}n_e Z^2 r_e^2 m^2 \sqrt{mc}c^4}{AM\sqrt{T_e}} L_{ei} \tag{5.11}$$

where

- Z is the charge of the nucleus
- r_e is the classical radius of an electron
- m_e is the rest mass of an electron
- c is the speed of light
- $L_{ei} \cong 14$ is the so-called Coulomb logarithm
- A is the atomic mass number
- M is the rest mass of a proton
- τ_i is the ion confinement time.

If one now solves for $\left(\frac{n_q q_i}{\tau_q}\right)$ from (5.9) and substitute this result into (5.10) and assume that the plasma is neutral, one arrives at the following expression for the electron density:

$$n_e = \sqrt{\frac{T_i \sum_{i=1}^{z} q_i \left(\frac{n_i}{\tau_i}\right)}{K}} \tag{5.12}$$

where $K = \frac{4\sqrt{2\pi}Z^2 r_e^2 m^2 \sqrt{mc}c^4 L_{ei}}{AM\sqrt{T_e}}$.

5.6 Measurements and discussion of the experimental results

5.6.1 Investigating the influence of microwave power on electron heating and electron density

Figure 5.4 shows the typical steady-state, axial bremsstrahlung spectra measured for 50 W of incident microwave power from a helium plasma. On this measured spectrum, the horizontal axis shows the photon energy in channels and the vertical axis shows the number of counts recorded by the high-purity germanium detector. In the case of the measurements reported on here, the binning was chosen to be 500 eV per channel.

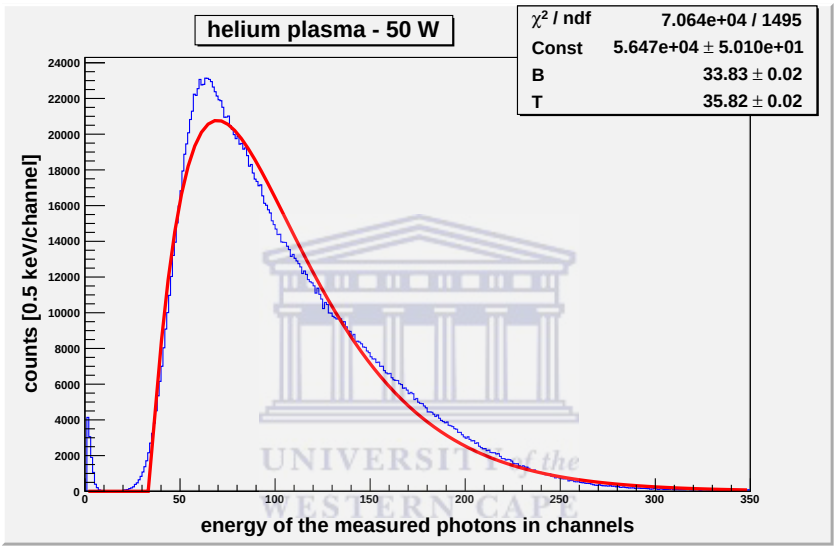

Figure 5.4: The blue curve shows the corrected measured spectra and the red curve is the fitted Maxwellian distribution. The measured spectrum is for 50 W incident microwave power on a helium plasma. The injection coil was set to 645.2 A, the extraction coil was set to 661.4 A and the pressure in the injection side of the ECRIS4 was 1.09×10^{-6}mbar. The binning was chosen to be 500 eV.

Using a subroutine written in Root [53], the measured bremsstrahlung spectra was corrected for background radiation in the ECR vault, as well as for the nonlinear response of the detector. Following this correction, the measured spectra was fitted with a Maxwellian distribution:

$$f(E) = (\text{Const})\,\frac{(E-B)}{T}\mathrm{e}^{-\frac{(E-B)}{T}}$$

where E is the measured photon energy and T is the spectral temperature of the electron population.

It should be mentioned that the measured spectrum under-represents very low energy photons, typically below 10 keV. This is as a result of absorption in the Kapton window and the layer of air between the detector and point of origin of the radiation. This effect was not corrected for in the data. It can also be mentioned that the Compton scattering corrections brought about a shift of low energy photons to higher energies.

Shown in the box, on the upper right hand corner of the measured spectrum, is the calculated values of the fitted parameters of the Maxwellian distribution. The so-called reduced chi-squared statistic, $\frac{\chi^2}{\text{ndf}}$, indicates the 'goodness of the fit' to the Maxwellian distribution. It is generally accepted that values for this statistic in excess of unity implies that the fitted model poorly represents the data. It therefore goes without saying that this measured spectrum is poorly represented by a Maxwellian distribution. This fact does not come as a surprise, as it has already been shown that the electron distribution function of an ECR plasma is not a Maxwellian distribution [4]. However for simplicity, it shall be assumed that the measured spectra can indeed be represented by a Maxwellian distribution, as has been done by various other investigators of these phenomena [34]. It was therefore chosen to describe the ECR plasma as three separate Maxwellian distributions [56]. For the sake of this study these will be referred to as the cold, warm and hot electron populations [56].

As the cold electron population generates bremsstrahlung radiation below the detection threshold of our detector, these are not present in our measured spectra. The detection threshold of our detector is estimated to be around 15 keV. The hot electron population on the other hand has electron energies that makes it inefficient for the production of high-charge states. This can easily be seen from the Lotz formula described in Chapter 4. This electron population is however essential to stabilise the plasma. Our measurements

are therefore only concerned with the warm electron population and the spectral temperature measured is a relative indication of the temperature of this electron population.

By measuring the spectral temperature, it was aimed to gain insight into the process of electron heating as a function of incident microwave power. Electron cyclotron resonance heating is a very effective method to selectively heat the electrons in an ECR plasma using externally launched high-frequency microwaves. However, to explain why this method of electron heating is so effective, is an extremely daunting task. For exactly this reason, it was chosen to explain the measured results of the measurements using stochastic heating with formulae derived from single-particle orbit theories. This approach will shortly be justified.

As discussed in Chapter 3, the electron performs very complex motions around the flux lines of the externally imposed magnetic confinement system produced with a solenoidal field and a hexapolar field. From (4.38) and (4.39), the radial and axial magnetic field components of the solenoidal field can be determined if the axial magnetic field, B_z, on the source axis is measured.

$$B_z = B_z(z) - \frac{r^2}{4}\frac{d^2 B_z}{dz^2} \tag{5.13}$$

$$B_r = -\frac{r}{2}\frac{dB_z}{dz} \tag{5.14}$$

This was performed, as an example, for the JYFL 14 GHz ECRIS, yielding the result [57]:

$$B_z = 91.837z^2 + 0.4 - 183.674\left(\frac{r}{2}\right)^2$$

$$B_r = -183.674z + 0.4\left(\frac{r}{2}\right).$$

Similarly, the radial and azimuthal components of the hexapolar field can be determined from (4.51) and (4.52).

The expressions (5.13), (5.14), (4.51) and (4.52) give the different magnetic field components as a result of the solenoidal and hexapolar fields. This constitutes the static magnetic field of the ECRIS. As discussed in Chapter 3, the motion of the individual charged particles also induce a magnetic field which for the purpose of this discussion should be called the variable magnetic field. The vector sum of this variable magnetic field and the externally

imposed static magnetic field, is what the charged particle experience during its very complicated trajectory around the flux lines.

If one now launches high-frequency microwaves from an external RF generator, the electron motion can be described by the familiar Lorentz equation introduced in Chapter 3. These types of equations can be solved using sophisticated heating codes [57]. This was however not the aim of our investigation. Our investigation was more concerned with observing trends of electron heating as a function of various ECRIS parameters.

From Canobbio's theory [58], for a single electron, passing through a resonance zone located in a magnetic field gradient, one finds that the perpendicular velocity of the electron, $\mathbf{v}_\perp$, is proportional to the high-frequency microwave electric field.

$$\mathbf{v}_\perp \propto \mathbf{E}^{\frac{6}{5}}\delta^{-\frac{4}{5}} \qquad \text{where} \qquad \delta = \frac{1}{|B_0|}\left(\frac{d|B_0|}{dz}\right)\frac{c}{\omega}$$

Additionally, the perpendicular velocity is also proportional to the incident microwave power, implying that more incident microwave power should yield higher electron temperatures.

$$\mathbf{v}_\perp \propto \mathbf{P}^{\frac{3}{5}}\delta^{-\frac{4}{5}} \qquad \text{where} \qquad \mathbf{P} \text{ is the microwave power}$$

The electric field component of the high-frequency microwave can be expressed as follows:

$$\mathbf{E} = E_0 \mathrm{e}^{i(kz-\omega t)} = E_0 \mathrm{e}^{-k_i z}\mathrm{e}^{ik_r z}\mathrm{e}^{i\omega t}.$$

Accepting the general idea that ECRH is caused largely by R-waves and recalling the dispersion relation for these waves, as derived in Chapter 4.

$$\tilde{n} = \frac{k^2c^2}{\omega^2} = 1 - \frac{\omega_p^2}{\omega\left(\omega - \omega_c\right)}$$

Solving for the wave number, k, from this dispersion relation and allowing it to tend to zero, one finds the resonance condition at $\omega = \omega_c$. Because this equation was derived from cold plasma theory, the dispersion relation shows that k goes to infinity at the resonance condition. In reality, one finds damping of the incident high-frequency microwave.

From this one can conclude that as the high-frequency microwaves are launched from the higher magnetic field side to the lower magnetic field side, it is transmitted through the plasma and are absorbed at the resonance region of the plasma. The transfer of power from the high-frequency microwave to the electron depends largely on the phase difference between the high-frequency wave and the orbiting electron. Stochastic heating averages over many electron crossings of the resonance zone. In this way it assumes a random phase difference between the electron and the wave. Absorption occurs when $k_i > 0$ as the microwave is most likely attenuated according to $\mathbf{E} = E_0 \mathrm{e}^{-k_i z}$.

From figure 5.5 it can be observed that the spectral temperature increases linearly as the incident microwave power is increased. By increasing the microwave power from 50 W to 300 W, the spectral temperature for the helium plasma increased by 14.0%, from 17.9 keV to 20.4 keV.

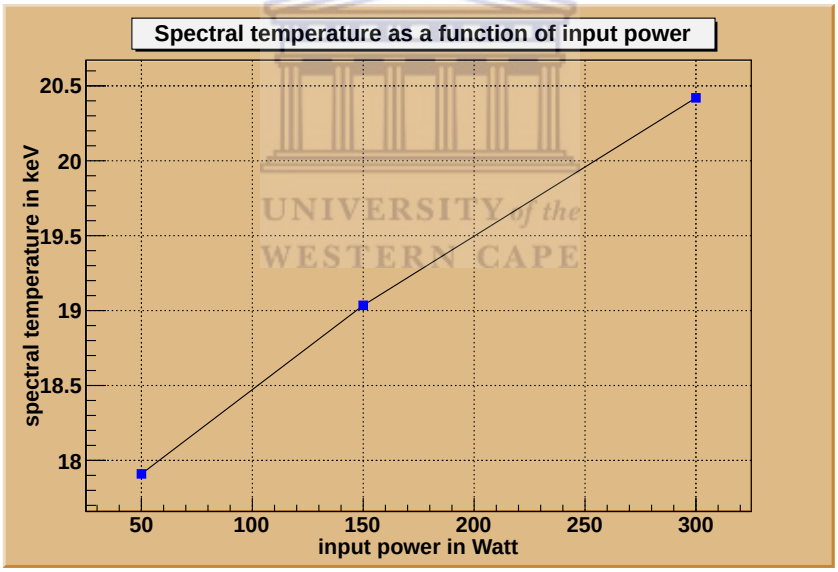

Figure 5.5: Spectral temperature measured as a function of incident microwave power for a helium plasma. The injection coil was set to 645.2 A, the extraction coil was set to 661.4 A and the pressure in the injection side of the ECRIS4 was 1.09×10^{-6}mbar.

These measurements were also repeated for an argon plasma and a typical result displayed in figure 5.6.

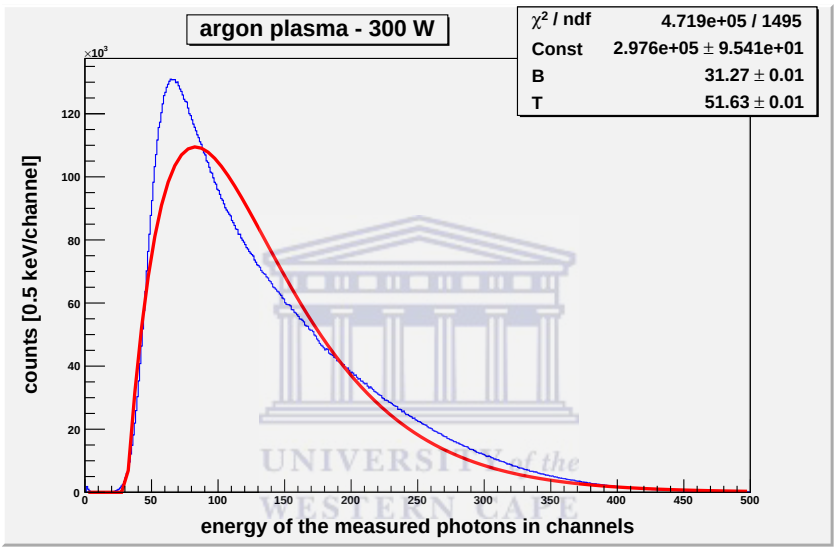

Figure 5.6: The blue curve shows the corrected measured spectra and the red curve is the fitted Maxwellian distribution. The measured spectrum is for 300 W incident microwave power on a argon plasma. The injection coil was set to 804 A, the extraction coil was set to 754 A and the pressure in the injection side of the ECRIS4 was 2×10^{-6}mbar. The binning was chosen to be 500 eV.

Figure 5.7 shows the variation of the spectral temperature with incident microwave power for the argon plasma. In this case, the microwave power was increased in intervals of 50 W. From figure 5.7 it can be seen that the spectral temperature initially increases rapidly. By increasing the microwave power from 50 W to 100 W, the spectral temperature increases by 2.4%. By further increasing the microwave power from 100 W to 150 W, the spectral temperature increases by only 1.3%. Increasing the microwave power even further from 250 W to 300 W, the spectral temperature increases by only 1.2%. This result seems to suggest that the increase of spectral temperature with incident microwave power will saturate after a finite increase of power. It is interesting to note that by increasing the incident microwave power from 50 W to 300 W, the increase in spectral temperature was 7.9% for the argon plasma. A possible explanantion for this substantial difference in spectral temperature increase versus incident microwave power between the helium and argon plasma will be given later.

Whilst the results displayed graphically in figures 5.5 and 5.7 are in agreement with the theory of Canobbio [58], it should be pointed out that the bremsstrahlung measured in our experimental setup is as a result of the axial electron acceleration. Due to cooling issues with the waveguide launching power into the ECRIS, the incident microwave power could not be increased beyond 300 W such that the saturation effect observed in various other similar experiments could be witnessed [39].

In addition to the spectral temperature measured, the electron density was also calculated as a function of incident microwave power during this investigation. Figure 5.8 shows the variation of the electron density with incident microwave power for an argon plasma. From this figure it is noted that by increasing the microwave power from 50 W to 100 W, the electron density rapidly increases by 13.4%, from $6.7\times10^{10}\text{cm}^{-3}$ to $7.6\times10^{10}\text{cm}^{-3}$. By further increasing the microwave power from 100 W to 300 W, the increase in electron density is only 8.8%, from $7.6\times10^{10}\text{cm}^{-3}$ to $8.2\times10^{10}\text{cm}^{-3}$. This could account for the very rapid increase in spectral temperature from 50 W to 100 W as seen earlier. At 50 W, the electron density is still relatively low, which means that the mean free path for the electrons is still relatively long. The electrons therefore less frequently undergo collisions. At 100 W, the electron density has increased significantly, implying more frequent electron collisions and hence a smaller increase in spectral temperature from this microwave power onwards. This is exactly what was observed in figure 5.7.

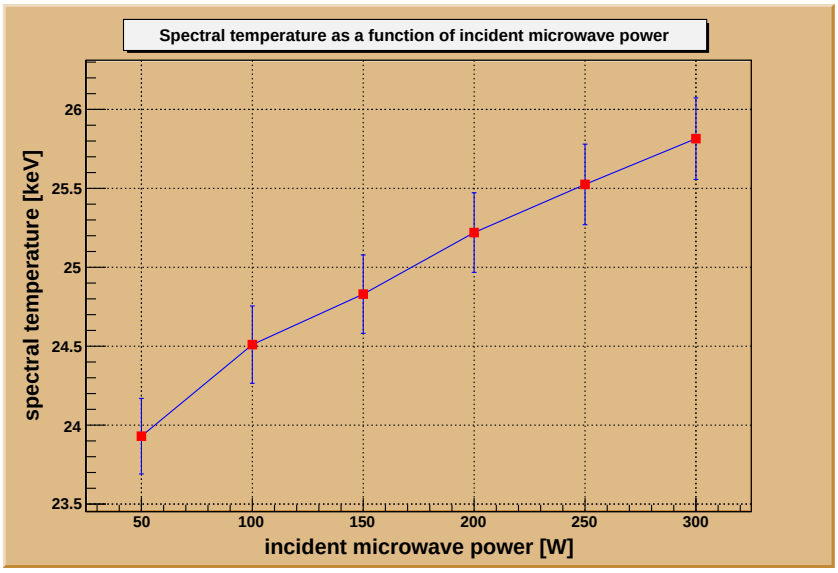

Figure 5.7: Spectral temperature measured as a function of incident microwave power for an argon plasma. The injection coil was set to 804 A, the extraction coil was set to 754 A and the pressure in the injection side of the ECRIS4 was 2×10^{-6}mbar.

It is also believed that this is the reason for the substantial difference in spectral temperature increase with incident microwave power between the helium and argon plasmas. Earlier it was noted that by increasing the microwave power from 50 W to 300 W, the increase in spectral temperature measured was 14.0% for the helium plasma. When this same measurement was repeated for the argon plasma, the increase in spectral temperature measured from 50 W to 300 W was only 7.9%. It is thought that this phenomenon is directly related to the electron density, as the helium plasma has a lower electron density as opposed to the argon plasma.

Following Hitz, one can write a 'rough power balance of an ECRIS in steady state' [56]:

$$\frac{P_{\mathrm{rf}}}{V} \approx \frac{n_e T_e}{\tau_e} \tag{5.15}$$

where P_{rf} is the absorbed microwave power and V is the plasma volume. This equation seems to suggest that the electron temperature and electron density should increase as the absorbed microwave power increases. This therefore suggests that either the absorbed power saturates or an effect takes place that limits the growth of electron density and electron temperature.

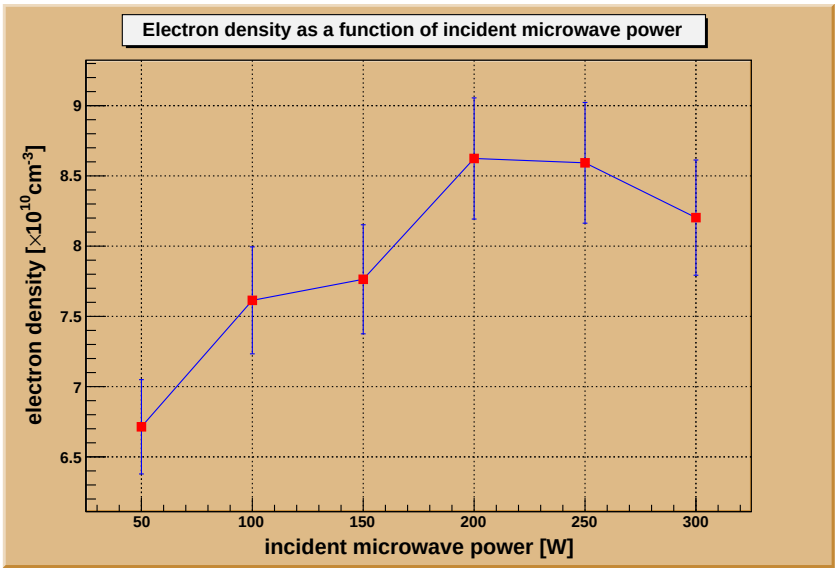

Figure 5.8: Electron densities as a function of incident microwave power, calculated from the extracted ion beam currents for an argon plasma. The injection coil was set to 804 A, the extraction coil was set to 754 A and the pressure in the injection side of the ECRIS4 was 2×10^{-6}mbar.

One such effect that is said to limit the growth of electron temperature and electron density is the rf-induced pitch-angle scattering [59]. This effect, which results in a change of the pitch-angle of the electron, causes the diffusion coefficient to increase. This leads to a loss of heated electrons and limits the density and temperature growth of the electrons.

From the spectral temperature measurement, the electron density was calculated. This allowed us to determine the electron plasma frequency. Given that the mass of an electron is so much smaller than that of an ion, $\omega_p \approx \omega_{\mathrm{pe}}$. From this result it can be concluded that $\left[\frac{\omega_p^2}{\omega_{\mathrm{RF}}^2}\right] \approx 3.832 \times 10^{-9} \ll 1$ over our limited range of measurements. In this so-called underdense plasma limitation, one can make the assumption that the majority of the plasma electrons behave like single orbiting electrons [4]. This justifies our treatment of electron heating from single-particle orbit theories.

5.6.2 Investigating the extracted beam intensities of the different charge states as a function of microwave power

Figure 5.9 presents the extracted ion beam current as measured on faraday cup 3Q in the transfer beamline. The position of this faraday cup in the beamline is shown in figure 2.6. Before proceeding with these measurements, the source was optimised for Ar^{6+}. The source parameters were then kept constant as shown in table 5.2 below and only the incident microwave power was varied.

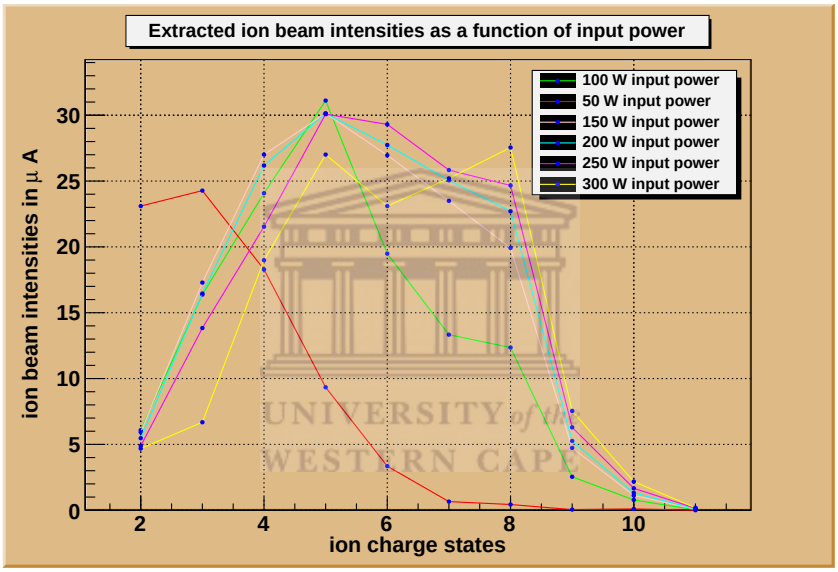

Figure 5.9: Extracted ion beam intensities as a function of incident microwave power for an argon plasma. The injection coil was set to 804 A, the extraction coil was set to 754 A and the pressure in the injection side of the ECRIS4 was 2×10^{-6}mbar.

From the result displayed in figure 5.9 one can immediately deduce that the production of lower charge states becomes very efficient with lower microwave powers. Conversely to produce higher charge states requires more input power. From figure 5.7 it was concluded that the spectral temperature increases with increasing microwave power, up to a saturation point. By increasing the spectral temperature, one increases the lifetime of the electrons. Additionally, the increase in spectral temperature also causes the electron

extraction potential	10 kV
extraction current	2.5 mA
pressure in the injection side of the ECRIS4	2×10^{-6} mbar
pressure in the extraction side of the ECRIS4	6×10^{-7} mbar
injection coil current	804 A
extraction coil current	754 A
incident microwave power	50 W to 300 W

Table 5.2: ECRIS4 settings with the source optimised for Ar^{6+} and the incident microwave power varied between 50 W and 300 W.

density to increase. This in turn causes the ion confinement time to increase. From the Lotz equation [20], it can be shown that the maximum single ionisation cross section increases with increasing electron temperature. However once ionised, the highly-charged particle undergoes charge-exchange, which appears to be independent of electron temperatures [55].

All these factors ultimately play a role in the measured charge state distribution. This problem was investigated by Shirkov *et al* [21]. From their research, they set up a number of equations which allowed them to calculate the mean charge state distribution in an ECRIS. Using their model, they investigated the charge state distribution for argon and krypton ions. From these measurements, they concluded that the ion charge state distribution is virtually independent of electron density. Additionally they also concluded that the dependence of ionisation cross section on electron temperature is so severe, that the charge state distribution tends towards higher charge states, with increasing electron temperature. This result is in complete agreement with our measurements shown in figure 5.9.

5.6.3 Investigating the influence of the neutral pressure on electron temperature and electron density

During this investigation, the source parameters were again kept constant, with only the pressure being varied. Table 5.3 below lists the main source settings during this measurement.

Figure 5.10 displays the variation of spectral temperature with neutral pressure. From this figure one can observe that the spectral temperature is a

extraction potential	10 kV
extraction current	2.5 mA
pressure in the injection side of the ECRIS4	2×10^{-6} to 4×10^{-7} mbar
injection coil current	804 A
extraction coil current	754 A
incident microwave power	300 W

Table 5.3: ECRIS4 settings with the source optimised for Ar^{6+} and the pressure in the injection side of the source varied between 2×10^{-6} mbar and 4×10^{-7} mbar.

very strong function of the neutral pressure, increasing rapidly as the neutral pressure is decreased. By decreasing the neutral pressure in the injection side of the ECRIS4 from 2×10^{-6}mbar to 4×10^{-7}mbar, the spectral temperature increased by a staggering 20.2% from 25.8 keV to 31.0 keV.

Figure 5.11 displays the variation of electron density as a function of neutral pressure. This measurement indicates a linear relation between the neutral pressure and electron density, as the neutral pressure is decreased, the electron density decreases in a linear fashion. By decreasing the neutral pressure in the injection side of the ECRIS4 from 2×10^{-6}mbar to 4×10^{-7}mbar, the electron density decreased by 40.3% from 7.5×10^{10}cm^{-3} to 3.8×10^{10}cm^{-3}. This decrease of the electron density would result in an increase in the mean free path between collisions of electrons and other constituents of the plasma. The electrons would therefore travel a greater distance before undergoing a collision and as a result, its average velocity and hence its spectral temperature would increase. This effect was, for the first time to our knowledge, observed in mirror confined plasmas, in 1959 by Geller when he was experimenting with RF plasmoids [4].

The increase of electron density with increasing neutral pressure can be accounted for by considering the ionisation process in some detail. Lets assume one were able to keep an ion, of a specific element, confined in a plasma where it is continuously being bombarded by electrons with a Maxwellian distribution. If the average electron temperature is such that the electrons can, during such a bombardment, remove a shell electron from the ion, the ambient number of electrons in the plasma will increase, meaning that the electron density will increase. Increasing the neutral pressure of a specific element, increases the number of ions of that element, which leads to an increase in

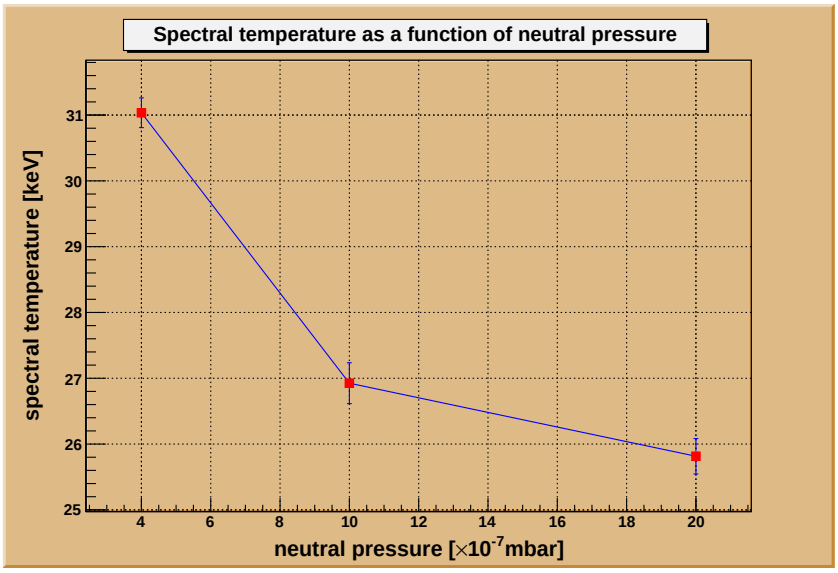

Figure 5.10: Measured spectral temperature as a function of neutral pressure for an argon plasma. The injection coil was set to 804 A, the extraction coil was set to 754 A with 300 W of microwave power incident on the plasma chamber.

the electron density.

Figure 5.12 shows the extracted ion beam intensities as a function of neutral pressure. From this figure one can observe that the extracted intensities is much lower for lower pressures, at the same source settings. This result can be understood by examining equation (5.9). The lower the neutral pressure, the lower will be the densities of the individual charge states and hence the less will be the extracted ion beam currents.

5.6.4 Investigating the influence of the solenoidal magnetic fields on electron heating and electron density

During this investigation, the source parameters were again kept constant, with only the injection and extraction coil currents being varied, either independently or simultaneously. Table 5.4 below lists the main source settings

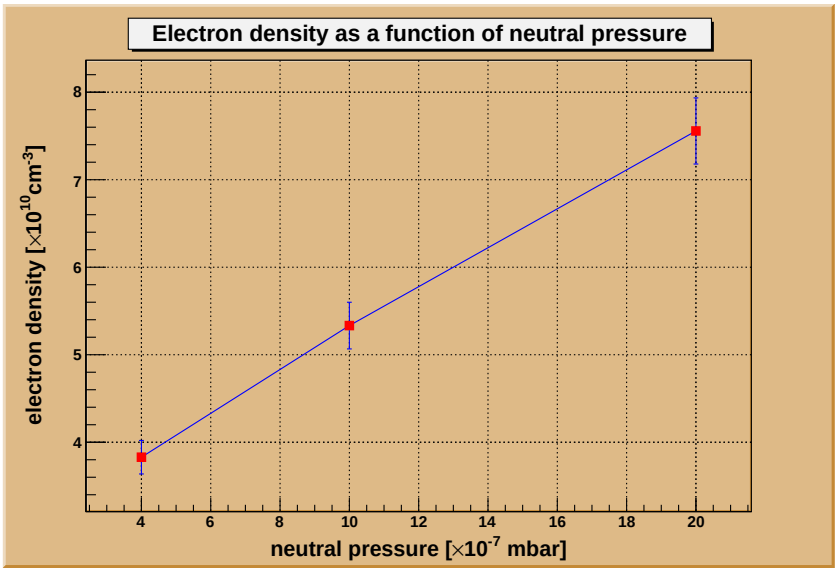

Figure 5.11: Calculated electron density as a function of neutral pressure for an argon plasma. The injection coil was set to 804 A, the extraction coil was set to 754 A with 300 W of microwave power incident on the plasma chamber.

during this measurement.

Figure 5.13 shows the measured spectral temperature for each of the solenoid coil settings. From these results, one can immediately conclude that the spectral temperature increases, as the current through the injection coil is increased and the extraction coil current kept invariant. The same result is observed as the extraction coil current is increased, with the injection coil current kept constant. By changing only one solenoid coil current, one essentially moves the plasma volume axially in the plasma chamber. By changing both solenoid coil currents, the confinement field is changed in a very complicated manner.

By keeping the extraction coil current invariant at 754 A, the injection coil current was varied from 754 A to 909 A. Over this range, the spectral temperature of the electron population under investigation, increased an astounding 14.5%. This measurement was repeated by keeping the injection coil current invariant at 803 A and varying the extraction coil current from 713 A to 838 A. During these ranges of measurement, the spectral temperature increased a substantial 16.2%. The reason for these significant increase

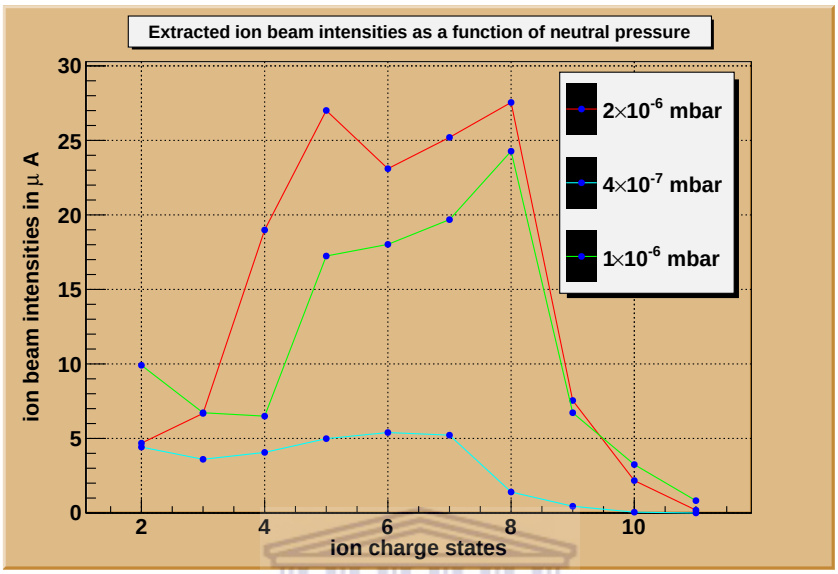

Figure 5.12: Extracted ion beam intensities as a function of neutral pressure for an argon plasma. The injection coil was set to 804 A, the extraction coil was set to 754 A with 300 W of microwave power incident on the plasma chamber.

extraction potential	10 kV
extraction current	2.5 mA
pressure in the injection side of the ECRIS4	2×10^{-6} mbar
pressure in the extraction side of the ECRIS4	6×10^{-7} mbar
injection coil current	754 A to 909 A
extraction coil current	713 A to 838 A
incident microwave power	300 W

Table 5.4: ECRIS4 settings with the source optimised for Ar^{6+} and the injection and extraction coil currents varied either independently or simultaneously.

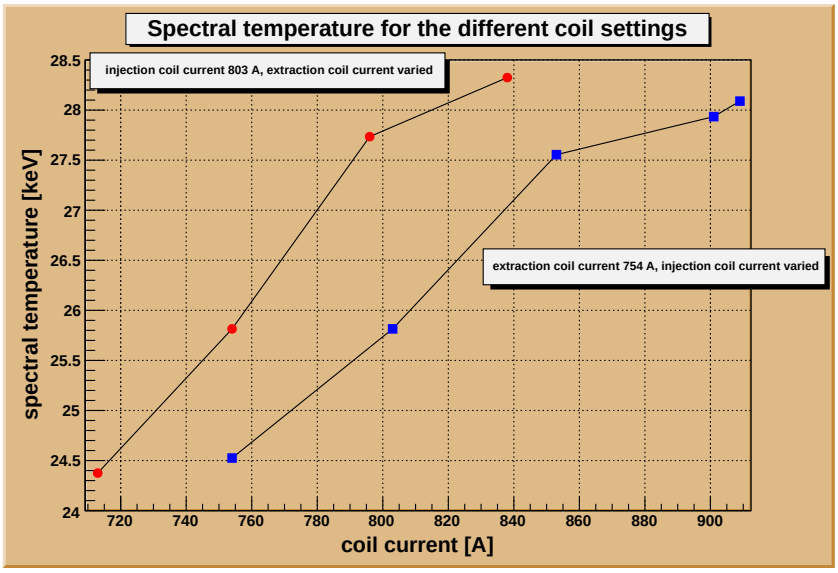

Figure 5.13: Measured spectral temperature for the different coil settings for an argon plasma.

in spectral temperature can be explained using the magnetic field gradient near the resonance zone.

Figure 5.14 shows the electron density, calculated from the extracted ion beam currents, for each of the solenoid coil settings. If one, for the time being, ignores the electron density associated with the coil settings, 909A/754A, then the electron density over this wide range of coil setting is confined to a very narrow band of electron densities. From this it can be concluded that by varying the coil current settings in these measurements, one practically made no change to the electron density. During the coil setting 909A/754A, the electron loses through loss cone of the magnetic bottle was increased, hence the electron density decreased significantly.

The result of increasing spectral temperature with changing coil currents in our measurements is attributed to the changing gradient of the magnetic field near the resonance zone. As described earlier, the magnetic confinement system of the ECRIS4 consists of a permanent magnet hexapole and two electromagnet solenoid coils. This forms the min-B structure for which one can measure along the centre line, axially, a B_{max} and a B_{min}. These are the maximum and minimum magnetic field strength, respectively. Additionally one can also define a B_{ECR} which is a closed magnetic surface where the

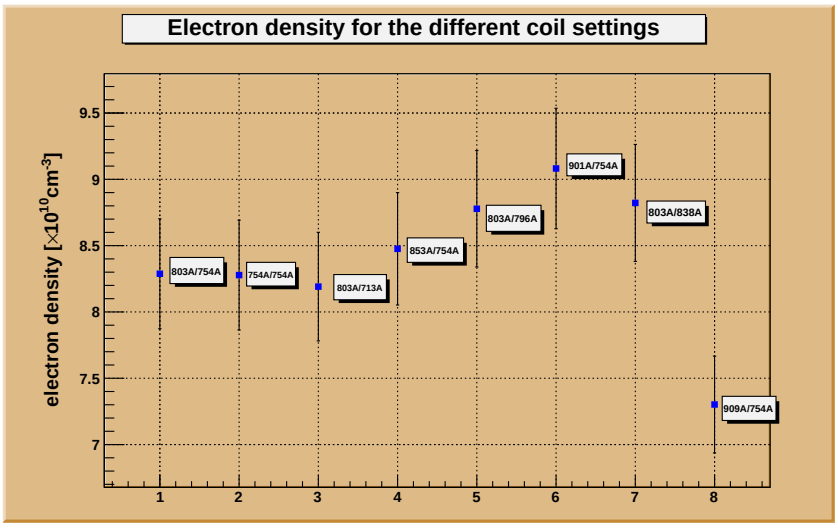

Figure 5.14: Calculated electron density for the different coil settings for an argon plasma.

incident microwave power launched from the outside, has the same frequency as the circulating electrons. Hence at this magnetic field strength, ECR heating occurs.

Investigations carried out by other groups have shown that the spectral temperature increase with decreasing $\frac{B_{\min}}{B_{\mathrm{ECR}}}$ [39]. By decreasing the gradient of the magnetic field near the resonance zone, the electrons near this zone are in contact with heated electrons for longer periods of time. Via collisions with these heated electrons, energy is transferred from the heated electrons to the ambient electrons. One therefore concludes that decreasing the gradient at the ECR zone makes heating of electrons more efficient.

As we have not had the opportunity to measure the magnetic field characteristics of the ECRIS4, we can only speculate that the reason for the increase in spectral temperature we observed was as a result of the changes made to $\frac{B_{\min}}{B_{\mathrm{ECR}}}$. This result is also backed by theoretical models which predict that the energy gain by the particle will increase as the gradient decreases [39].

Chapter 6

Summary and conclusions

The aim of the investigation was firstly to build-up and test a measurement setup that could be used to study the axial bremsstrahlung radiation generated by the plasma of an ECRIS. Secondly the emitted bremsstrahlung radiation was analysed. In doing this, it was endeavoured to gain a better understanding of the relative importance of the various ion source parameters on the production of multiply charged ion species. This body of knowledge is especially important given our facility's ambitions to develop a radioactive ion beam facility in the near future. Additionally the measurement setup could be used to perform time-resolved measurements on the emitted bremsstrahlung radiation. This will be extremely valuable, given that the GTS2 is required to operate in pulsed mode to enable us to perform beam development for CERN [60].

Instead of opting for the traditional analogue electronics, it was decided to implement a digital measurement setup using the DGF Pixie-4 [51]. The main motivation for this choice lies in our aspirations to carry out intensive investigations on electron heating in the near future. To analyse the measured bremsstrahlung spectra, a number of subroutines were written, which could be extended should we choose to enter the realm of time-resolved measurements.

Using the measurement setup implemented, the influence of neutral pressure, incident microwave power and solenoid coil currents on the spectral temperature, electron density and extracted ion beam intensities was investigated. From these measurements it was concluded that the spectral temperature increases almost linearly with an increase in microwave power. By increasing the incident microwave power from 0.050 kW to 0.300 kW, a spectral temperature increase of 14.0% for a helium plasma and 7.9% for an argon

plasma was measured. It was also noticed that by increasing the incident microwave power in 0.050 kW intervals, the growth of spectral temperature in consecutive intervals appears to slow down. This led us to believe that we were close to observing the saturation effect mentioned by other investigators of bremsstrahlung phenomena [39].

The influence of neutral pressure on spectral temperature was found to be significant. By decreasing the neutral pressure in the injection side of the ECRIS4 from 2.00×10^{-6}mbar to 4.00×10^{-7}mbar, a spectral temperature increase of 20.2% was measured. To explain this result, the electron density over this range of pressure variation was also calculated. This calculation showed a decrease of 40.3% in electron density over the range of pressure variation. It was therefore concluded that the increase in spectral temperature is probably related to the increase in mean free path of the electrons. The ion beam intensities extracted at low pressure were significantly lower then those at higher pressures. It should however be mentioned that throughout this study, the source was optimised for medium charge states and all source parameters kept constant except for the parameter under investigation.

The influence of the solenoid coil current settings on spectral temperature and electron density was also investigated. From these measurements a significant increase in spectral temperature of 14.5% was noticed by increasing the injection coil current and keeping the extraction coil current constant. By increasing the extraction coil current and keeping the injection coil current constant, an even larger increase in spectral temperature of 16.2% was measured. These effects were attributed to a more efficient heating of the electrons near the resonance zone of the ECRIS4. The calculated electron density were largely confined to a very narrow band, if the electron density as a result of the coil setting 909A/754A is discarded. Over the range of variation of coil currents, the electron density only varied between 8.2×10^{10}cm^{-3} and 9.1×10^{10}cm^{-3}. This is a variation of less then 11.2%, which implies that in these current coil settings, the electron density stayed reasonable constant.

Lastly it was observed that the electron density over our wide spectrum of changes made to the source never exceeded 9.1×10^{10}cm^{-3}. Comparing this value to the values obtained from the literature, it appears that our electron density is at least an order of magnitude lower than those quoted for similar sources. The reason for this variation remains unknown and will be intensively investigated in future studies on both ECR ion sources. It should also just be mentioned that the measurements presented in this study

were not geared towards high electron density and high output currents. In our case source stability and repeatability was of higher concern.

Bibliography

[1] Reitmann, D., 1995. A brief history of South Africa's cyclotrons. In: iThemba LABS (Laboratory for Accelerator Based Sciences), 14th International Conference on Cyclotrons and their Applications. Cape Town, South Africa, 8-13 October 1995. Singapore : World Scientific Publishing Co.

[2] Botha, A.H., 2008. Discussion on the Pretoria cyclotron. [conversation] (Personal communication, 8 January 2008).

[3] National Accelerator Project, 1976. Technical Report of the Accelerator Task Group. August 1976.

[4] Geller, R., 1996. Electron Cyclotron Resonance Ion Sources and ECR Plasmas. Bristol: Institute of Physics Publishing.

[5] Botha, A.H., 1994. Notas oor siklotrone. [notes], iThemba LABS [previously known as National Accelerator Centre (NAC)], Cape Town, South Africa.

[6] Bernhardi, K. and Wiesemann, K., 1982. X-ray bremsstrahlung measurements on an ECR-discharge in a magnetic mirror, Plasma Physics, vol 24, no 8, pp 867-884.

[7] Gerlach, W. and Stern, O., 1922. Das magnetische Moment des Silberatoms. Zeitschrift für Physik 9, pp 353-355.

[8] Jungwirth, H.N., Bruins, L.D., Botha, A.H. and Pabot, J.L., 1975. Design of magnets for an Open-Sector Cyclotron. In: Swiss Institute for Nuclear Research (SIN), 7th International Conference On Cyclotrons and their Applications. Zürich, Switzerland, 19-22 August 1975. Basel : Birkhäuser Verlag.

[9] de Villiers, J.G., 2006. The study of a novel flat-topping resonator for more intense proton beams of better quality from cyclotrons. Ph.D. thesis. University of Witwatersrand.

[10] Botha, A.H. and Kritzinger, J.J., 1975. Design of an RF system for an Open-Sector Cyclotron, In: Swiss Institute for Nuclear Research (SIN), 7th International Conference On Cyclotrons and their Applications. Zürich, Switzerland, 19-22 August 1975. Basel : Birkhäuser Verlag.

[11] du Toit Z.B., Burger S.J., *et al.*, 1981. Aspects of the design of an 8 MeV cyclotron as injector for a 200 MeV separated-sector cyclotron, In: University of Caen, 9th International Conference On Cyclotrons and their Applications, Caen, France, 7-10 September 1981. Paris : Les Editions de Physique.

[12] Livingston, M.S. and Blewett, J.P., 1962. Particle Accelerators. New York : McGraw-Hill Book Company.

[13] Cornell, J.C., Conradie, J.L. and Fourie, D.T., 1992. Beamlines for a second injector cyclotron at NAC, In: TRIUMF. 13th International Conference On Cyclotrons and their Applications, Vancouver, Canada, 6-10 July 1992. Singapore : World Scientific Publishing Co.

[14] Conradie, J.L., Cornell, J.C. and Fourie, D.T., 1991. Transfer beamlines for ECR and polarised-ion sources, 12th International Conference on Cyclotrons and their Applications, Berlin, Germany, 8-12 May 1989. Singapore : World Scientific Publishing Co.

[15] Thomae, R., *et al.*, 2008. Status of new electron cyclotron resonance ion sources at iThemba LABS, In: Argonne National Laboratory. 18th International Workshop on ECR Ion Sources. Chicago, Illinois, USA, 15-18 September 2008.

[16] Chen, F.F., 1977. Introduction to plasma physics. New York, United States of America : Plenum Press.

[17] Goldston R.J. and Rutherford P.H., 1995. Introduction to plasma physics. Philadelphia : Institute of Physics Publishing.

[18] Jackson, J.D., 1962. Classical Electrodynamics. New York : John Wiley and Sons.

[19] Hutchinson, I.H., 2001. Principles of Plasma Diagnostics. Cambridge : Cambridge University Press.

[20] Lotz, W., 1968. Electron-Impact Ionisation Cross-Sections and Ionisation Rate Coefficients for Atoms and Ions from Hydrogen to Calcium. Zeitschrift für Physik, 216, pp 241-247.

[21] Shirkov, G.D., Mühle, C., Musiol, G. and Zschornack, C., 1991. Ionisation and charge dispersion in electron cyclotron resonance ion sources. Nuclear Instruments and Methods in Physics Research A, A302, 1991, pp 1-5.

[22] Müller, A. and Frode, R., Phys. Rev. 44 (1080) 29.

[23] Müller, A. and Salzborn, E., 1976. Phys. Lett., A59 (1976) 19.

[24] Panofsky, W. and Phillips, M., 1965. Classical Electricity and Magnetism. New York : Addison-Wesley.

[25] Gallardo, J., 1999. Note on Vector Potential and Magnetic Field for a Solenoid, BNL-CAP-Tech. Notes MU-033. [notes], New York.

[26] Gradshteyn, I. and Ryzhik, I.,1980. Tables of integrals, Series and Products. New York : Academic Press.

[27] Gallardo, J., 1999. Errors in a continuous solenoid, BNL-CAP-Tech. Notes MU-033. [notes], New York.

[28] Conradie, J.L., 1985. Eksperimentele evaluering van vierpoolmagnete. M.Sc. thesis. University of Stellenbosch.

[29] Halbach, K., 1980. Design of permanent multipole magnets rare earth cobalt material. Nuclear Instruments and Methods, 196, 1980, pp 1-10.

[30] Dandl, R.A., Eason, H.O., Guestg, G.E., Hedrickc, C.L., Ikegami, H. and Nelson, D.B. Plasma Physics and Controlled Nuclear Fusion Research : Tokyo Proc. 5^{th} int. Conf. Tokyo, 1974. vol. 2, IAEA, Vienna, pp 141

[31] Ard, W.B., Becker, M.C., Dandl, R.A., Eason, H.O., England, A.C. and Kerr, R.J., 1963. Neutron Production from a Steady-State, Hot-Electron, Deuterium Plasma. Phys. Rev. Lett. vol. 10, no 3, pp 87-89.

[32] T. J. Fessenden. Pulsed electron-cyclotron resonance discharge experiment. Technical Report MIT-3221-19, Massachusetts Institute of Technology, 1966.

[33] Zhoa, H.Y., Zhang, W.H., Cao, Y., Zhoa, H.W., Lu, W., Zhang, X.Z., Zhu, Y.H., Li, X.X., and Xie, D.Z., 2010. Measurements of bremsstrahlung radiation and X-ray heat load to cryostat on SECRAL. Proceedings of ECRIS2010, Grenoble, France.

[34] Zhao, Y. H.,*et al.*, 2008. Experimental study of hot electrons in LECR2M plasma. Review scientific instruments, vol 79, 02B504, 2008, pp 1-4.

[35] Zhao, Y. H.,*et al.*, 2006. Measurements of bremsstrahlung spectra on Lanzhou ECR Ion Source No. 3 (LECR3). Review scientific instruments, vol 77, 03A312, 2006, pp 1-3.

[36] Toivanen, V., Koivisto, H., Steczkiewicz, O., Celona, L., Tarvainen, O., Ropponen, T., Gammino, S. and Ciavola, G. 2010. Effect of ECR ion source frequency tuning on ion beam intensity and quality at Department of Physics, University of Jyväskylä, Rev. Sci. Instrum., 81, 2010, 02A319.

[37] Ropponen, T.; Tarvainen, O.; Jones, P.; Peura, P.; Kalvas, T.; Suominen, P.; Koivisto, H. and Ärje, J, 2009. The effects of magnetic field strength on the time evolution of high energy bremsstrahlung radiation created by an electron cyclotron resonance ion source. Nuclear Instruments and Methods in Physics Research A 600 (2009), pp 525-533

[38] Ropponen, T.; Tarvainen, O.; Jones, P.; Peura, P.; Kalvas, T.; Suominen,P. and Koivisto, H., 2009. Time evolution of high-energy bremsstrahlung and argon ion production in electron cyclotron resonance ion-source plasma. IEEE transactions on plasma science, vol 37, no 11, pp 2146-2152.

[39] Noland, J.D., 2011. Measurements of plasma bremsstrahlung and plasma energy density produced by electron cyclotron resonance ion source plasmas. Ph.D. thesis. University of California, Berkeley, USA.

[40] Leitner, D., Benitez, J.Y., Lyneis, C.M., Todd, D.S., Ropponen, T., Ropponen, J., Koiivisto, H. and Gammino, S, 2008. Measurement of the high energy component of the X-ray spectra in the VENUS electron cyclotron resonance ion source, Rev. Sci. Instrum., 79, 2008, 033302.

[41] Benitez, J.Y.; Noland, J.D.; Leitner, D.; Lyneis, C.; Todd, D.S. and Verboncoeur, J., 2008. High-energy component of X-ray spectra in ECR ion sources. In : LBNL, Proceedings of ECRIS08, Chicago, IL, USA.

[42] Ropponen, T. Bremsstrahlung and Ion Beam Current Measurements with SuSI ECR Ion Source. Proceedings of ECRIS2010, Grenoble, France.

[43] Bernhardi, K. and Wiesemann, K., 2012. A collimator for hot plasma X-ray diagnostics in ion sources, Rev. Sci. Instrum., vol 83, no 2, 2012, 02A337.

[44] Bernhardi, K., 1980. An improved deconvolution method for bremsstrahlung spectra from hot plasmas. Computer Physics Communications, 19, pp 17-21.

[45] Martin, B.; Grether, M.; Köhrgrück, R.; Stettner, U.; Waldmann, H. 1993. The Berlin 14.5 GHz ECR ion source, and its testbench for the production of slow, highly charged ions. In : University of Groningen, Proceedings of the 11th international workshop on electron cyclotron resonance ion sources. Netherlands, 6-7 May, 1993.

[46] Hitz, D., *et al.*, 2003. Multiply charged ion production with ECR ion sources: State of the art and prospects. Nuclear Instruments and Methods in Physics Research B 205 (2003), pp 168-172.

[47] Keller, R., 1989. The physics and technology of ion sources. New York: Wiley-interscience.

[48] Thuillier, T.; Lamy, T.; Latrasse, L.; Izotov, I,V.; Sidorov, A.V.; Skalyga, A.; Zorin, V.G. and Marie-Jeanne, M, 2008. Study of pulsed electron cyclotron resonance ion source plasma near breakdown: The preglow. Review of Scientific Instruments 79, 02A314.

[49] Ropponen., T., 2010. Electron Heating, time evolution of bremsstrahlung and ion beam current in electron cyclotron resonance ion sources. Ph.D. thesis. University of Jyväskylä.

[50] Leo, W.R., 1987. Techniques for nuclear and particle physics experiments. Berlin : Springer-Verlag.

[51] XIA LLC, 2006.User's Manual Digital Gamma Finder (DGF) PIXIE-4. [on-line]. USA : XIA. Available at http://www.xia.com. [Accessed 17 March 2011].

[52] Lamoreux, M. and Charles, P., 2006. General deconvolution of thin-target and thick-target bremsstrahlung spectra to determine electron energy distributions, Radiation Physics and Chemistry 75 (2006), pp 1220-1231.

[53] ROOT: An object-orientated data analysis framework, 1994. Available at http://root.cern.ch/drupal/ [Accessed 15 March 2011]

[54] West, H.I. Jr., 1982. preprint UCRL-53391, Lawrence Livermore National Laboratory, California, USA.

[55] Shirkov, G., 1991. The multiply charged ion production in ECR ion sources. Review of scientific instruments, vol 63, no 4, April 1992, pp 2894-2896.

[56] Hitz, D., 2006. Recent Progress in High Frequency Electron Cyclotron Resonance Ion Sources. Advances in imaging and electron physics, vol 144, pp 1-150.

[57] Ropponen, T., Tarvainen, O., Suominen, P., Koponen, T.K., Kalvas, T., Koivisto, H., 2008. Hybrid simulation of electron cyclotron resonance heating. Nuclear Instruments and Methods in Physics Research A, 587, 2008, pp 115-124.

[58] Cannobio, E. 1972.Neoclassical theory of landau damping and ion and electron transit-time magnetic pumping (TTMP) in toroidal geometry. Nuclear Fusion, vol 12, no 5, 1972.

[59] Perret, C., Girard, A., Khodja, H. and Melin, G, 1999. Limitations to the plasma energy and density in electron cyclotron resonance ion sources. Physics of Plasmas, vol 6, no 3408, 1999.

[60] Thomae, R., 2010. Report on the visit to CERN (BE-ABP Department). [report], iThemba LABS, Cape Town, South Africa.